Response to the Reviewers

Probabilistic tsunami hazard assessment at Stromboli volcano: 2. New simulation database and probabilistic inundation maps and curves

Manuscript egusphere-2026-1602 | *Journal: Natural Hazards and Earth System Sciences*

General response

Response: We sincerely thank the Editor and both Reviewers for their careful reading of the manuscript, their positive assessment of the study, and their constructive suggestions. We have revised the manuscript and Supporting Information accordingly. The revisions clarify the novelty and scope of the work, distinguish the complete public simulation repositories from the common subset used in the probabilistic analysis, improve the definitions of source parameters and tsunami intensity measures, discuss the role of the initial landslide position and source azimuth, and correct the figures, cross-references, section numbering, and language issues identified by the Reviewers. Below, each comment is reproduced in full, followed by our response and, where appropriate, the corresponding revised or proposed manuscript text.

Response to Anonymous Referee #2

Reviewer comment: *Thank you for the opportunity to review this great manuscript, here are some of my comments:*

Response: We sincerely thank the Reviewer for the positive assessment and for the concise, constructive comments. The comments have helped us clarify the novelty, scope, and terminology of the manuscript. Our point-by-point responses are provided below.

Comment a. Novelty and relationship to the simulation repositories

Reviewer comment: *a). The manuscript should clarify more explicitly the main novelty of this database compared with Cerminara et al. (2024) and de' Michieli Vitturi et al. (2026). In particular, the authors should concisely highlight the contributions of the 10-m topo-bathymetry itself, the numerical-model modifications, and expanded set of 462 scenarios.*

Response: We thank the Reviewer for this helpful comment. We agree that the relationship between the present work, Cerminara et al. (2024), and de' Michieli Vitturi et al. (2026a, b) was not sufficiently explicit in the original manuscript.

First, we would like to clarify that de' Michieli Vitturi et al. (2026a, b) are not separate scientific studies preceding the present work. They are the associated INGV data repositories in which the two numerical simulation databases developed for this study are publicly archived. We have revised the Introduction and Section 2.2 to make this relationship explicit.

The novelty with respect to Cerminara et al. (2024) concerns both the extension of the scenario space and the modelling configuration. The previous database included six landslide volumes (3, 5, 8.7, 14, 21, and 30 × 10^6 m^3), whereas the databases developed for the present study provide a substantially denser sampling of landslide volume, extending the common range from 1 to 40 × 10^6 m^3. The complete 20 m and 10 m repositories contain 495 and 462 simulations, respectively. For the probabilistic analysis, however, we use a common subset of 308 simulations per database, based on 14 common volumes, 11 initial positions, and two landslide bulk densities.

The complete repositories also include simulations with a bulk density of 2500 kg m^{-3}. This value was retained for consistency with previous simulation databases and to facilitate comparison with earlier modelling studies, but it was not used in the probabilistic analysis because such a high bulk density is not considered representative of the fragmented and porous granular material involved in the avalanches occurring along the Sciara del Fuoco. Accordingly, only the two lower bulk densities were retained for the PTHA.

We also note that the other two aspects highlighted by the Reviewer (the new 10 m topo-bathymetry and the modifications introduced in the updated version of Multilayer-HySEA) were already described in detail in Section 2.2 of the manuscript. In particular, the manuscript discusses the higher native resolution and more recent acquisition of the new bathymetric and topographic datasets, together with the limitations associated with vegetation and partially resolved urban features. It also explicitly describes the principal changes introduced in the 2025 version of Multilayer-HySEA, including the new Riemann solver, the revised treatment of incompressibility, and the updated formulations for vertical viscosity, bottom friction, and run-up. We have therefore retained these detailed descriptions and revised the surrounding text only where needed to clarify the relationship between the present databases, Cerminara et al. (2024), and the associated INGV data repositories.

Finally, we have also revised the Introduction so that it concisely states that the two new databases extend the scenario set of Cerminara et al. (2024) and are publicly available through the associated INGV data repositories de' Michieli Vitturi et al. (2026a, b).

Changes in the manuscript: The Introduction has been revised to clarify that de' Michieli Vitturi et al. (2026a, b) correspond to the associated INGV data repositories and that the databases developed for the present study extend the scenario set previously presented by Cerminara et al. (2024). Section 2.2 has also been revised to make the extension of the volume sampling more explicit, to distinguish the complete repositories (495 and 462 simulations) from the common 308-simulation subset used in the PTHA, and to explain why the 2500 kg m^{-3} bulk-density cases were retained in the repositories but excluded from the probabilistic analysis. The existing detailed descriptions of the 10 m topo-bathymetry and of the updated Multilayer-HySEA model have been retained, since these aspects were already explicitly documented in Section 2.2.

Proposed revised text (Introduction): *Building on that work, this paper utilizes the probabilistic outputs of the expert elicitation to probabilistically weight the scenarios contained in two new databases of numerical tsunami simulations. These databases extend the scenario set previously presented by Cerminara et al. (2024) and are publicly archived in the associated data repositories de' Michieli Vitturi et al. (2026a, b), which provide the numerical datasets analysed in the present study.*

Proposed revised text (Section 2.2): "*To explore the epistemic uncertainties associated with tsunami modelling at Stromboli, this study relies on two new databases of numerical simulations developed for the present work and publicly available through the associated INGV data repositories de' Michieli Vitturi et al. (2026a) and de' Michieli Vitturi et al. (2026b). These databases were designed to cover an identical matrix of landslide scenarios but were generated using different topobathymetric data and different landslide and tsunami numerical simulation model setups (code versions). All simulations were performed on a 21.9 × 23 km computational domain centred on Stromboli. The tsunamigenic source was modelled as the collapse of a granular mass placed on the existing topography. The geometry and position of the mass are defined by the horizontal coordinates of its barycentre (x_0, y_0) and its length, width, and vertical thickness. These parameters collectively determine the landslide volume. In addition, the material's bulk density must be specified, typically as a water/material density contrast. The initial barycentre elevation z_0 is defined relative to mean sea level, with positive values corresponding to subaerial release positions and negative values to submarine positions. The density contrast parameter is defined as the water-to-landslide bulk-density ratio $r_\rho = \rho_w/\rho_s$, where ρ_w and ρ_s are the water density and the bulk density of the granular mass, respectively.*

The simulations used in this paper represent a subset of those available in de' Michieli Vitturi et al. (2026a-b) and comprise 11 initial barycentric positions along the Sciara del Fuoco centreline (P0-P10, see Fig. 1), two water/landslide density contrasts (0.5 and 0.6, corresponding respectively to material densities of 2000 and 1667 kg/m³) and 14 landslide volumes (1, 1.5, 2, 3, 5, 8, 8.7, 11, 14, 17, 21, 25, 30 and 40 × 10^6 m^3). The initial granular mass is released from rest, with no prescribed initial velocity or direction of motion; its subsequent trajectory develops dynamically according to gravity, the local topography and bathymetry, the adopted rheology, and its interaction with the water. Thus, the 11 positions constrain the initial release locations along the central axis of the Sciara del Fuoco, rather than *imposing a predetermined landslide path. Of the 14 landslide volumes considered in the probabilistic analysis, six (3, 5, 8.7, 14, 21 and 30 × 10^6 m^3) were already included in Cerminara et al. (2024); the additional volumes provide a more granular sampling of the source-volume range, particularly at the lower end and between the previously simulated values. The 2500 kg/m^3 cases were retained in the complete repositories for consistency with previous simulation databases and to facilitate comparison with earlier modelling studies, but were excluded from the PTHA because such a high bulk density is not considered representative of the fragmented and porous granular material involved in the avalanches considered at the Sciara del Fuoco. The complete 20 m and 10 m repositories in de' Michieli Vitturi et al. (2026a-b) contain 495 and 462 simulations, respectively, including three landslide bulk densities. For the probabilistic analysis presented here, we use a common subset of 308 simulations for each database, obtained from the 11 initial positions, 14 common volumes, and the two bulk densities considered representative of granular landslides at the Sciara del Fuoco..”*

Comment b. Landslide direction and initial position

Reviewer comment: *b) The source scenarios appear to vary mainly in volume, elevation, and density, while the landslide direction seems to be kept along a single trajectory. It would be interesting and scientifically valuable to include, not only different landslide directions, or at least discuss them.*

Response: We thank the Reviewer for this important comment. We would first like to clarify that, in our simulations, no initial landslide velocity or prescribed direction of motion is imposed. The granular mass is released from rest, and its subsequent acceleration, deformation, spreading, and trajectory are computed dynamically by the coupled granular-flow–water model as a consequence of gravity, the local topographic and bathymetric gradients, the adopted rheology, and the interaction with the water. The 11 initial positions used in the present PTHA are therefore release locations distributed along the central axis of the Sciara del Fuoco, rather than points constrained to follow a prescribed kinematic path.

The uncertainty that is not explicitly propagated in the present PTHA is instead the lateral position of the initial mass at a given elevation. This aspect has been investigated in previous work. Esposti Ongaro et al. (2025) displaced the initial barycentre laterally with respect to the central axis of the Sciara del Fuoco, by approximately 440 m toward the NE and 395 m toward the SW, and found variations of about 10% in proximal waveforms, smaller than those associated with the dominant source parameters.

This is also consistent with the recent parametric study of Trolese et al. (2026). In that study, the parameter referred to as source azimuth corresponds to different lateral source positions/transects across the Sciara del Fuoco, again without imposing any initial velocity or prescribed direction of motion. The sensitivity analysis shows that this lateral source-position parameter is, on average, a secondary control on maximum wave height compared with the dominant parameters, although larger local effects can occur close to the source.

On this basis, we consider the use of the central Sciara del Fuoco axis to be an appropriate first-order representation for the present PTHA, while recognizing that lateral source position constitutes an additional source of epistemic uncertainty that could be explicitly propagated in future extensions of the hazard model. We have revised both Section 2.2 and the Discussion to clarify these points.

Changes in the manuscript: Section 2.2 has been revised to clarify that the granular mass is released from rest and that no initial velocity or prescribed direction of motion is imposed. The selected points along the central Sciara del Fuoco axis therefore constrain the initial release locations, not the subsequent kinematic trajectory. In addition, Section 4.3 now explicitly identifies lateral source position at fixed elevation as a source-related uncertainty not propagated in the present PTHA and briefly discusses the results of Esposti Ongaro et al. (2025) and Trolese et al. (2026).

Proposed revised text in Section 2.2: *The initial granular mass is released from rest, with no prescribed initial velocity or direction of motion; its subsequent trajectory develops dynamically according to gravity, the local topography and bathymetry, the adopted rheology, and its interaction with the water. Thus, the 11 positions constrain the initial release locations along the central axis of the Sciara del Fuoco, rather than imposing a predetermined landslide path.*

Proposed revised text in Section 4.3: *Lateral source position. The lateral position of the initial mass at a given elevation is not explicitly propagated in the present PTHA. Esposti Ongaro et al. (2025) found that lateral displacements of the source within the Sciara del Fuoco produced variations of about 10% in proximal waveforms, smaller than those associated with the dominant source parameters. Consistently, Trolese et al. (2026) identify lateral source position, represented through different source azimuths/transects across the Sciara del Fuoco, as a secondary control on maximum wave height on average, although its influence can be locally larger close to the source.*

Comment c. Definitions of source parameters and outputs

Reviewer comment: *c) The definitions of several scenario parameters and outputs should be clarified in more detail. Authors should define the meaning of 'vertical elevation' and 'density contrast,' as well as distinguish clearly between maximum wave height above sea level, inundation height above ground, and water depth. Although I understand the meaning of each parameters, but the different meaning of vertical elevation and density contrast should be well explained.*

Response: We thank the Reviewer and agree. We will replace the generic expression 'vertical elevation' with 'initial barycentre elevation' and define it as the elevation of the barycentre of the initial granular mass relative to mean sea level, with positive values for subaerial positions and negative values for submarine positions. We will also define the density parameter mathematically as the water-to-landslide bulk-density ratio rρ = ρw/ρs. The complete repositories use rρ = 0.4, 0.5, and 0.6, corresponding to landslide bulk densities of 2500, 2000, and approximately 1667 kg m−3 for ρw = 1000 kg m−3; the PTHA uses only rρ = 0.5 and 0.6 for the physical reason explained in our response to Comment a.

We will further standardize the output terminology. Maximum free-surface elevation and inundation height are elevations relative to mean sea level, whereas water depth (or inundation/flow depth) is the vertical water thickness above the local ground surface. The hazard maps and curves presented in this manuscript are based on maximum water depth above ground, unless explicitly stated otherwise. We will avoid using 'wave height' for an elevation above sea level where 'free-surface elevation' is intended.

Changes in the manuscript: Definitions will be added in Sect. 2.2 and at the beginning of the methodological section on hazard products. Figure captions, axis labels, and the Data Availability description will be checked for consistent use of 'maximum free-surface elevation', 'inundation height/elevation', and 'maximum water depth above ground'.

Proposed revised text: *The initial barycentre elevation z_0 is defined relative to mean sea level, with positive values corresponding to subaerial release positions and negative values to submarine positions. The density contrast parameter is defined as the water-to-landslide bulk-density ratio* $r_\rho = \rho_w/\rho_s$*, where* ρ_w *and* ρ_s *are the water density and the bulk density of the granular mass, respectively.*

Proposed revised text: *To avoid ambiguity in the terminology used in the maps and curves, we distinguish between free-surface elevation, measured relative to mean sea level, and water depth, measured relative to the local ground surface. Maximum free-surface elevation denotes the maximum positive free-surface elevation at a marine location, whereas inundation height (or inundation elevation) denotes the maximum elevation reached by the free surface over initially dry land, also relative to mean sea level. Water depth is instead the vertical thickness of water above the local ground surface. Unless otherwise stated, the probabilistic maps and hazard curves presented in this study refer to maximum water depth above ground.*

Additional author-initiated revisions

Response: In addition to the changes explicitly requested by the Reviewers, we have conducted a full language and consistency revision. This included correcting grammatical errors in the Abstract and Methods, replacing ambiguous phrases such as 'water depth heights', correcting typographical errors such as ‘closet’ to ‘closest’, checking subject–verb agreement, and ensuring that all figures, supplementary figures, equations, and section references are complete and correctly numbered.

References additionally cited in the response and revised discussion

de’ Michieli Vitturi, M., Bevilacqua, A., Tadini, A., and Neri, A.: Version 2-ELICIPY: A Python online tool for expert elicitation. SoftwareX, 35, 102785, doi: 10.1016/j.softx.2026.102785, 2026.

Trolese, M., Cerminara, M., Esposti Ongaro, T., de’ Michieli Vitturi, M., and Tadini, A.: Sensitivity analysis and scaling of tsunamis generated by granular flows at Stromboli volcano: A numerical modeling approach. EGUsphere preprint, https://doi.org/10.5194/egusphere-2026-1757, 2026.

Probabilistic tsunami hazard assessment at Stromboli volcano: 2. New simulation database and probabilistic inundation maps and curves

Mattia de' Michieli Vitturi[1], Alessandro Tadini[1], Andrea Bevilacqua[1], Juan F. Rodríguez-Gálvez[1,2], Matteo Cerminara[1], Tomaso Esposti Ongaro[1], Augusto Neri[1], Matteo Trolese[1], Jorge Macías[2], Manuel J. Castro[2], Cipriano Escalante[2], Sergio Ortega[2], José M. González-Vida[2], Stefano Lorito[3]

[1]Istituto Nazionale di Geofisica e Vulcanologia, Sezione di Pisa, via Cesare Battisti 53, 56125 Pisa, Italy.
[2]EDANYA Group, Universidad de Málaga, Avda. Cervantes 2, 29071 Málaga, Spain
[3]Istituto Nazionale di Geofisica e Vulcanologia, Sezione ONT, Via di Vigna Murata 605, 00143 Roma, Italy

Correspondence to: Mattia de' Michieli Vitturi (mattia.demichielivitturi@ingv.it), Alessandro Tadini (alessandro.tadini@ingv.it)

Abstract. Probabilistic Tsunami Hazard Assessment (PTHA) is the essential first step for quantifying the long-term risk posed by landslide-generated tsunamis at active volcanic islands like Stromboli, Italy. This study presents a first PTHA for Stromboli, providing a quantitative and transparent basis for risk mitigation and long-term coastal planning at Stromboli. In particular, our work integrates two new databases of numerical simulations for volcanic landslide-induced tsunamis with occurrence probabilities derived from expert elicitation (described in the companion paper by Tadini et al., ~~submitted~~2026). We introduce a new methodology to translate elicited probabilities for landslide frequency, volume, and location into a full suite of probabilistic hazard products. The results, expressed as hazard curves, maps and profiles (5th, 50th and 95th percentiles), are presented for alternative modelling setups, including different high-resolution topobathymetric models and code versions, to transparently account for epistemic uncertainty in the numerical hazard assessment. Our findings quantify a significant tsunami hazard for Stromboli's inhabited coastal areas over the next 50 years. The 95th percentile maps indicate that inundation by at least 0.5 m of water has a probability greater than 90% of occurring along parts of the coast of Stromboli village over the next 50 years.~~The 95th percentile maps indicate that inundation by at least 0.5 m of water has > 90% to occur along coast of Stromboli village the over the next 50 years~~. Furthermore, the hazard curves at critical sites show non-negligible probabilities of exceeding severe inundation depths ~~in~~ over the same 50~~-~~year~~s~~ ~~temporal~~ timeframe.

1 Introduction

Probabilistic Tsunami Hazard Assessment (PTHA) has become the standard framework for quantifying tsunami hazard, moving beyond deterministic, single-scenario analyses to provide a more comprehensive understanding of risk (Grezio et al., 2017; Selva et al., 2021). PTHA aims to estimate the probability of exceeding specific tsunami intensity metrics (such as inundation depth) at a given location, or conversely, to estimate the intensity metric corresponding to a given probability of exceedance, over a defined time horizon. This approach allows for the systematic integration of multiple tsunami sources and the quantification of both aleatory and epistemic uncertainties (Lorito et al., 2021), providing a robust basis for risk mitigation and coastal planning (Behrens et al., 2021).

Among the various tsunamigenic sources, landslides from volcanic islands represent a significant but complex challenge for PTHA due to the inherent instability of volcanic edifices. At Stromboli volcano (Aeolian Islands, Italy), the persistent, centuries-long volcanic activity (e.g., Barberi et al., 1993; Rosi et al., 2013; Tadini et al., ~~submitted~~2026) feeds the Sciara del Fuoco (SdF), a large horseshoe-shaped scar on the volcano's northwestern flank that is prone to both subaerial and submarine failures. The tsunamigenic potential of the SdF was dramatically demonstrated on December 30, 2002, when a sequence of landslides triggered a tsunami that caused significant damage to the island's coastline (Tinti et al., 2006b).

The 2002 event spurred significant research into the numerical modelling of landslide-generated tsunamis at Stromboli. Tinti et al. (2000, 2005, 2006b) and Fornaciai et al. (2019, 2024) presented numerical simulation results to investigate the 2002 event. Subsequent work by Esposti Ongaro et al. (2021; 2025) advanced these efforts through a systematic benchmark of different numerical codes and physical approximations. These studies highlighted the critical importance of using non-hydrostatic models to accurately capture wave generation and propagation in the near-field and explored the differences between rigid and deformable (granular) landslide models.

Beyond its scientific relevance, the 2002 event also forms the basis of the current civil protection plan in Stromboli (Protezione Civile, 2015). However, the new Italian Civil Protection Code explicitly promotes the use of probabilistic approaches, whenever possible, to assess potential risks (Protezione Civile, 2018a). In line with this, emergency planning for earthquake-generated tsunamis in Italy (Protezione Civile, 2018b) is already based on a regional long-term PTHA model (Basili et al., 2021; Tonini et al., 2021). Furthermore, for early-warning purposes related to earthquake-generated tsunamis, Italy has adopted Probabilistic Tsunami Forecasting (Selva et al., 2021; Cordrie et al., 2025), which can be regarded as a very short-term PTHA. In this context, the present paper is the second of two companion articles reporting the results of a comprehensive project aimed at developing the first formal long-term PTHA for volcanic landslide-generated tsunamis at Stromboli.

Developing a comprehensive PTHA that incorporates a temporal framework requires establishing a historical baseline of tsunami occurrences in a specific area to derive future occurrence rates. However, although Stromboli allows for a detailed review of historical sources, the available data are still insufficient for a robust statistical analysis. To address this, expert elicitation techniques (see e.g., Aspinall, 2006; Colson and Cooke, 2018; Quigley et al., 2018) represent an established approach in volcanology to quantify uncertainties in key variables (such as occurrence rates and magnitudes) in contexts where a lack of observational constraints and/or inadequate data prevent traditional analysis.

The companion paper by Tadini et al. (~~submitted~~2026) provides a detailed review of historical tsunami events at the island and, crucially, presents the results of a structured expert elicitation. That elicitation was designed to formally quantify the epistemic uncertainties associated with the key source parameters for tsunami modelling, providing probability distributions for the frequency, location, and volume of future tsunamigenic landslides (TLs) at the SdF (Fig. 1).

Building on that work, this paper utilizes the probabilistic outputs of the expert elicitation to probabilistically weight the scenarios contained in two new databases of numerical tsunami simulations. These databases extend the scenario set previously presented by Cerminara et al. (2024) and are publicly archived in the associated data repositories de' Michieli Vitturi et al. (2026a, b), which provide the numerical datasets analysed in the present study.(de' Michieli Vitturi et al., 2026a-b). We present a new methodology to integrate the probability distributions from the elicitation with the scenarios of the simulation databases to obtain a PTHA. The final products of this work are the first hazard curves at several points and probabilistic inundation maps for Stromboli (Fig. 1), expressing the probability of exceeding a given tsunami intensity value in the next 50 years, which account for the full range of elicited uncertainty. A key aspect of this study is the exploration of epistemic uncertainty introduced by numerical modelling. Accounting for land cover roughness is particularly critical, as it has been shown to significantly affect inundation extent (see e.g., Dalrymple et al., 2006; Kaiser et al., 2011; Griffin et al., 2015; Scala et al., 2024). In this work, we quantify epistemic uncertainty associated with the modelling by presenting results for two different high-resolution topographic models (20 m and 10 m) and two versions of the same numerical code.

This paper is organized as follows. Section 2 describes the numerical models, the simulation databases, and the strategy developed to integrate the expert elicitation outcomes for the generation of probabilistic curves and maps. Section 3 presents the main results, including a comparison of the hazard products derived from the different model setups and a detailed analysis of the hazard patterns. Finally, Section 4 provides some discussion and Section 5 summarizes the main conclusions of this study.

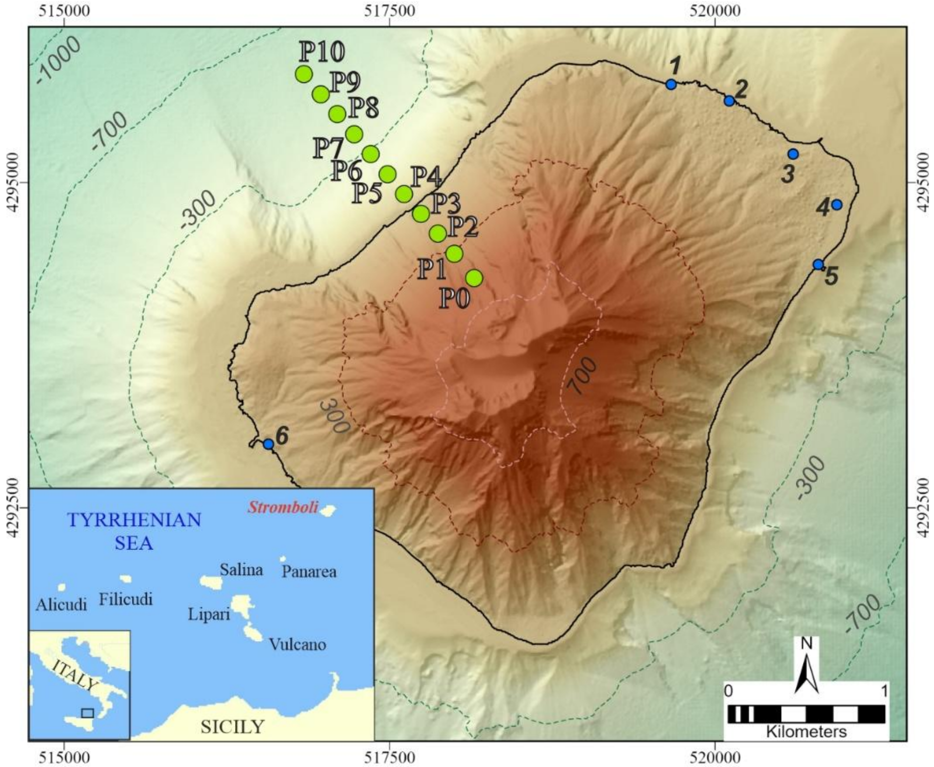

Figure 1. Stromboli volcano. Initial positions for simulations along the Sciara del Fuoco (see Section 2.2) are indicated as green points. Sites where hazard curves have been described (see Section 2.43.1) are indicated as blue points (1: Spiaggia Lunga; 2: Scalo dei Balordi; 3: Area attesa Ficogrande; 4: Centrale ENEL; 5: Molo Scari; 6: Molo Ginostra). The solid black line is the coastline. Hillshade relief is derived from a resampling at 10-m resolution of, respectively, the DSM of Bisson et al. (2025) for the subaerial part, and the bathymetry provided by I.I.M.M. (Istituto Idrografico Marina Militare - Italian Navy Hydrographic Institute) for the submarine part. Coordinates are expressed in the UTM-WGS84 33 N system.

2 Materials and Methods

2.1 Expert elicitation

Performance-based expert elicitation relies on empirical validation using quantitative calibration questions, or "seed questions", whose true answers are known to analysts but not to experts (Colson and Cooke, 2018; Quigley et al., 2018). Experts also address "target questions" (TQs) on the key issues of the problem under investigation. For both types, they provide 5th, 50th, and 95th percentiles of their uncertainty. A performance-based algorithm then combines expert opinions into group-level uncertainty distributions (Decision Maker solutions) using either equal weighting (EW) or Cooke's Classical Model (CM) (Cooke, 1991; Aspinall, 2006, 2010; Neri et al., 2008; Bevilacqua, 2016). CM weights experts based on calibration (statistical accuracy) and informativeness, computed from seed question responses (Cooke, 1991; Aspinall and Cooke, 2013; Bevilacqua et al., 2015, 2025; Tadini et al., 2017, 2022). The web-based tool ELICIPY (de' Michieli Vitturi et al., 2024; 2026) was used to manage elicitation sessions, from data collection to automated analysis and output generation.

The elicitation was aimed at estimating, for the next 50 years: i) the expected number of TLs with volumes $\geq 1 \times 10^6$ m^3 at Stromboli, and ii) their potential triggering conditions and parameters. Two expert elicitations were conducted (in 2022 and 2024), the second of which was designed to resolve ambiguities in some initial questions and to incorporate new field data that had become available. In total, 21 experts with diverse expertise and strong knowledge of Stromboli participated. Seed questions (16 total) were included only in the first round. Target questions focused on landslides $\geq 1 \times 10^6$ m^3 - roughly half the subaerial mass deposited during June – October 2019 (Di Traglia et al., 2022) and 20–30 times smaller than the December 2002 landslide (Tinti et al., 2006b).

The elicitation outcomes, described in Tadini et al. (~~submitted~~2026), provide the primary inputs for assigning probabilities to the simulations of our simulation database. For each target question, the ELICIPY tool generated a set of 10,000 samples representing the uncertainty distribution of the expert pool. This set was constructed through a two-step random sampling procedure, repeated 10,000 times: first, an expert was randomly selected with a probability equal to their performance-based weight; second, a single value was drawn from that expert's individual probability distribution. The resulting collection of 10,000 samples thus constitutes a set of equiprobable realizations of the combined expert judgment.

Table 1 provides a statistical summary of these sample sets, reporting their 5^{th}, 50^{th}, and 95^{th} percentiles for the key questions used in this study: the number of TLs in the next 50 years (TQ3), the percentage of those occurring within the SdF (TQ4), and the percentage of TLs across different landslide initial positions and volume ranges (TQ16-TQ35). While this table offers a concise summary, our methodology directly utilizes the entire collection of 10,000 samples for each question to generate the probabilistic maps and curves. This approach ensures that the full range of elicited uncertainty - and not just a summary based on three percentiles - is propagated into the final hazard assessment. Note that for TQ20-TQ35, the values in Table 1 and the corresponding samples represent conditional probabilities (see Fig. 8 in Tadini et al., 2026~~submitted~~): the probabilities used for the maps described in the following sections are recalculated as absolute probabilities by considering TQ3, TQ4 and TQ16-TQ19 (see Section 2.4~~3~~.2). These questions provide all the quantities required to assign probabilities to the numerical scenario matrix used in this study. The remaining target questions concern triggering conditions and other source characteristics that are discussed in the companion paper but are not directly required for the probabilistic weighting adopted here, either because they do not enter the present hazard calculation or because the corresponding variables are not independently varied in the numerical database. For completeness, the full list of target questions and their role in the two companion studies is provided in Table S1.

Table 1. Percentile values for TQ3-4 and TQ16-35 for the CM scoring method for TLs in the next 50 years (from Tadini et al., ~~submitted~~2026)

Question (unit)	5th	50th	95th
TQ3: TLs at Stromboli (n°)	1	4	10
TQ4: TLs along the SdF (%)	66	82	96
TQ16: TLs along the SdF, initial position 700-300 m b.s.l.	2	12	37
TQ17: TLs along the SdF, initial position 300-0 m b.s.l.	4	28	58
TQ18: TLs along the SdF, initial position 0-300 m a.s.l.	5	21	52
TQ19: TLs along the SdF, initial position 300-700 m a.s.l.	7	31	62
TQ20: TLs along the SdF, initial position 700-300 m b.s.l., volume 1-5 × 10^6 m^3 (%)	9	39	69
TQ21: TLs along the SdF, initial position 700-300 m b.s.l., volume 5-14 × 10^6 m^3 (%)	6	26	57
TQ22: TLs along the SdF, initial position 700-300 m b.s.l., volume 14-30 × 10^6 m^3 (%)	3	17	49
TQ23: TLs along the SdF, initial position 700-300 m b.s.l., volume > 30 × 10^6 m^3 (%)	0.3	9	37
TQ24: TLs along the SdF, initial position 300-0 m b.s.l., volume 1-5 × 10^6 m^3 (%)	12	44	71
TQ25: TLs along the SdF, initial position 300-0 m b.s.l., volume 5-14 × 10^6 m^3 (%)	6	25	71
TQ26: TLs along the SdF, initial position 300-0 m b.s.l., volume 14-30 × 10^6 m^3 (%)	3	14	41
TQ27: TLs along the SdF, initial position 300-0 m b.s.l., volume > 30 × 10^6 m^3 (%)	0.3	9	39
TQ28: TLs along the SdF, initial position 0-300 m a.s.l., volume 1-5 × 10^6 m^3 (%)	13	46	75
TQ29: TLs along the SdF, initial position 0-300 m a.s.l., volume 5-14 × 10^6 m^3 (%)	6	23	53
TQ30: TLs along the SdF, initial position 0-300 m a.s.l., volume 14-30 × 10^6 m^3 (%)	2	12	44
TQ31: TLs along the SdF, initial position 0-300 m a.s.l., volume > 30 × 10^6 m^3 (%)	0.1	8	39
TQ32: TLs along the SdF, initial position 300-700 m a.s.l., volume 1-5 × 10^6 m^3 (%)	9	44	75
TQ33: TLs along the SdF, initial position 300-700 m a.s.l., volume 5-14 × 10^6 m^3 (%)	6	24	58
TQ34: TLs along the SdF, initial position 300-700 m a.s.l., volume 14-30 × 10^6 m^3 (%)	2	13	48
TQ35: TLs along the SdF, initial position 300-700 m a.s.l., volume > 30 × 10^6 m^3 (%)	0.1	7	42

2.2 Numerical simulations

To explore the epistemic uncertainties associated with tsunami modelling at Stromboli, this study relies on two new databases of numerical simulations developed for the present work and publicly available through the associated INGV data repositories de' Michieli Vitturi et al. (2026a) and de' Michieli Vitturi et al. (2026b).~~To explore the epistemic uncertainties associated with tsunami modelling at Stromboli, this study relies on two distinct databases of numerical simulations, referred to as de' Michieli Vitturi et al. (2026a) and de' Michieli Vitturi et al. (2026b).~~ These databases were designed to cover an identical matrix of landslide scenarios but were generated using different topobathymetric data and different landslide and tsunami numerical simulation model setups (code versions). All simulations were performed on a 21.9 × 23 km computational domain centred on

Stromboli. The tsunamigenic source was modelled as the collapse of a granular mass placed on the existing topography. The geometry and position of the mass are defined by the horizontal coordinates of its barycentre (x_0, y_0) and its length, width, and vertical thickness. These parameters collectively determine the landslide volume. In addition, the material's bulk density must be specified, typically as a water/material density contrast. The initial barycentre elevation z_0 is defined relative to mean sea level, with positive values corresponding to subaerial release positions and negative values to submarine positions. The density contrast parameter is defined as the water-to-landslide bulk-density ratio $r_\rho=\rho_w/\rho_s$, where ρ_w and ρ_s are the water density and the bulk density of the granular mass, respectively.

The simulations used in this paper represent a subset of those ~~published~~ available in de' Michieli Vitturi et al. (2026a-b) and comprise~~, and are done considering~~ 11 initial barycentric positions along the Sciara del Fuoco centreline (P0-P10, see Fig. 1), two water/landslide density contrasts (0.5 and 0.6, corresponding respectively to material densities of 2000 and 1667 kg/m^3) and 14 landslide volumes (1, 1.5, 2, 3, 5, 8, 8.7, 11, 14, 17, 21, 25, 30 and 40 × 10^6 m^3). The initial granular mass is released from rest, with no prescribed initial velocity or direction of motion; its subsequent trajectory develops dynamically according to gravity, the local topography and bathymetry, the adopted rheology, and its interaction with the water. Thus, the 11 positions constrain the initial release locations along the central axis of the Sciara del Fuoco, rather than imposing a predetermined landslide path. Of the 14 landslide volumes considered in the probabilistic analysis, six (3, 5, 8.7, 14, 21 and 30 × 10^6 m^3) were already included in Cerminara et al. (2024); the additional volumes provide a more granular sampling of the source-volume range, particularly at the lower end and between the previously simulated values.~~Volumes 3, 5, 8.7, 14, 21 and 30 × 10^6 m^3 are those already contained in Cerminara et al. (2024).~~ The 2500 kg/m^3 cases were retained in the complete repositories for consistency with previous simulation databases and to facilitate comparison with earlier modelling studies, but were excluded from the PTHA because such a high bulk density is not considered representative of the fragmented and porous granular material involved in the avalanches considered at the Sciara del Fuoco. The complete 20 m and 10 m repositories in de' Michieli Vitturi et al. (2026a-b) contain 495 and 462 simulations, respectively, including three landslide bulk densities. For the probabilistic analysis presented here, we use a common subset of 308 simulations for each database, obtained from the 11 initial positions, 14 common volumes, and the two bulk densities considered representative of granular landslides at the Sciara del Fuoco.~~For each database, we therefore considered a total of 308 simulations.~~ The two simulation databases utilize different Digital Elevation Models (DEMs), representing one of the components of the epistemic uncertainty.

In de' Michieli Vitturi et al. (2026a) the topobathymetry is composed of:

- Topography obtained by ~~elaborating~~ processing the 3D point cloud acquired during an airborne LiDAR (Light Detection And Ranging) survey that was carried out in May 2012 (MASE, 2013). The data were acquired by using the Leica ADS80 sensor, which has instrumental vertical and horizontal accuracy of 0.10-0.20 and 0.25 m, respectively. The acquired point cloud had a mean point density of 8 pt/m^2 (Di Traglia et al., 2018).
- Bathymetry derived from the project Marine Geohazards along the Italian Coasts (MaGIC – Chiocci and Ridente, 2011). The MaGIC database consists of data with spatial resolution decreasing with depth, from 50 m to 100 and 200 m as the distance from the coast increases.

In de' Michieli Vitturi et al. (2026b), simulations use a more recent topobathymetry composed of:

- Topography obtained by elaborating 3D point cloud derived from a LiDAR (Light Detection And Ranging) survey conducted in 2023. The acquired data (Bisson et al., 2025) have a spatial resolution of 50 cm, an instrumental vertical accuracy of < 5 cm, and a horizontal (planimetric) accuracy of < 12 cm. The acquired point cloud had a mean point density with 4-~~ to ~~6 pt/m^2.
- Bathymetry from I.I.M.M. (Istituto Idrografico Marina Militare - Italian Navy Hydrographic Institute) with a resolution of 1 m from a depth of 3–4 m down to 60 m, and a resolution of 30 m from 60 m down to depths between 1000 and 1600 m.

The topographic and bathymetric data were then merged and resampled to 10 m, and a kriging interpolation was applied to fill the missing bathymetric portion between the shoreline and the beginning of the bathymetric data.

In general, a different spatial resolution of the DEM may result in a different inundation extent, with a loss of inundation detail but a larger inundation extent when using a lower resolution (e.g., Song and Goda, 2019). For our datasets, DEM resolution is not the only factor affecting the results. Indeed, although the DEMs of the two databases were both resampled to comparable grid resolutions (20 m and 10 m), an inspection of the original source data reveals substantial differences in the information content of the two topobathymetries. In particular, analysis of the 10 m versions highlights a clear contrast between the old and the new topobathymetry. For the bathymetric domain, the new version is characterized by a markedly higher native resolution and by more recent survey data, resulting in a significantly more detailed and accurate representation of the submarine morphology. This difference is already evident before any resampling procedure and directly affects the simulated tsunami wave propagation in the near-field marine environment. On land, the differences between the two datasets are of a different nature. The original data of both DEMs include the buildings, but the use of a 20 m resolution smooths them a lot. In addition, while the new topographic data are more recent, they are not filtered for vegetation. Therefore, trees (particularly tall vegetation) are retained in the DEM and appear as topographic obstacles with dimensions comparable to the tree canopy. This feature represents a major difference in the source data used for the simulations. The older topography, in contrast, is effectively smoother, because of both the vegetation filtering and the lower resolution. This must therefore be considered when interpreting the effects of the adopted DEM on the simulated inundation patterns discussed in the following sections.

The simulations in~~of~~ both the databases were performed using Multilayer-HySEA, a non-hydrostatic multilayer model capable of simulating the coupling between granular landslide motion and water dynamics on GPU architectures. A detailed description of the model and its validation can be found in Macías et al. (2021a, b) and Esposti Ongaro et al. (2025). To reflect the evolution of modelling tools and to account for epistemic uncertainty related to the numerical solver, this study employs two distinct versions of the code, referred to here as the "2021 version" and the "2025 version". The first one corresponds to the stable release available at the beginning of this study and used in previous hazard assessments at Stromboli (Esposti Ongaro et al., 2025), which represents a consolidated benchmark for simulating TLs in this volcanic setting.

The updated version~~one~~ introduces the following key improvements:

- **Improved Numerical Stability**. A new Riemann solver has been implemented. This enhancement stabilizes the numerical scheme, allowing for larger and more consistent time steps throughout the simulation and thus improving computational efficiency.
- **More Accurate Incompressibility**. The iterative solver enforcing the zero-divergence condition (i.e., fluid incompressibility) has been refined. It now employs a local convergence criterion, leading to a more robust and physically accurate solution, especially in complex flow conditions.
- **Layer-Independent Friction and Run-up**. A vertical linear viscosity model and a corrected formulation for the Manning friction have been introduced. Previously, friction was applied only to the bottom layer, making its total effect dependent on the number of layers used to discretize the water column. These new mechanisms ensure that the overall frictional dissipation and the resulting run-up behaviour are physically consistent and largely independent of the number of vertical layers chosen for the simulation.

The simulations contained in de' Michieli Vitturi et al. (2026a), relying on the 20 m topobathymetry, were performed using the 2021 version of the numerical model, as done for the comprehensive analysis presented in Esposti Ongaro et al. (2025). The simulations presented in de' Michieli Vitturi et al. (2026b) were carried out combining the updated 2025 version of the model with the more recent 10 m topobathymetry, leading to a database of scenarios based on improved numerical tools and higher-resolution data. In this work, we intentionally present and compare both datasets. The objective is not simply to supersede the previous results, but to highlight how model developments and new topographic data can influence hazard assessments. Moreover, as discussed in the final section, the newer dataset also presents some limitations (e.g. vegetation effects and partial resolution of urban features), and therefore cannot be considered consistently more accurate. Presenting both databases thus provides a more transparent view of the epistemic uncertainties associated with tsunami inundation modelling at Stromboli and frames the results within the context of evolving modelling capabilities. For the sake of brevity, and referring to their primary distinguishing feature, in the remainder of this paper we will refer to these two databases simply as the "Database A" (for de' Michieli Vitturi et al., 2026a) and the "Database B" (for de' Michieli Vitturi et al., 2026b).

2.3 Sensitivity analysis

To provide a first-order insight into the differences arising from the use of distinct Digital Elevation Models (DEMs) and numerical code versions, we performed a series of quantitative comparisons between pairs of simulations. These comparisons were designed to analyse separately the contributions of the topographic representation and of model developments, by varying one factor at a time. We focused on three key aspects of the inundation: the cell-by-cell water depth (in meters above ground), the overall inundated area, and the spatial agreement between the inundation patterns.

First, we conducted a direct, cell-by-cell comparison of the maximum water depth. The results are visualized through maps showing the absolute differences between two simulations, highlighting areas where one simulation predicts higher or lower water depths than the other. These maps are complemented by histograms that quantify the total area corresponding to specific intervals of water depth difference.

To quantify the spatial agreement between the inundated areas of two simulations (let's call them area A and area B), we employed the Jaccard index (J) and two complementary metrics, SIM_1 and SIM_2.

The Jaccard index (Jaccard, 1901) measures the similarity between the two areas and is defined as the ratio of the intersection to the union:

$$J = \frac{|A \cap B|}{|A \cup B|}$$

A value of J=1 indicates perfect overlap, while J=0 means no overlap.

The SIM_1 and SIM_2 indices~~exes~~ quantify the portions of the total inundated area that are unique to each simulation, respectively:

$$SIM_1 = \frac{A \backslash B}{|A \cup B|}; SIM_2 = \frac{B \backslash A}{|A \cup B|}$$

For clarity, we use the subscript “TOT” when these ~~indexes~~ indices refer to the entire island of Stromboli and “STV” when they refer exclusively to ~~the~~ Stromboli village. For example, J_{STV} represents the Jaccard index for the village area.

2.4~~3~~ Methodological framework for probabilistic hazard assessment

2.4~~3~~.1 Hazard curves, maps, and profiles

The two main types of products are hazard curves (more commonly known in statistics as survival functions), which quantify the hazard at specific points, and hazard maps, which provide a spatial representation of the hazard across the entire domain. A hazard curve provides ~~a~~ more complete information at a specific location regarding the hazard model. A hazard map provides a spatial overview of the variability and correlations represented by the hazard model. ~~A hazard map provides an overview for a fixed level of the spatial variability and correlations which the hazard model features~~. Both maps and curves have been produced considering for a 50-year time horizon~~a temporal framework of 50 years in the future~~, consistent with the outputs of the expert elicitation (Tadini et al., ~~submitted~~2026) and in line with similar studies of PTHA (e.g., Gibbons et al., 2020; Basili et al., 2021).

Hazard curves quantify, at a given location, the probability of exceeding different water depth thresholds, thus providing a quantitative site-specific hazard assessment. For practical purposes, we present and discuss these curves only for a selection of pre-defined points of interest. To avoid ambiguity in the terminology used in the maps and curves, we distinguish between free-surface elevation, measured relative to mean sea level, and water depth, measured relative to the local ground surface. Maximum free-surface elevation denotes the maximum positive free-surface elevation at a marine location, whereas inundation height (or inundation elevation) denotes the maximum elevation reached by the free surface over initially dry land, also relative to mean sea level. Water depth is instead the vertical thickness of water above the local ground surface. Unless otherwise stated, the probabilistic maps and hazard curves presented in this study refer to maximum water depth above ground.

The probabilistic inundation maps fall into two complementary categories:

- Probability of Exceedance Maps. For a given water depth threshold (e.g., 0.5 m), this product visualizes the probability that the threshold will be exceeded at least once over the next 50 years. Because this probability is itself uncertain due to epistemic uncertainties in source parameters (see Tadini et al., ~~submitted~~2026), we do not produce a single map but rather a distribution of possible outcomes. We present summary maps corresponding to different percentiles (e.g., 5th, 50th, and 95th) of this probability distribution. Each pixel in a given percentile map thus represents that specific level of confidence for the 50-year exceedance probability.
- Inundation Depth Maps for a Given Probability. Similarly, for a given 50-year probability of exceedance (e.g., 10%), this product shows the corresponding inundation depth. This depth is also uncertain. Consequently, we present percentile maps (5th, 50th, and 95th) that illustrate the range of possible inundation depths for that specific probability level. Each pixel's value in these maps represents the water depth that has the specified probability of being equalled or exceeded at least once over the next 50 years, at a given confidence level (percentile).

These two map types can be understood as different views of the underlying hazard curve computed for each pixel. A probability exceedance map is equivalent to taking a vertical slice through the hazard curves at a fixed water depth and plotting the corresponding probabilities. Conversely, an inundation depth map is equivalent to taking a horizontal slice at a fixed probability and plotting the corresponding water depths.

The maps produced and shown in the following sections refer to specific water depth values, probabilities, and percentiles. These values are as follows:

- water depth ~~heights~~thresholds: 0.1, 0.2, 0.5 and 1 m. The use of water depth (or inundation/flow depth) to derive hazard maps and curves has already been used in other tsunami hazard studies, for instance in Lorito et al. (2015) and Woessner and Farahani (2020). In this latter study, water depth thresholds of 0.5, 1, 5 and 10 m are chosen based on engineering considerations and fragility/vulnerability functions. For our Stromboli study case, we also used smaller thresholds (0.1 and 0.2 m) to take into account the small scale of the investigated area. We also note that 0.5 m water depth is potentially capable of dragging away adults (Kurisu et al., 2018);
- probabilities: 2% and 10%. These values have been used in other tsunami probabilistic hazard assessment studies (e.g., Gibbons et al., 2020; Fukutani et al., 2021; Ramos et al., 2025);
- percentiles: 5th/50th/95th. We chose these percentiles to be consistent with the outputs of the elicitation (Table 1 and Tadini et al., ~~submitted~~2026), although in similar PTHA studies slightly different values are used (e.g., 2nd, 50th, 98th in Gibbons et al., 2020);
- six specific sites, selected to represent critical infrastructure and locations of relevance for tourism and civil protection~~6 specific sites, chosen to be representative of the most critical points for infrastructures or from a touristic~~

~~point of view~~ (Figure 1). In particular, we have chosen the two main piers at the two villages of Ginostra and Stromboli ("Molo Ginostra" and "Molo Scari", respectively), the main power plant of the island ("Centrale ENEL"), two touristic beaches ("Spiaggia Lunga" and "Scalo dei Balordi") and a designated civil-protection waiting area located outside the area inundated by the 2002 tsunami~~a signal for waiting area positioned by Italian Civil protection in a safe area outside the inundation of the 2002 tsunami~~ ("Area di attesa Ficogrande"; Bonilauri et al., 2021).

To generate the probabilistic maps for a fixed water depth threshold, those corresponding to a given exceedance probability and the hazard curves, we follow a procedure in line with standard PTHA methodologies (e.g., Grezio et al., 2017; Volpe et al., 2019; Selva et al., 2021). The full approach is described in Text S1 from Supporting Information. In addition to hazard curves and maps, we extracted hazard profiles from the probabilistic inundation maps to analyse in detail the hazard variability within Stromboli village. The profiles were sampled on the 20m DEM along the 15-m isohypse, which Bonilauri et al. (2021) proposed as a potential lower boundary of the tsunami safe zone. That contour was derived from the maximum run-up of the 2002 tsunami (roughly along the 10-11 m isoline; Tinti et al., 2006a), with an added uncertainty margin of 5 m. To ensure a consistent comparison between model setups, the same contour line was used to extract hazard profiles from both the Database A and Database B results. Elevation differences between the two DEMs along this line are shown in Figure 2.

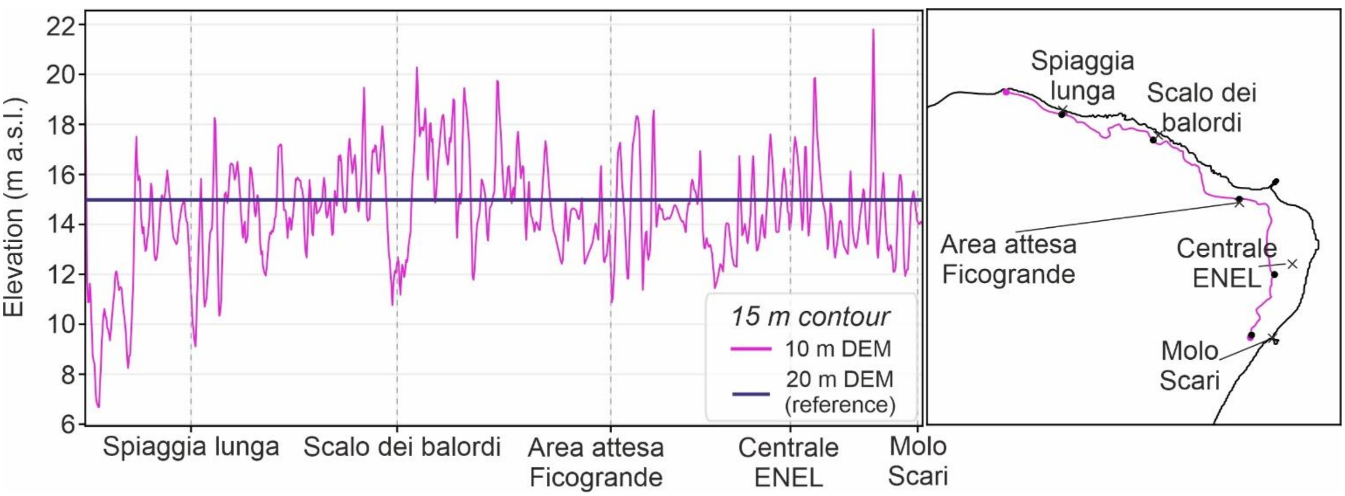

Figure 2. Left: elevation sampled from the 10 m DEM (purple line) along the planimetric path of the 15 m isoline extracted from the 20 m DEM. The blue horizontal line represents the constant 15 m elevation of the reference contour in the 20 m DEM.~~Left: Topographic profile extracted from the 10m DEM (purple line) along the 15 m isoline of the 20m DEM (blue line).~~ Vertical dashed lines correspond to the closest point along the 15 m isoline (black dots in the map to the right) to 5 out 6 sites where hazard curves have been developed (black crosses in the map to the right).

2.4~~3~~.2 Integration with expert elicitation outcomes

The integration of elicited probabilities with the deterministic simulation database requires addressing two key methodological challenges:

1. Treatment of the unbounded volume interval, as the probability for landslides of class V4 (volumes > 30×10^6 m^3) does not have an upper limit.
2. Discretization of interval probabilities, as it is necessary to partition the probabilities of the position/volume intervals defined in the elicitation among the discrete scenarios that fall within or near each range in our simulation database.

Regarding point (1), we adopted two distinct approaches to address the unbounded nature of the highest volume class (V4, > 30×10^6 m^3), resulting in two separate sets of probabilistic maps and hazard curves:

- Approach A (1-30 × 10^6 m^3 volume range). This approach entirely excludes the V4 class from the analysis. The elicited probabilities for the three bounded volume ranges (1–5, 5–14, and 14–30 × 10^6 m^3) were renormalized so that their sum equals 1. This method provides a probabilistic assessment conditional on the landslide volume in the range 1-30 × 10^6 m^3.
- Approach B (≥ 1 ~~m^3~~ × 10^6 m^3 volume range). This approach includes the V4 class (> 30×10^6 m^3) by assigning its entire elicited probability to a single volume in this interval, which was chosen to be 40×10^6 m^3. Although a simplification, this choice is consistent with the power-law landslide scaling described by Brunetti et al. (2009) and discussed for Stromboli by Tadini et al. (~~submitted~~2026), as well as with the current modelling framework~~this choice is consistent with both the power-law landslide scaling law described in Brunetti et al. (2009) and discussed for the Stromboli case in Tadini et al. (submitted), but also with the current modelling framework~~. Firstly, landslide volumes significantly larger than 40×10^6 m^3, when initiated from higher elevations, would likely extend beyond the morphological boundaries of the Sciara del Fuoco, involving material that would not slide along its main path. Secondly, very large-volume failures might involve different triggering mechanisms, such as deep-seated rotational slides, which would require a different initial geometry (e.g., incised into the slope) rather than the 'on-top' placement used in our simulations.

Regarding point (2), we use the outputs of the CM method (see Section 2.1), ~~that~~which consist of a set of 10,000 probability values for each target question of Table 1. We also adopt a specific procedure to derive probabilities for each specific volume/position interval, which ~~is extensively illustrated~~described in detail in Text S1 ~~from~~ of the Supporting Information. The core of this approach is to sample a series of hypothetical scenarios, each characterized by a defined position, volume, and density, from each interval and map each scenario to the closest available simulation in the corresponding database subset ~~The core of this approach is to sample from each intervals a series of hypothetical scenarios (with a defined position/volume/density), and to map each of this scenario to the closet available simulation in the corresponding database~~

subset (. Figure 3 illustrate this mapping processes for the volume range 1-30 × 10^6 m^3). The probability of each interval is then equally partitioned among the hypothetical scenarios that fall within each interval.

The final output of this procedure consists of two distinct sets of probability vectors, each containing 286 (volume range 1-30 × 10^6 m^3) or 308 (volumes ≥1 × 10^6 m^3) probability values.

The probabilities derived so far are conditional on the occurrence of a single tsunamigenic landslide within the SdF. To convert these into absolute probabilities over a 50-year time horizon, we account for the expected frequency of events by incorporating the 10,000 sampled values from elicitation questions TQ3 (number of events in 50 years, N_{50}) and TQ4 (percentage within the SdF, P_{SdF}). For each of the 10,000 sampling steps, we compute the expected number of events as $n = N_{50} \times P_{SdF}$ and then calculate the corresponding 50-year exceedance probability at every pixel. Because n is generally not an integer, we approximate its effect using the two nearest integers, N_{low} and N_{up}. The single-event conditional exceedance probability at each pixel is first used to compute the probabilities, as [$P(k) = 1 - (1 - p)^k$], of at least one exceedance assuming N_{low} and N_{up}, respectively. The final 50-year exceedance probability is then obtained as a weighted average of these two values. Repeating this procedure for all 10,000 realizations yields a distribution of 10,000 values for the 50-year exceedance probability at each pixel.

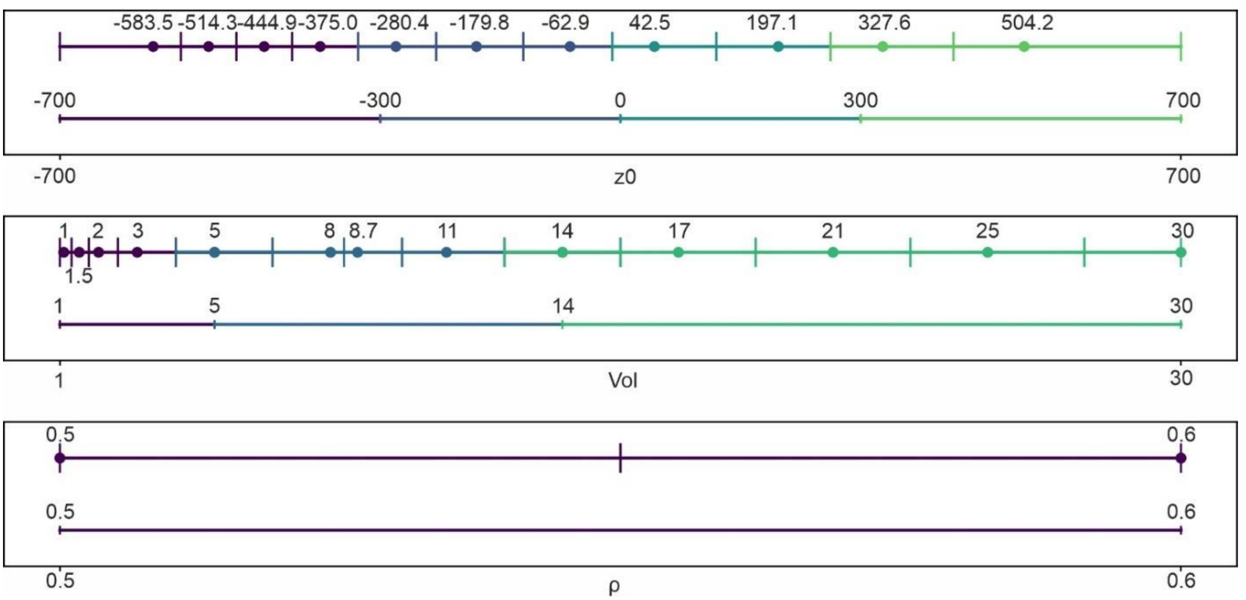

Figure 3 Comparison between positions (z_0 – top panel), volumes (Vol – middle panel, 1–30 × 10^6 m^3 range) and density contrast (ρ – bottom panel) for the simulations (upper straight line in each panel) and the ranges derived from the elicitation (lower straight line in each panel). For all upper straight lines, each simulated position/volume/density is marked by a circle, while the vertical lines indicate the segments (of the lower straight lines) associated with the corresponding circle (during the sampling of z_0, Vol, and ρ).

3 Results

3.1 Sensitivity of inundation to different DEM resolutions and code versions

To assess the differences arising from the use of distinct Digital Elevation Models (DEMs) and numerical code versions separately, we performed several~~few~~ comparisons ~~related~~ for to a single scenario, ~~that is~~namely a large-volume landslide (30 × 10^6 m^3) with a density of 2000 kg/m³, originating from a high-elevation subaerial position (P0). This scenario was chosen as it produces one of the most significant inundations and is therefore well-suited to highlight the differences between the model setups. The analysis focuses on the inundation within ~~the~~ Stromboli village and combines qualitative observations of the maps (Figure 4) with quantitative assessments from Jaccard ~~indexes~~ indices (Table 2) and water depth difference histograms.

The main differences are observed when using the same version of the code (2021 version) and comparing the old and new DEMs, both at 10m (Fig. 4a) and at 20m (Fig. 4b) resolutions. The inundation map for these cases reveals a complex pattern of differences. Firstly, within the commonly inundated area, two fundamentally divergent behaviours are evident, represented by the intense red and blue colours. These indicate large zones where the water depth differs by several meters between the two simulations. The corresponding histogram confirms this divergence, showing a strongly bimodal distribution with peaks in the [-3.16, -1.0] m and [1.0, 3.16] m bins. In addition to these differences in water depth, a second critical feature is the presence of extensive black areas, which indicate that the OLD DEM produces a much larger inundation footprint, especially in the inland portions of the village. A major contribution to these differences comes from the changes in the coastline that occurred between the acquisition dates of the two DEMs ~~changes in the coastline occurred in the time span between the two DEMs acquisition,~~ which is particularly evident for the Ficogrande and Scari beaches. It is interesting to observe that, although significant erosion occurred at both locations ~~despite for both the locations a significant erosion occurred,~~ for Ficogrande this results in a decrease in the maximum water depth (which also prevents the inundation of the area behind, shown in black in Figure 4a and 4b), while for Scari the erosion results in an increase in maximum water depth (red in Figure 4a and 4b). Differences in inundation for ~~the~~ Stromboli village are quantitatively confirmed by the Jaccard index (J_{STV} = 0.645 at 20m, 0.709 at 10m), which indicates poor spatial agreement, and by the fact that the area inundated exclusively by the OLD DEM amounts to either 27.0% (10m) or 34.3% (20m) of the total. Conversely, areas inundated only by the NEW DEM are negligible (1.2% at 20m and 2.1% at 10m).

In contrast, the impact of updating the numerical code from version 2021 to 2025 is more subtle, though still significant. On the same 20m DEM (Fig. 4c), the two code versions produce very similar inundation patterns, as confirmed by a high Jaccard index (J_{STV} = 0.917). The older 2021 version has a slightly larger footprint, inundating an exclusive area of just 31,451 m² (6.1%), which appears as thin black lines at the inundation margins. The water depth differences are also modest, with the histogram showing peaks for differences in the range of tens of centimetres.

However, the effect of the code update becomes much more pronounced on the 10m NEW DEM (Fig. 4d). While the difference in inundated area remains small (the 2021 version inundates an exclusive area of 16,225 m², or 5.5%), the impact on water depth is substantial. The histogram for this case has more pronounced peaks in the [-3.16, -1.0] m and the [1.0, 3.16, 1.0] m bins.

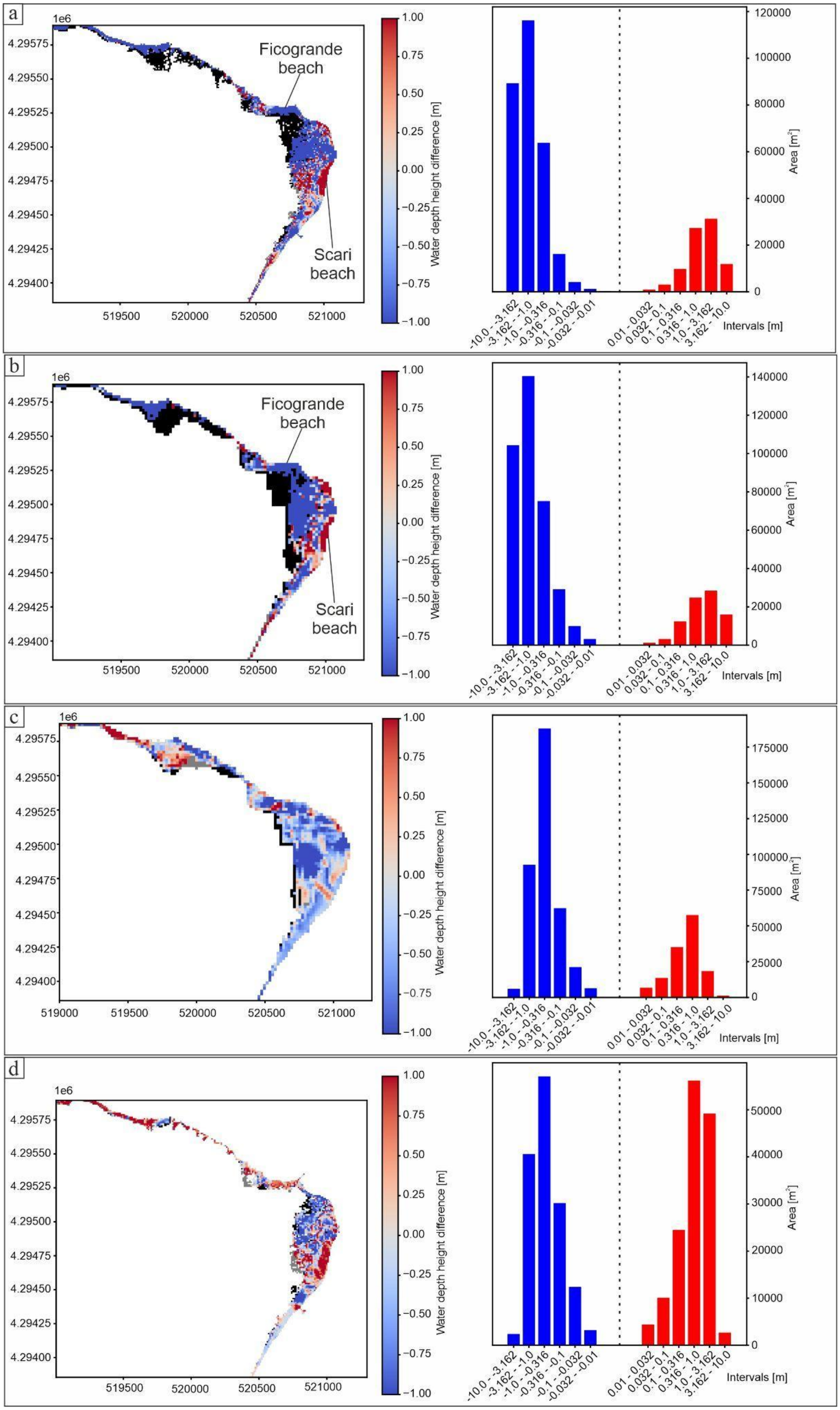
a
1e6
Ficogrande beach
Scari beach
Water depth height difference [m]
Area [m²]
Intervals [m]
b
1e6
Ficogrande beach
Scari beach
Water depth height difference [m]
Area [m²]
Intervals [m]
c
1e6
Water depth height difference [m]
Area [m²]
Intervals [m]
d
1e6
Water depth height difference [m]
Area [m²]
Intervals [m]

Figure 4 Comparison between simulations. a) P0-30 × 10^6 m^3, 10m NEW vs 10m OLD; b) P0-30 × 10^6 m^3, 20m NEW vs 20m OLD; c) P0-30 × 10^6 m^3, two versions of the code for 20m OLD DEM; d) P0-30 × 10^6 m^3, two versions of the code for 10m NEW DEM. For maps in left panels, grey pixels indicate areas inundated by~~where~~ SIM_1 ~~invades and~~but not by SIM_2~~ does not invade~~, while black pixels indicate areas ~~where~~ inundated by SIM_2 ~~invades while~~but not by SIM_1~~ does not invade~~. In the right histograms, the vertical dashed line separates blue bins, where the water depth of SIM_1 is smaller than that of SIM_2 (i.e. negative difference), and red bins, where the water depth of SIM_1 is larger than that of SIM_2 (i.e. positive difference). Please note that the vertical scales for the histograms are different, while the horizontal bins are the same for all the plots.

Table 2 Jaccard indices~~exes~~ to compare different simulations for Stromboli Island (TOT) and Stromboli village (STV). In the first column, "OLD" refers to the DEM used in de' Michieli Vitturi et al. (2026a) (both at its 20 m resolution and at 10 m resolution, obtained before the downsampling described in Section 2.2), while "NEW" refers to the DEM used in de' Michieli Vitturi et al. (2026b) (both at its 10 m resolution and at 20 m resolution, obtained with a downsampling)

DEM	Code version	AREA |AB| Island/village	J_{TOT}	J_{STV}	$SIM_{1,TOT}$	$SIM_{1,STV}$	$SIM_{2,TOT}$	$SIM_{2,STV}$
Sim_1: 10 m (NEW) Sim_2: 10 m (OLD)	Sim_1: 2021 Sim_2: 2021	723,800 m^2/ 379,400 m^2	**0.740**	**0.709**	**0.036**	**0.021**	**0.224**	**0.270**
Sim_1: 20 m (NEW) Sim_2: 20 m (OLD)	Sim_1: 2021 Sim_2: 2021	773,200 m^2/ 457,600 m^2	**0.663**	**0.645**	**0.057**	**0.012**	**0.280**	**0.343**
Sim_1: 20m (OLD) Sim_2: 20m (OLD)	Sim_1: 2025 Sim_2: 2021	866,800 m^2/ 515,600 m^2	**0.909**	**0.917**	**0.020**	**0.022**	**0.071**	**0.061**
Sim_1: 10m (NEW) Sim_2: 10m (NEW)	Sim_1: 2025 Sim_2: 2021	602,500 m^2/ 295,000 m^2	**0.906**	**0.888**	**0.043**	**0.057**	**0.051**	**0.055**

3.2 Hazard maps, curves and profiles

3.2.1 Hazard maps with fixed water depth

Probabilistic maps for a fixed exceedance threshold of 0.5 m obtained from Databases A and B are presented in Figures 5 and 6, respectively~~Probabilistic maps for a fixed exceedance threshold of 0.5 m are presented in Figures 5 and 6~~. These two figures allow for a comparison of the combined effects of code version (2021 vs 2025), DEM resolution (20m vs 10m) and landslide volume range (1-30 × 10^6 m^3 vs ≥1 × 10^6 m^3). With respect to the inundated areas, the effects of the different code versions are smaller than those resulting from the DEM resolution (see Section 2.2) and are not discussed here.

Despite the differences between these setups, all maps show a consistent overall hazard pattern. The area by far most exposed is the northeastern coast, where the main village of Stromboli is located. This is due to the combination of its exposure to tsunami energy diffracting from the Sciara del Fuoco (northwestern flank) and, crucially, its gentle coastal plain morphology, which allows for significant inland inundation. In contrast, other exposed coastlines like Ginostra (southwest) show a more limited hazard footprint due to their steeper topography. The hazard gradient is consistently sharp across the island; the probability of inundation, represented by colours from yellow (high) to dark blue (low), decreases rapidly with increasing elevation away from the coast.

The comparison between the percentile maps within each row provides a powerful visualization of the uncertainty propagated from the expert elicitation. The 5^{th} percentile map represents the lower uncertainty bound, while the Median map shows the central estimate. The 95^{th} percentile map outlines a more severe, "1-in-20" case, meaning there is only a 5% chance that the hazard will be even greater. Although this represents a less probable outcome than the median, its likelihood is by no means negligible, making it a useful reference for robust hazard assessment and risk mitigation planning. A critical result, common to all four setups, is that in the 95^{th} percentile scenario, vast portions of the village's coastal area are coloured bright yellow. This indicates that, assuming such condition, these areas are almost certain to be inundated by at least 0.5 m of water over the next 50 years.

Beyond these general patterns, the figure allows for a detailed comparison of the impact of the different modelling choices. Regarding the effect of DEM resolution, as expected, these probabilistic results confirm the findings from the deterministic comparison shown in Figure 2. In both comparisons, the Database A (DEM resolution 20m, Fig. 5) produces a more extensive hazard footprint, with probabilities of inundation extending further inland compared to the Database B (DEM resolution 10m, Fig. 6). The 10m DEM, by resolving small-scale natural obstacles, confines the hazard more closely to the coastline, offering a more accurate, albeit less conservative, depiction of the inundation extent.

Similarly, the effect of including larger volume landslides is evaluated by comparing Figure 5a-b and Figure 6a-b. In both cases, incorporating the 40 × 10^6 m^3 scenarios (Figs. 5b and 6b) increases the overall hazard.

In summary, the most conservative hazard assessment, in terms of spatial extent and probability values, is provided by the setup in the Database A, ≥1 × 10^6 m^3 range (Fig. 5b), while the least conservative is that of Database B, 1-30 × 10^6 m^3 range

(Fig. 6a). Presenting this matrix of results is therefore essential for transparently communicating not only the tsunami hazard but also the significant uncertainty associated with key modelling choices.

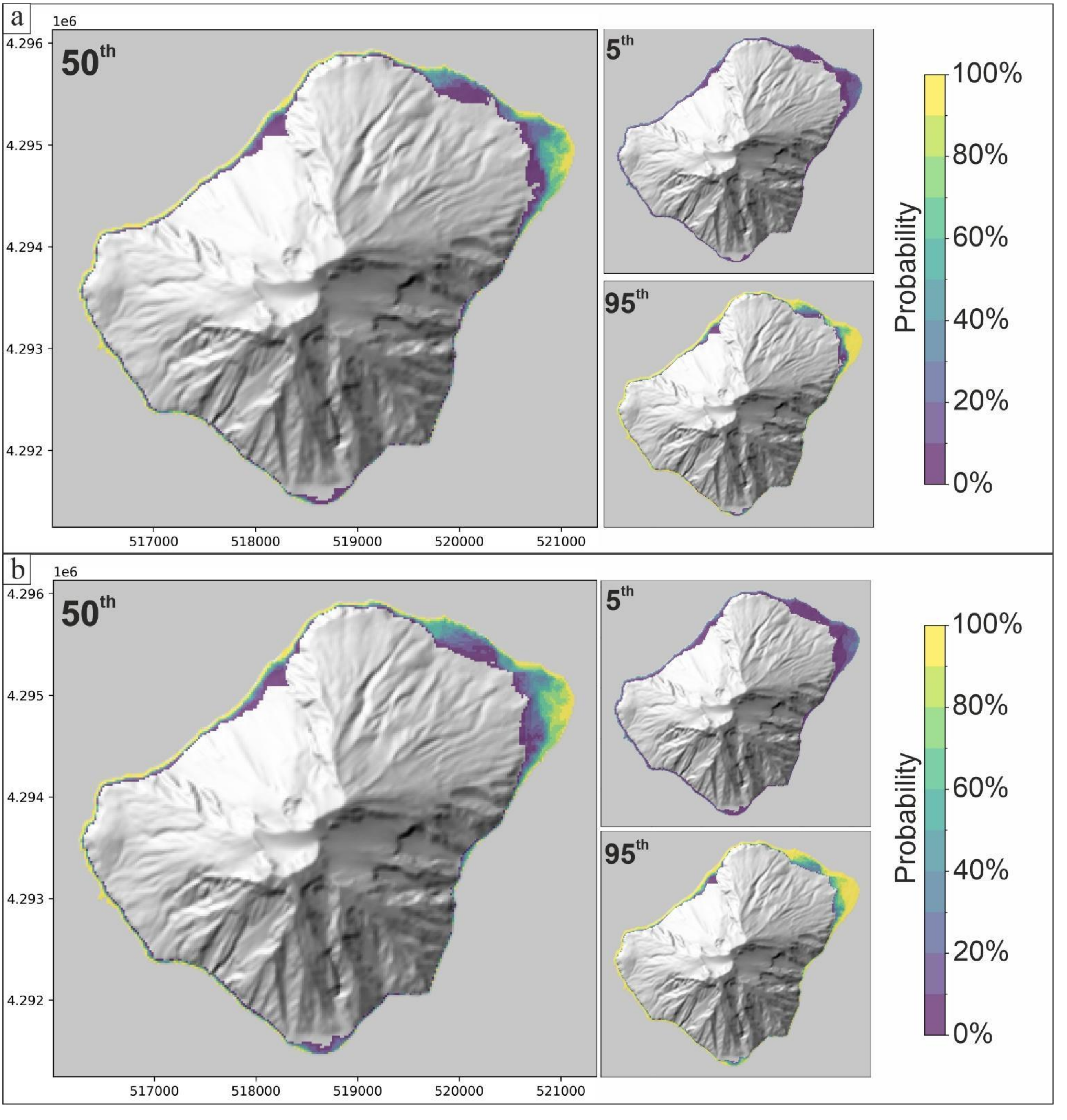

Figure 5. Probabilistic maps for exceeding a water depth of 0.5 m over a 50-year horizon for the Database A. (a) Volume range 1-30 × 10^6 m^3; (b) volume range ≥1 × 10^6 m^3.

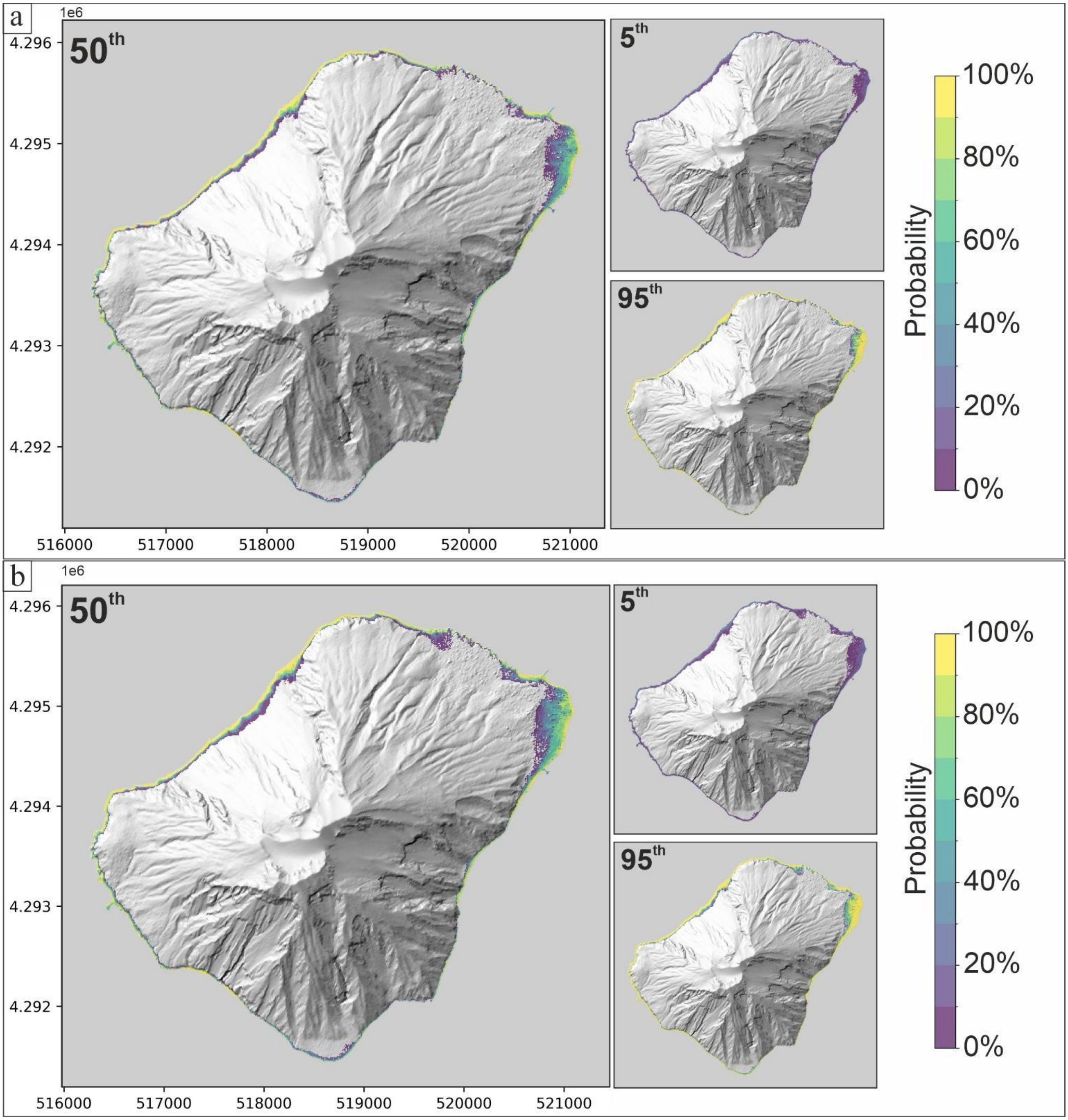

Figure 6. Probabilistic maps for exceeding a water depth of 0.5 m over a 50-year horizon for the Database B. (a) Volume range 1-30 × 10^6 m^3; (b) volume range ≥1 × 10^6 m^3.

To further investigate the hazard, we analysed the sensitivity of the probabilistic maps to the chosen water depth threshold. Figure 7 illustrates this by comparing the 50^{th} percentile probability map of the 0.5 m (Fig. 7c, same as Fig. 6b) for three different exceedance thresholds (Fig. 7a, b, d): 0.1 m, 0.2 m, and 1.0 m. These maps were all generated using a setup combining the Database B with the ≥1 × 10^6 m^3 volume range. The full maps for these thresholds are displayed in Figs. S1-S6.

The comparison reveals a striking result: the overall footprint of the area with significant hazard probability remains remarkably stable, showing only minor contractions as the water depth threshold increases from 0.1 m to 1.0 m. Although subtle differences exist, with a slightly larger and more uniform hazard area for the 0.1 m threshold as expected, the primary boundaries of the inundated zone do not change substantially.

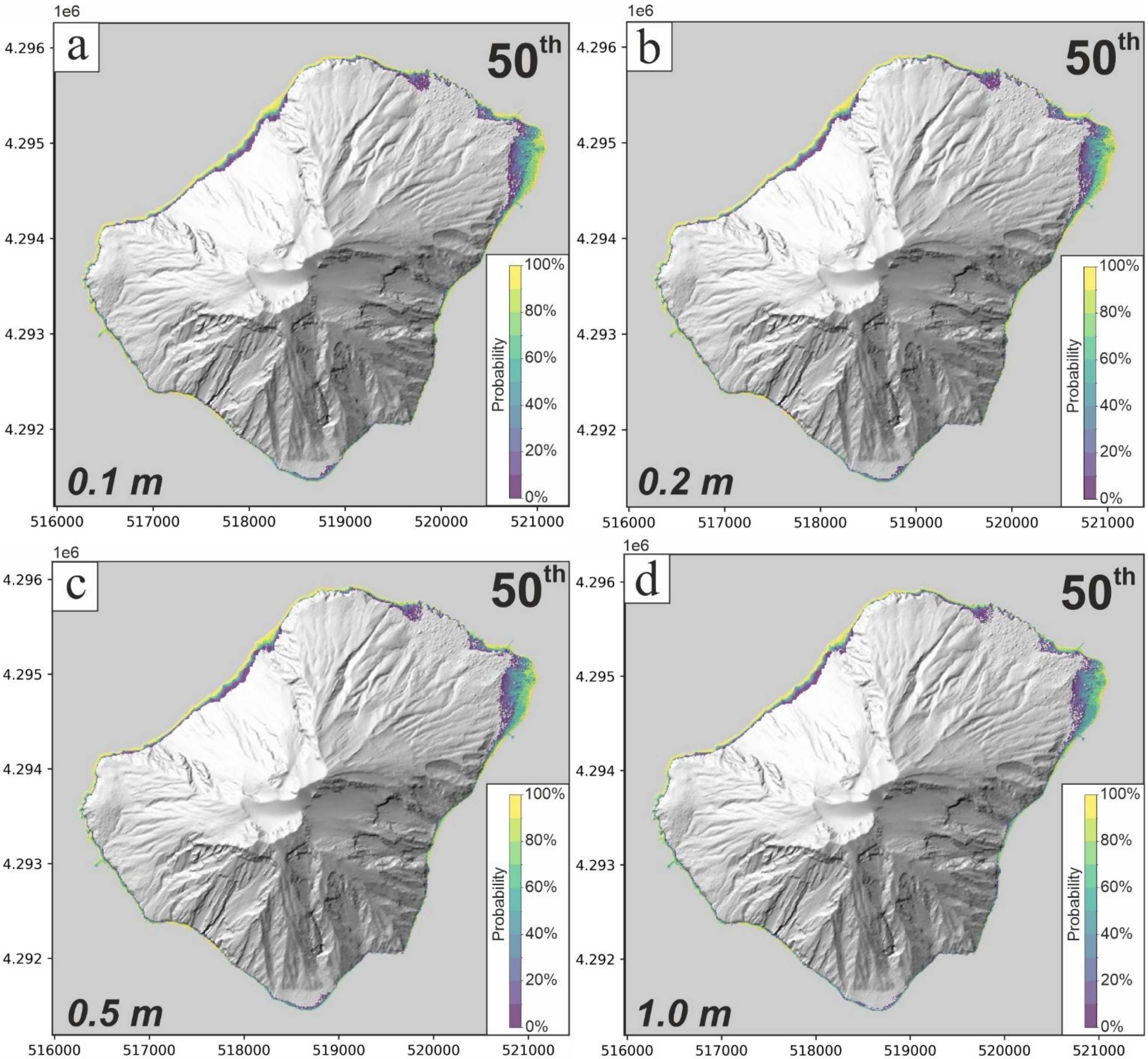

Figure 7. Sensitivity of the 50th percentile probabilistic inundation map to the water depth threshold. The maps show the 50-year probability of exceeding (a) 0.1 m, (b) 0.2 m, (c) 0.5 m, and (d) 1.0 m, all for the Database B and $\geq 1 \times 10^6$ m^3 volume range setup.

3.2.2 Hazard maps with fixed probability

The probabilistic inundation maps corresponding to a 10% exceedance probability in 50 years, obtained from Databases A and B, are shown in Figures 8 and 9, respectivelyThe probabilistic inundation maps corresponding to a 10% exceedance probability in 50 years are shown in Figures 8 and 9. Those corresponding to the 2% exceedance probability are displayed in Figs. S7-S8 from the Supporting Information. This type of map is particularly useful for planning purposes as it visualizes the expected inundation intensity for a given likelihood level.

The three columns within each row effectively visualize the uncertainty associated with the water depth for this 10% probability level. The 5th percentile map represents a more moderate inundation scenario, with water depths generally below 1-2 meters even in the most exposed areas. The Median map shows a more significant inundation, with depths commonly exceeding 2 meters along the coast. The 95th percentile map depicts a far more severe scenario; for the same 10% probability, the expected water depths are higher, with water depth > 5 meters along the entire waterfront. This highlights the substantial uncertainty in the potential intensity of a "10% probability" event.

The most significant factor influencing the results is the DEM resolution, which primarily controls the spatial extent of the hazard. Comparing the maps generated with the Database A (20m DEM resolution, Fig. 8) to those with the Database B (10m DEM resolution, Fig. 9), it is evident that the former consistently produce a much larger inundation area for the same percentile and volume range. This effect is particularly pronounced in the 95th percentile maps, where the inundation from the Database A extends significantly further inland across the coastal plain. While the Database B provides a more heterogeneous and detailed inundation pattern, with corridors of deeper flow and shadow zones, its overall footprint is more constrained.

The inclusion of larger landslide volumes ($>30 \times 10^6$ m^3) also has a clear and significant impact, primarily on the intensity of the inundation. Comparing the results for the $1\text{-}30 \times 10^6$ m^3 range (Figs. 8a and 9a) with those including the 40×10^6 m^3 scenarios (Figs. 8b and 9b) reveals a striking increase in inundation severity. For the same 10% exceedance probability, the water depths in the lower two rows are significantly higher across all percentiles. The Median and 95th percentile maps, in particular, shift from showing predominantly 1-2 meters of water depth to > 5 meters of water depth. This demonstrates that including high-consequence events in the analysis drastically elevates the expected water depth for any given probability level.

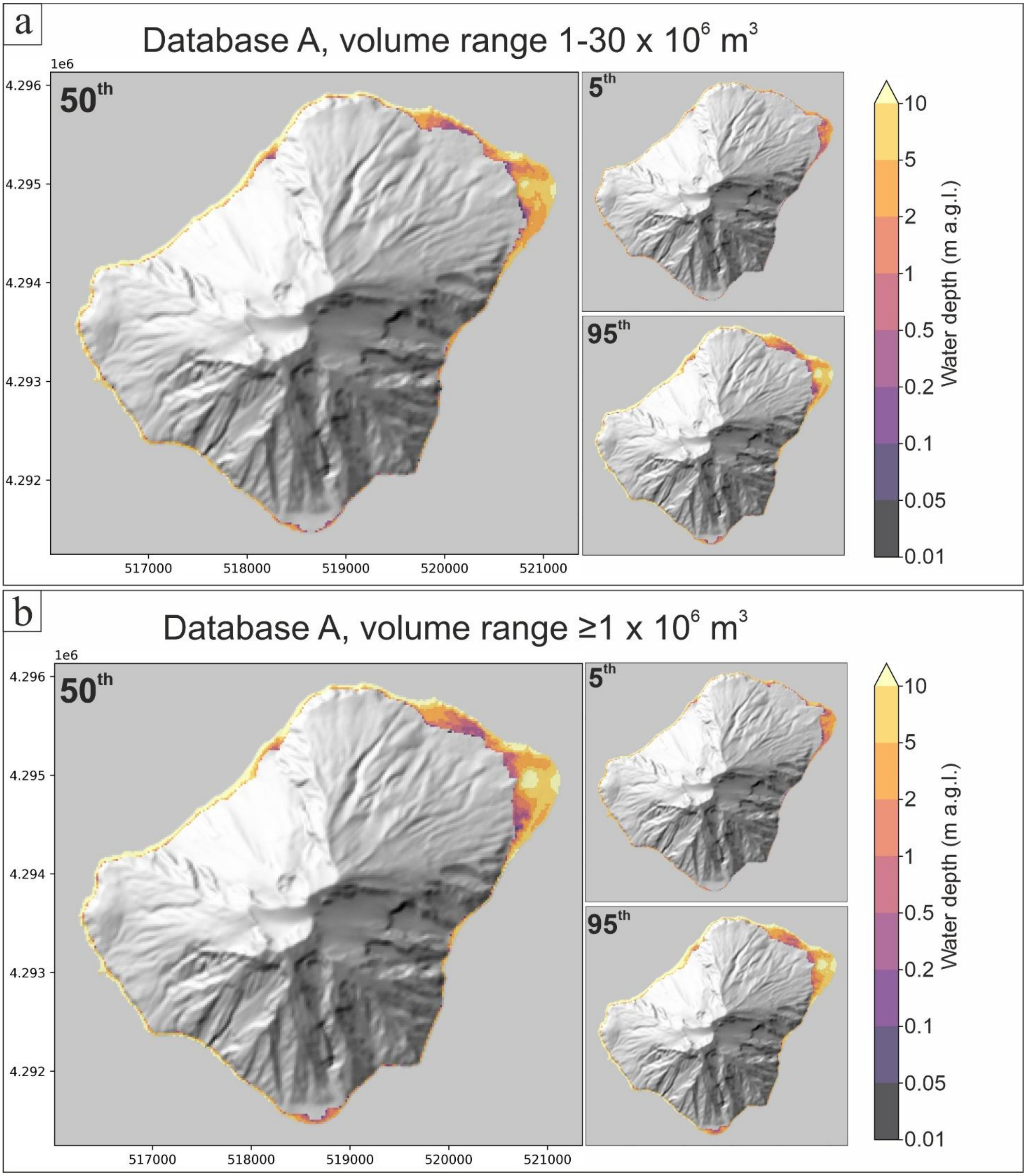

Figure 8. Probabilistic maps showing the inundation water depth corresponding to a 10% exceedance probability over a 50-year horizon for the Database A. (a) Volume range 1-30 × 10^6 m^3; (b) volume range ≥1 × 10^6 m^3.

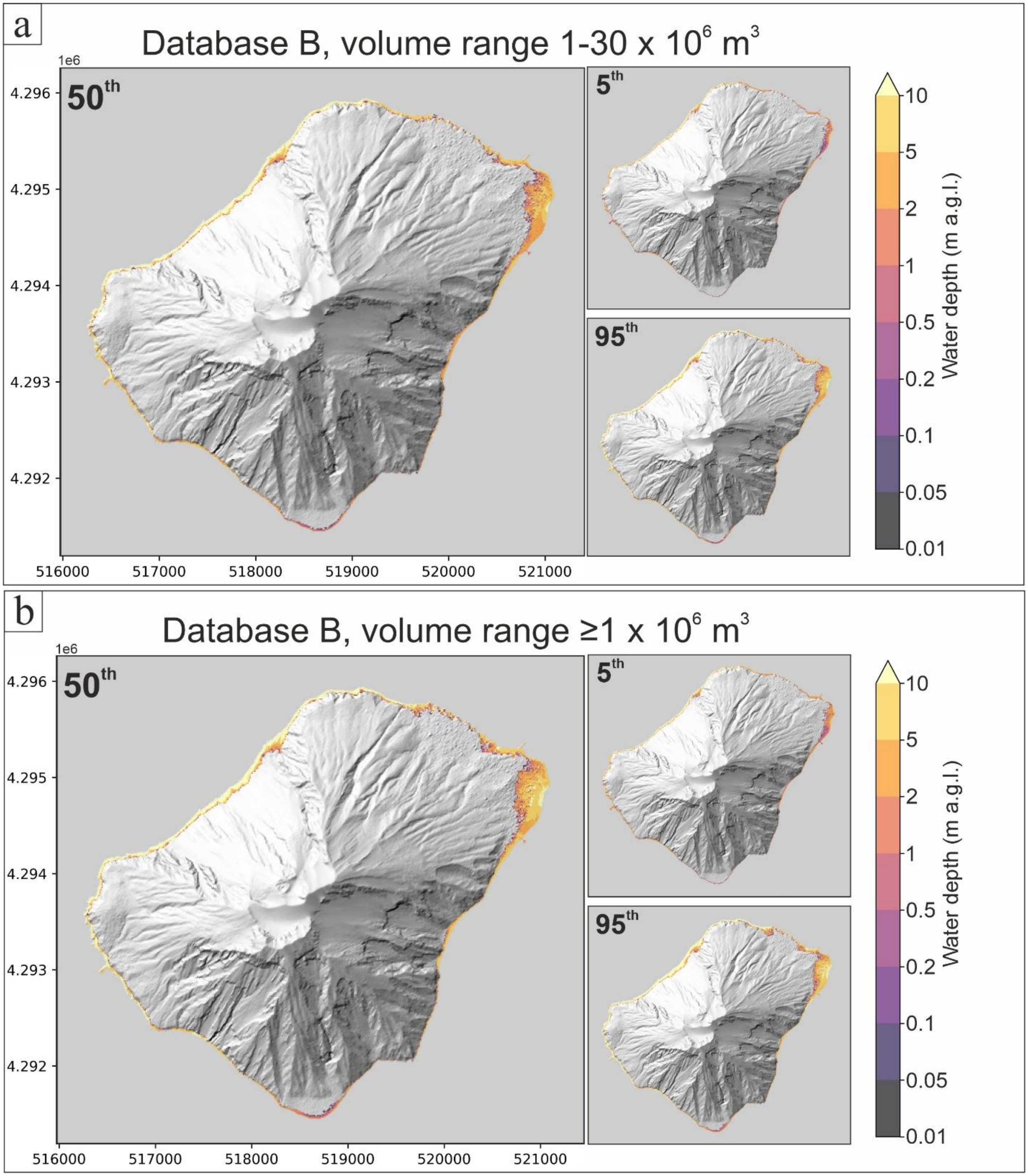

Figure 9. Probabilistic maps showing the inundation water depth corresponding to a 10% exceedance probability over a 50-year horizon for the Database B. (a) Volume range 1-30 × 10^6 m^3; (b) volume range ≥1 × 10^6 m^3.

To complete the analysis, we investigated how the expected inundation intensity changes for different levels of exceedance probability. Figure 10 compares the water depth maps for two different 50-year exceedance probabilities, 2% (Fig. 10a) and 10% (Fig. 10b), across all three statistical estimators: the 5th, 50th, and 95th percentiles (left, central, and right columns, respectively). All maps were generated using the most detailed setup (10m DEM with the $\geq 1 \times 10^6$ m^3 volume range).

The results reveal a complex, non-uniform sensitivity that depends on the percentile considered. For the 50th percentile and 95th percentile maps (central and right columns in Fig. 10), a striking saturation effect is observed. The inundation intensity is remarkably insensitive to the chosen probability level, with the maps for 2% and 10% probability being nearly identical. This suggests that for the median and reasonably pessimistic scenarios, the upper tail of the hazard curve is very steep. Once the analysis includes high-consequence events, a significant decrease in probability (from 10% to 2%) does not correspond to a significant increase in the predicted water depth.

This dual behaviour has profound implications for hazard assessment. For the 50th and 95th percentile maps, the hazard appears to reach a plateau, meaning that planning for a 10% probability event may already provide robust protection against much rarer tsunamis, or the other way around, that is planning for a better protection may be worthwhile as it adds a limited marginal cost. For the 5th percentile maps, however, the severity continues to scale with the rarity of the event. This highlights the complex nature of the hazard distribution, where the uncertainty tails behave differently from the central tendency.

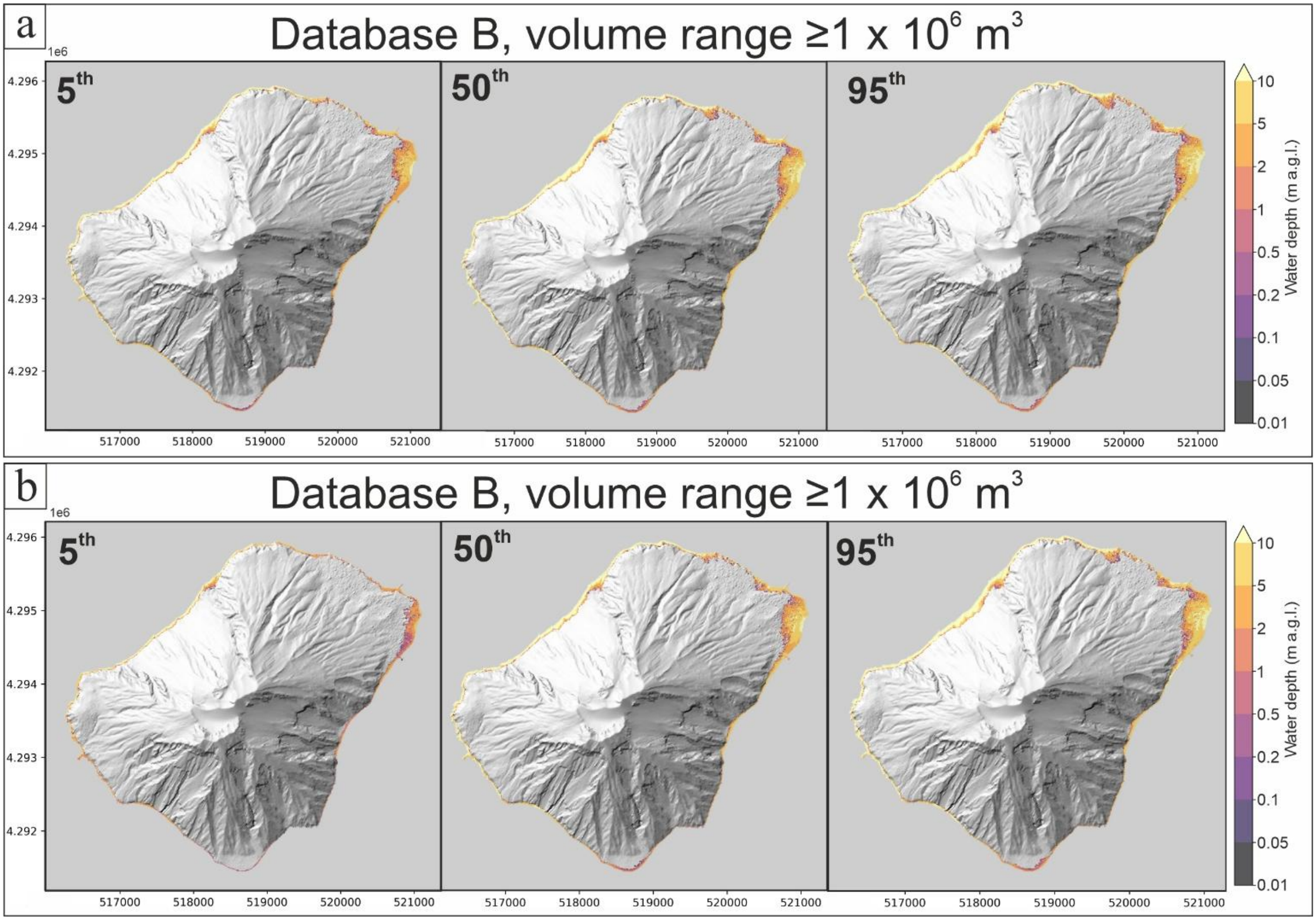

Figure 10. Effect of the exceedance probability level on the percentile inundation depth maps. All maps were generated using the ~~10m DEM~~Database B with the volume range ≥1 × 10^6 m^3 ~~landslide volume range~~. a) water depth for a 2% probability in 50 years; b) water depth for a 10% probability in 50 years.

3.2.3 Hazard Curves

A detailed, quantitative assessment of the tsunami hazard at specific locations is provided by hazard curves, which were generated for 6 points of interest around the island (see Fig. 1). In this section, we present and discuss the results for two representative sites within ~~the~~ Stromboli village: "Centrale ENEL", located directly on the waterfront and highly exposed, and "Area di attesa Ficogrande," situated further inland at a slightly higher elevation. In addition to their locations with respect to the coastline, they are interesting as they are the island power plant, and one of the assembly points to be used after evacuation, respectively. The hazard curves for these sites (Figures 11 and 12) plot the 50-year probability of exceeding a range of water depths and are presented for all four set of maps (Databases A and B, combined with the ~~and~~ 1-30 × 10^6 m^3 ≥1 × 10^6 m^3 volume ranges), showing the 5^{th}, Median, and 95^{th} percentile results. The hazard curves for the additional sites shown in Figure 1 are provided in Figs. S9-S12 from the Supporting Information.

These curves provide a synthesis of the hazard and its associated uncertainty. The vertical distance between the 5^{th} percentile (blue line) and the 95^{th} percentile (green line) illustrates the wide range of uncertainty in the exceedance probability for a given water depth, which often spans more than an order of magnitude. Similarly, the horizontal distance between these curves quantifies the uncertainty in the inundation water depth for a given probability level. For example, at the Centrale ENEL site for a 10% exceedance probability, the expected water depth could range from approximately 2 meters (5^{th} percentile) to over 6 meters (95^{th} percentile), highlighting the vast range of plausible outcomes.

The shape of the curves, particularly the steepness of their "roll-off" at higher water depths, is fundamental to understanding the nature of the hazard. For the Centrale ENEL site (Figure 11), the Median and 95^{th} percentile curves (orange and green lines) exhibit an extremely steep decay for low probabilities (<10%). This explains the "saturation effect" observed in the corresponding maps: in this steep portion of the curve, a large decrease in probability (e.g., from 10% to 2%) translates into only a minor increase in the associated water depth. Conversely, the 5^{th} percentile curve (blue line) has a much gentler slope, explaining why for this percentile, a similar decrease in probability corresponds to a much more significant increase in expected water depth.

The effect of the DEM is particularly evident at the “Area di attesa Ficogrande” site (Figure 12). While the Database A (20m DEM, top panels) predicts a non-negligible hazard, for Database B (10m DEM, bottom panels) no hazard curves are visible. This is because, at these locations, the maximum water depth does not reach the minimum inundation threshold of 0.01 m for any of the three percentiles considered (5^{th}, 50^{th}, and 95^{th}). These locations are therefore classified as not inundated in the probabilistic analysis. The absence of visible curves is thus a consequence of the simulated inundation pattern rather than a plotting artifact~~the curves generated with the Database B (10m DEM - bottom panels) drop to near-zero probability for any significant water depth~~.

The effect of including larger landslide volumes is also clear and systematic. In ~~all panels of~~ both F~~f~~igures 11 and 12, the curves for the $\geq 1 \times 10^6$ m^3 range (right panels~~columns~~) are consistently shifted to the right compared to those for the 1-30 $\times$ 10^6 m^3 range (left panels~~columns~~). This indicates, as expected, a higher hazard level, where any given exceedance probability corresponds to a greater water depth when high-consequence events are included in the analysis. It is important to note that since the x-axis is on a logarithmic scale, even a visually moderate shift in the right-hand part of the graph corresponds to a significant increase in the absolute water depth, often on the order of several meters. This shift is pronounced across all percentiles, underscoring the substantial contribution of larger, rarer events to the overall hazard assessment.

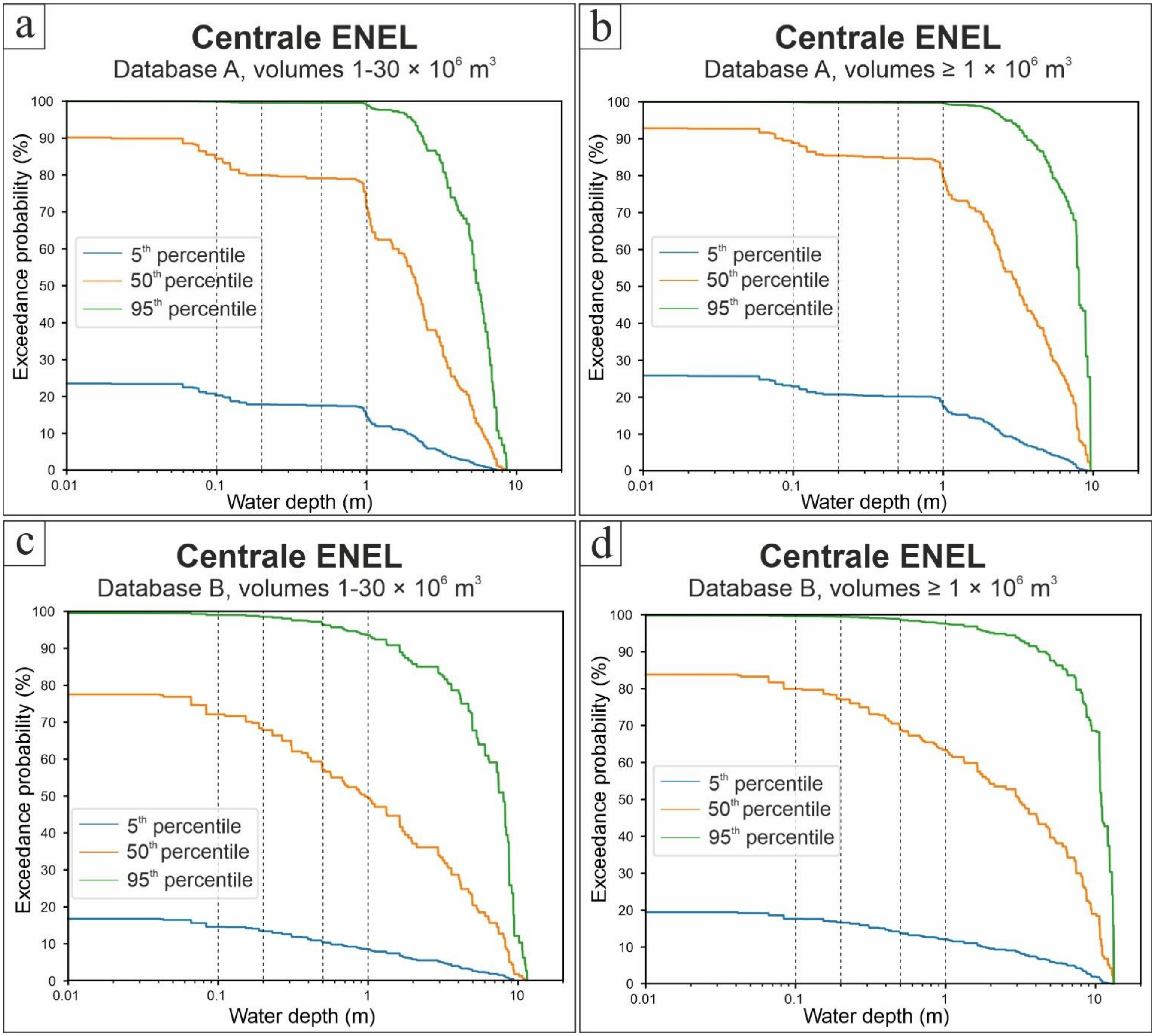

580 **Figure 11.** Probabilistic hazard curves for the "Centrale ENEL" site. The panels compare the results for the four different model setups: Database A (a-b), Database B (c-d), 1-30 × 10^6 m^3 volume range (a-c), and ≥1 × 10^6 m^3 volume range (b-d). Each panel shows the 50-year exceedance probability as a function of water depth for the 5th, 50th, and 95th percentiles of the hazard distribution. Vertical grey dashed lines correspond to the water depth thresholds used for map production (0.1, 0.2, 0.5 and 1 m).

585

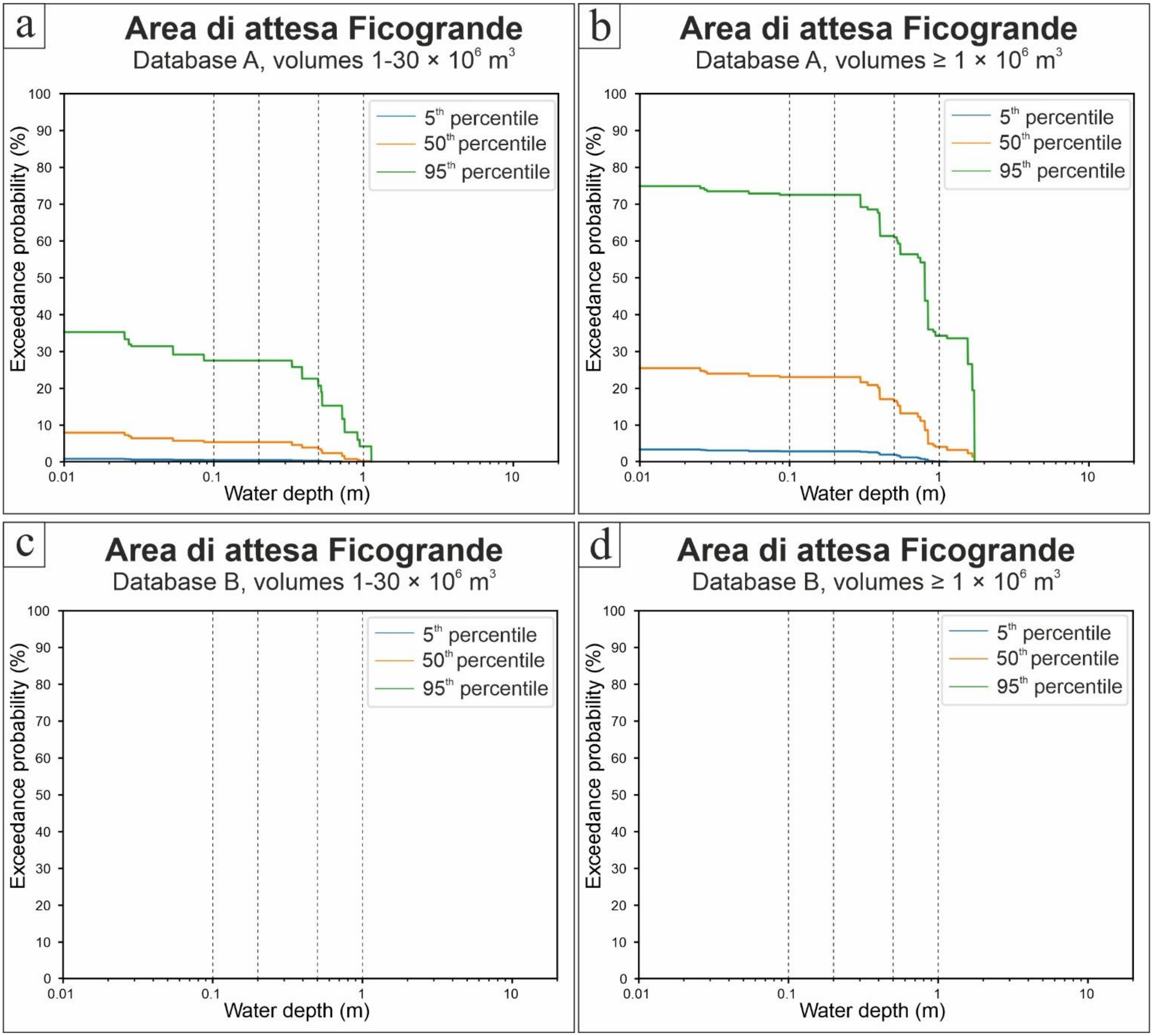

Figure 12. Probabilistic hazard curves for the "Area di attesa Ficogrande" site. The panels compare the results for the four different model setups: Database A (a-b), Database B (c-d), 1-30 × 10^6 m^3 volume range (a-c), and ≥1 × 10^6 m^3 volume range (b-d). Each panel shows the 50-year exceedance probability as a function of water depth for the 5th, 50th, and 95th percentiles of the hazard distribution. Note the drastic reduction in hazard for this inland site when using the Database B (c-d). Vertical grey dashed lines correspond to the water depth thresholds used for map production (0.1, 0.2, 0.5 and 1 m). Please note that no lines are plotted for Database B, because water depth < 0.01 m for the 5th, 50th and 95th percentiles.

3.2.4 Hazard profiles

Regarding the hazard profiles (Figures 13-14), the values from the 2D probabilistic maps (5th, Median, and 95th percentiles) were interpolated at a high number of points along this contour to generate a continuous 1D representation of the hazard. In each panel of the resulting figures, the thin, oscillating line represents the direct result of the interpolation, while the thicker dashed line shows a smoothed version of the same profile, which helps to visualize the underlying trend by filtering out high-frequency noise. We stress that the sites ~~corresponding to~~in the hazard ~~curves~~ profiles of Figs. 13-14 are not located along the 15 m isoline: rather, they are included just to provide an indication of the point along the isoline which is closest to the site of the hazard curve.

Figure 13 shows the resulting profiles for the probability of exceeding 0.5 m of water depth, comparing the Database A (Fig. 13a) with the Database B (Fig. 13b) both for the $\geq 1 \times 10^6$ m^3 volume interval. These profiles reveal that the probability of significant inundation is consistently high within the village, though with some localized variations. A dip is observed along the segment between "Scalo dei Balordi" and "Area di attesa Ficogrande". A more subtle decrease is visible east of "Area di attesa Ficogrande" while a more significant and progressive drop in probability occurs in the easternmost section, from "Centrale ENEL" to "Molo Scari".

In contrast, the profiles showing the water depth for a fixed 10% exceedance probability (Figure 14) exhibit a greater variability. Here, a clear decreasing trend in water depth is visible moving from west to east, away from the area of direct impact of the waves generated at the Sciara del Fuoco. This trend is smoother and more evident in the profiles from the Database A (Fig. 14a), while it is superimposed with high-frequency oscillations in the profiles from the Database B (Fig. 14b).

A key difference between the two sets of profiles is the frequency of the oscillations, which directly highlights the impact of the DEM resolution. The profiles derived from the Database B (panel b in both figures) consistently exhibit high-frequency oscillations that are much more pronounced than in the profiles from the Database A (panel a). This is a numerical artifact originating from the interpolation procedure. As the profile is traced along the 15 m isohypse~~isobath~~, the bilinear interpolation samples values from the underlying discrete grid of the probabilistic map. Each oscillation corresponds to the path crossing from one set of four grid cells to the next. Since the 10m DEM has a finer grid, these crossings occur more frequently, resulting in the observed high-frequency noise. The 20m DEM, being coarser, produces a smoother profile with lower-frequency oscillations, as the path remains within the same set of interpolating cells for a longer distance.

Finally, the profiles provide a quantitative measure of the uncertainty along the selected isoline. The vertical distance between the 5th and 95th percentile curves is substantial in all cases, reinforcing the wide range of plausible outcomes derived from the expert elicitation. This is particularly evident in Figure 14, where the 95th percentile water depth is often several times greater than the 5th percentile value for the same 10% probability, underscoring the large uncertainty in the potential intensity of the inundation. It should be noted that, for the profiles obtained for a fixed probability (Figure 14), despite the resolution-induced differences in signal smoothness, the spatial position of the relative peaks (local maxima) along the 15 m isohypse remains consistent between the two databases. This consistency indicates that the identification of the most exposed segments of the coast is robust and not heavily dependent on the specific model setup.

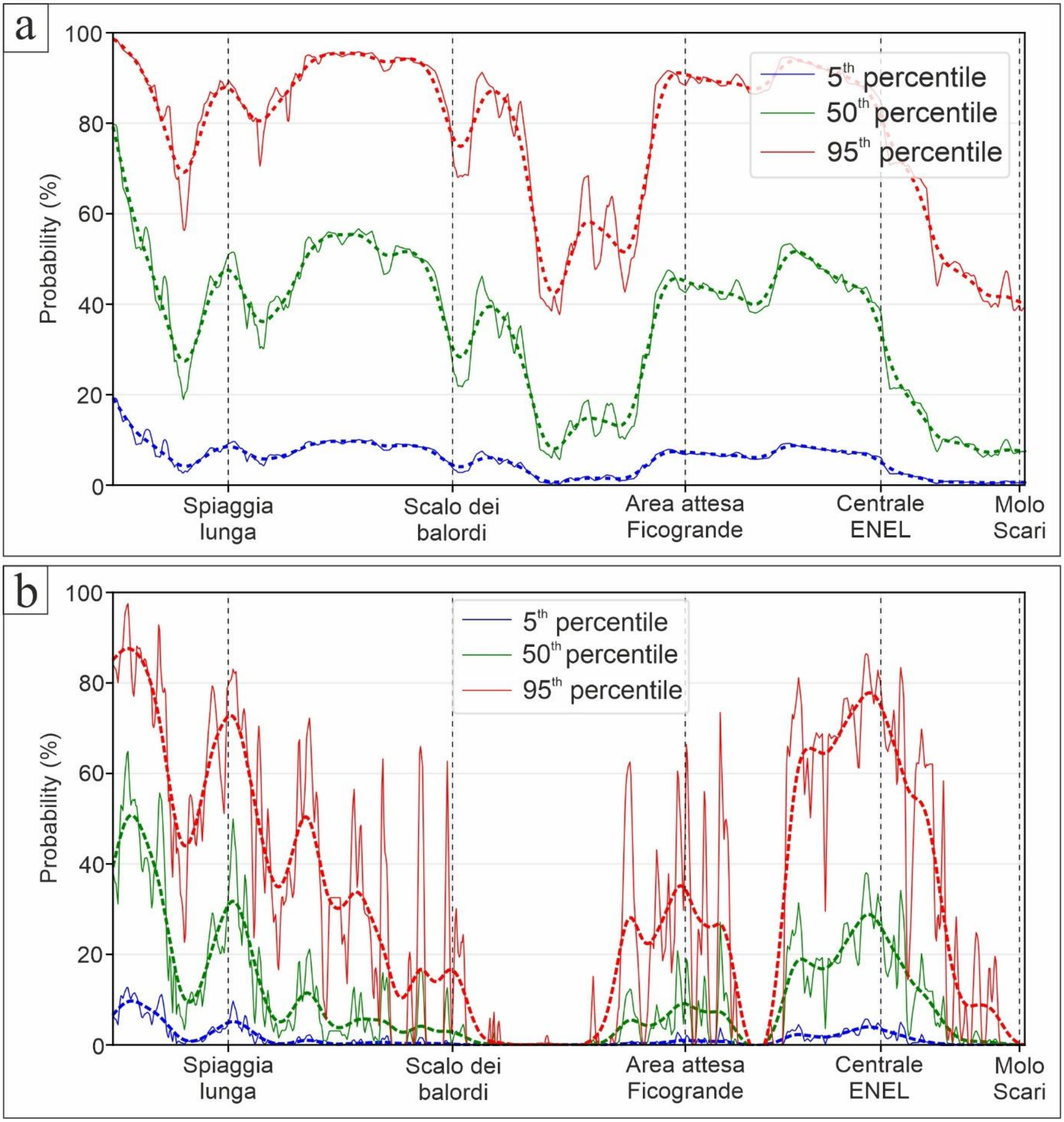

630 **Figure 13.** Profiles along the 15 m isoline of the 20m DEM (5th-50th-95th) for maps with water depth 0.5 m for a) Database A and b) Database B. Vertical dashed lines correspond to the closest point along the 15 m isoline (black dots in the map to the right) to 5 out 6 sites where hazard curves have been developed (black crosses in the map to the right; see Section 3.2.4).

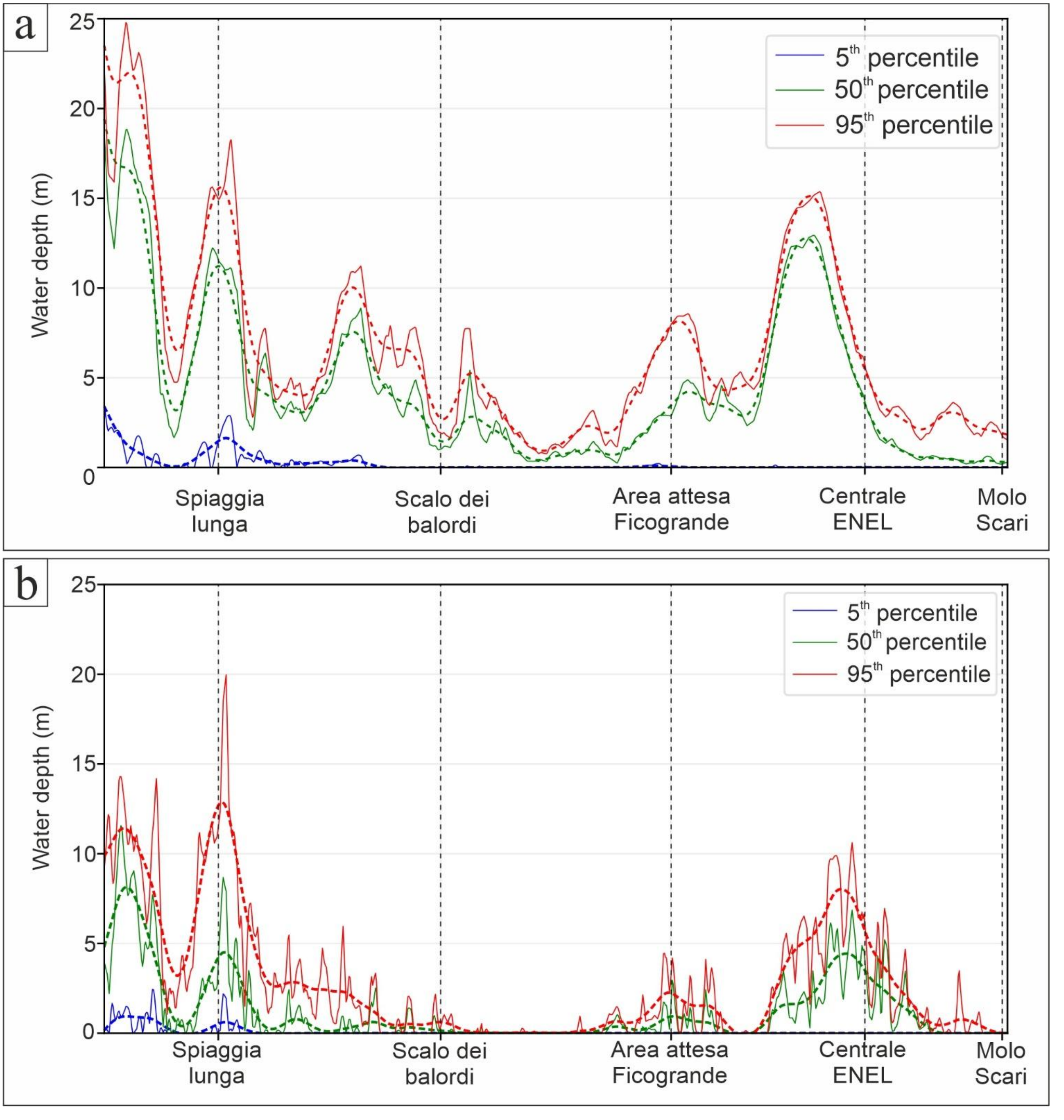

635 **Figure 14** Profiles along the 15 m isoline of the 20m DEM (5^{th}-50^{th}-95^{th}) for maps with probability 10% for a) Database A and b) Database B. Vertical dashed lines correspond to the closest point along the 15 m isoline to 5 out 6 sites where hazard curves have been developed (see Section 3.2.4).

4 Discussion

This study presents a first PTHA for Stromboli Island, stemming from potential landslides on the Sciara del Fuoco. As indicated in the companion paper of Tadini et al. (~~submitted~~2026), the importance of this study lies in the current incompleteness of a full PTHA for Stromboli Island. While ~~in fact~~ a PTHA from seismic sources is available for the Mediterranean Sea (Basili et al., 2018; 2021), it is currently missing from local sources such as landslides induced by volcanic activity. This work therefore represents a first step toward a more comprehensive PTHA for Stromboli Island.

In this study, by integrating two large databases of numerical tsunami simulations with a structured expert elicitation, we have produced a suite of probabilistic inundation maps and hazard curves that quantify not only the expected hazard but also its associated uncertainty. The simulation databases were developed using high-resolution 20m and 10m topobathymetries and two versions of an advanced non-hydrostatic numerical model. The uncertainty in landslide source parameters—such as volume, initial position, and frequency of occurrence—was quantified through an expert elicitation and propagated through the entire hazard assessment workflow. This ~~latter~~ produced a series of probabilistic hazard maps presented as a set of three maps that help in quickly visualising the uncertainty. The incorporation of uncertainty in maps and curves is already established when dealing both with volcanic (see e.g. Neri et al., 2015; Constantinescu et al., 2022; Tadini et al., 2025) and tsunami hazard (see e.g., Glimsdal et al., 2019; Løvholt et al., 2020; Tonini et al., 2021). Following these approaches of quantitative hazard assessment, our approach includes:

- a quantification of both epistemic and aleatoric uncertainty through a formalized expert elicitation (considering the Cooke's Classical Model);
- a modelling approach where a substantial ~~set of simulations~~simulation sets are developed in different databases (for sensitivity test with respect to DEM resolution and code version) and combined with the probabilities obtained from expert elicitation;
- a representation of uncertainty through different products (hazard maps, hazard curves and hazard profiles) that allow to carefully evaluate the hazard with respect to different locations.

4.1 Sensitivity of the results to the use of a different model version, DEM and landslide volume range

The combined use of the new, high-resolution 10 m DEM and the updated '2025 version' of the code (Database B) results in a systematically lower hazard estimate compared to the 20 m DEM and the '2021 code version' (Database A).

Regarding the use of different code versions, we can see a systematic effect: the new 2025 code version leads to a significant reduction in water depth, between 1 and 3 meters, over a vast portion of the village compared to the previous version for the 20m DEM, while it is more balanced (reduction and increase in water depth in different portions of the village) for the 10m DEM. This highlights a strong interaction between the model physics and the topographic details, where the updated code produces a less severe inundation when run on a high-resolution DEM. However, as already mentioned in the previous section, the effect of using different code versions is smaller than that of using different DEMs~~the effect of the use of different code versions is lower than the effect derived from the use of different DEMs~~, especially with respect to the inundated area. Although the comparison between simulations performed using the 10 m and 20 m DEMs highlights significant differences in inundation patterns, these differences should not be interpreted solely in terms of grid resolution. Rather, they reflect a combination of factors related to data accuracy, data preprocessing, and the characteristic spatial scales of the physical processes involved. For the bathymetric domain, the new topobathymetry can be considered more accurate. The bathymetric data are more recent and originate from surveys with a much higher native resolution, allowing for a more reliable representation of near-shore morphology and, consequently, a more accurate simulation of tsunami wave propagation in the marine environment.

For the subaerial domain, the interpretation is more complex. While the new topographic dataset is also more recent, it presents some intrinsic limitations. In particular, the DEM is not filtered for vegetation, and tall trees are therefore retained in the elevation model. As a consequence, these elements act as obstacles to tsunami propagation with dimensions comparable to the tree canopy, whereas the actual physical obstacle (the trunk) would have a much smaller impact. This effect is related to the lack of vegetation filtering in the source data rather than to the DEM resolution itself. In addition, the 10 m resolution represents an intermediate scale that is sufficient to partially resolve buildings, which may locally act as barriers to flow, but insufficient to properly represent narrow streets and alleys that characterize the built environment of Stromboli village. This combination may locally restrict flow propagation and result in inundation patterns that are influenced by partially resolved urban features. Conversely, the 20 m DEM introduces a stronger smoothing of small-scale features, reducing the influence of individual buildings and resulting in a more conservative representation of inundation extent over urban areas. For this reason, despite its coarser resolution, the 20 m DEM may provide a more conservative hazard assessment on land.

Overall, it is therefore difficult to identify a single optimal DEM for tsunami hazard modelling at Stromboli. The two datasets present complementary advantages and limitations: the higher-resolution DEM offers a more accurate representation of marine wave propagation, while the coarser DEM may yield more conservative and stable inundation estimates on land. Presenting results obtained with both datasets allows these sources of epistemic uncertainty to be explicitly explored and communicated. Similarly, the choice of the landslide volume range involves a trade-off between completeness and methodological assumptions. The analysis including larger volumes ($\geq 1 \times 10^6$ m^3, incorporating 40×10^6 m^3 scenarios) provides a more comprehensive and conservative assessment of the hazard intensity, as it includes (although with limitations) all the scales of TLs identified by the four volume ranges defined in the elicitation. However, this required an assumption to handle the unbounded nature of the largest volume class elicited ($>30 \times 10^6$ m^3), for which we assigned the entire probability to the 40×10^6 m^3 scenarios. While this approach captures the impact of high-consequence events, the choice of a single representative volume is an acknowledged simplification.

4.2 Hazard assessment in critical areas of Stromboli village

The primary and most critical finding of this work is the quantification of a high probability of tsunami inundation for the inhabited coastal areas of Stromboli over the next 50 years. The probabilistic maps show that significant inundation is not a remote possibility but relatively likely. In particular, the 95th percentile maps - representing a severe but plausible “1-in-20” outcome from the range of expert uncertainty - indicate that widespread inundation by at least 0.5 m of water is likely. The hazard curves for critical sites reinforce this conclusion, showing non-negligible probabilities of exceeding damaging water depths. These results provide a first quantitative basis for civil protection authorities and stakeholders to inform risk mitigation strategies, emergency planning, and public awareness campaigns.

The remarkable stability observed when water depth threshold increases from 0.1 m to 1.0 m strongly suggests that the maximum inland penetration of the tsunami is dominated by the local topography rather than the specific height of the incoming wave. For the majority of the tsunamigenic scenarios, the waves likely possess sufficient energy to travel across the flat coastal plain until they are stopped by an abrupt change in slope at the edge of the village. The final inundation limit is therefore primarily a function of the terrain morphology, which acts as a natural barrier.

This finding has a critical implication for hazard assessment at Stromboli: in the vulnerable coastal areas, there is not a gradual relationship between wave height and inundation extent. Instead, once a minimal inundation threshold is surpassed, the flow is likely to occupy the entire susceptible low-lying area. This means that even scenarios producing waves of apparently moderate height (e.g., just over 1 m at the coast) can lead to a widespread and significant inundation across the village waterfront. Consequently, the entire low-lying coastal plain should be considered exposed to inundation, regardless of the specific tsunami scenario.

~~With respect to site-specific analysis, ~~A comparison can also be made between the sites for which hazard curves were developed and the effects of the 2002 tsunami described by ~~some comparison could be done with respect to sites where we developed hazard curves and the effect of the 2002 tsunami described in ~~Bertagnini et al. (2003) and Tinti et al. (2006a). The site of “Spiaggia Lunga” (point 1 in Figure 1) is the area where the highest run-up of all the 2002 event was measured (10.9 m; Tinti et al., 2006a). Despite the large uncertainty expressed by the 5th-95th percentile range, our hazard estimates indicate a probability of equalling or exceeding 0.5 m in the next 50 years that is consistently > 70% as median probability (depending on the database/volume range chosen; see Figs. S9-S12 from Supporting Information). Similarly, the “Centrale ENEL” site (which was flooded during the 2002 tsunami; Tinti et al., 2006a) shows probabilities for the same threshold consistently > 60% as median probability (see Fig. 11), indicating a major hazard for this very sensitive site. The “Area di attesa Ficogrande” site (Figs. 1 and 12), as previously noted, is located outside the inundation area of the 2002 tsunami, over which the current Italian civil protection plan is based (Protezione Civile, 2015). For this site, we highlight the dual behaviour observed when considering maps obtained with the Databases A and B (Fig. 12). While for Database B the probability of inundation above the adopted threshold is zero, for Database A the median probability of equalling or exceeding 0.5 m over the next 50 years is~~While in fact for the 10 m database the probability of inundation is zero, Database A the probability of equalling or exceeding~~

~~0.5 m in the next 50 years is~~ > 5% or > 10% ~~as median probability~~, indicating a non-negligible hazard also for this site (taking also into account the capability of a tsunami wave of 0.5 to drag away an adult).

Figures 13 and 14 provide two complementary advantages. First, they offer a rapid overview of spatial trends in the hazard and their relationship with coastal morphology~~Figures 13 and 14 have a double advantage. From one side it could offer a quick view useful to identify trend in hazard assessment and link them to morphological aspects of the coastline~~. For example, in Figure 13 the decrease in probability values to the east of "Area di attesa Ficogrande" can be interpreted as a sheltering effect caused by the orientation of the coastline relative to the incoming waves from the northwest. Along the same line, the significant drop in probability occurring in the easternmost section ("Centrale ENEL" to "Molo Scari") indicates that this area becomes progressively more shielded from the main tsunami impact.

On the other hand, hazard profiles are also useful for evaluating the hazard along a contour associated with the maximum run-up of a known event~~hazard profiles are useful in case one would like to evaluate the hazard along a line describing the maximum runup of a known event~~ (i.e., the measured maximum run-up of the 2002 event; Tinti et al., 2006a). In our case, choosing the 15-m isoline is conservative with respect to the maximum run-up measured for the 2002 event (10.9 m) but helps in evaluating the hazard along critical limits, that in our case is beyond the safe zone area as defined by the current Italian civil protection plan.

4.3 Limits and future developments of the current approach

The approach and the results described in previous sections represent a first step toward a more quantitative tsunami hazard assessment for Stromboli village. The large uncertainty quantified in our results is indicative of the high sensitivity of the investigated area to even small variations in landslide volume and location, as well as in the probabilities assigned to different scenarios~~with respect to even small fluctuations in both the volume/location of landslide but also to the probabilities of different scenarios~~ in the next 50-year period.

To summarize some considerations from the previous sections, we wish to add that the maps/curves produced, when considered individually, may present certain limitations, specifically:

- Less accurate topobathymetry for maps/curves produced using 20 m simulations. On one hand, the source bathymetric data is less accurate; on the other, at a 20 m resolution, the smoothing of the topography produces a much more uniform inundation model, lacking visible effects of obstacles at the scale of individual buildings.
- At a 10 m resolution, the inundation maps clearly show the local effects of buildings or small natural elements on wave propagation. However, an even higher resolution is likely requisite for an accurate description of these effects, in order to model the impact of alleys and streets between individual buildings.
- Concentration of probability for the volume interval $V > 30 \times 10^6$ m^3 within a single scenario (40×10^6 m^3) for maps/curves produced with simulations at both 10 m and 20 m with volumes $\geq 1 \times 10^6$ m^3.
- Lateral source position. The lateral position of the initial mass at a given elevation is not explicitly propagated in the present PTHA. Esposti Ongaro et al. (2025) found that lateral displacements of the source within the Sciara del Fuoco

produced variations of about 10% in proximal waveforms, smaller than those associated with the dominant source parameters. Consistently, Trolese et al. (2026) identify source azimuth as a secondary control on maximum wave height on average, although its influence can be locally larger close to the source.

For future developments, higher-resolution DEMs, more accurate reconstruction of landslide volumes of past events, a broader sampling of lateral source positions, or updated estimates of landslide frequency could significantly modify both the spatial extent and intensity of the hazard. Future work could focus on incorporating these improvements to refine hazard estimates and reduce epistemic uncertainty.

5 Conclusions

This work provides the first probabilistic tsunami hazard assessment study for landslides induced by volcanic activity at Stromboli volcano along the Sciara del Fuoco. By integrating probabilities derived from expert elicitation and numerical modelling of different landslide scenarios (mainly different volumes and initial landslide positions), we produced inundation maps, hazard curves and hazard profiles, explicitly quantifying the large uncertainties inherent in the process (through the representation of maps/curves/profiles corresponding to 5th/50th/95th percentile values). These maps/curves were produced for the 50-year time horizon defined by the expert elicitation.~~taking into consideration the temporal framework of the next 50 years, as derived from the expert elicitation~~. We also explored the sensitivity of the results to: i) different DEM resolutions~~ of the DEMs~~ used for numerical modelling (10 m and 20 m), ii) different model version, and iii) different landslide volume range. ~~In this way, w~~We therefore offer a transparent basis for hazard assessment and mitigation planning. The sensitivity analysis indicates that the impact of the use of different DEMs is more important (when considering the extent of the inundated area) ~~with respect to~~than the use of different model versions and different landslide volume ranges.

Key products include hazard maps ~~(~~for four fixed water depth thresholds and ~~for~~ two fixed probability values~~)~~, hazard curves for six~~6~~ sensitive sites along the coast of Stromboli~~. In addition~~, and hazard profiles along the specific 15-m elevation isoline ~~are derived from the corresponding hazard maps to explore the hazard at specific elevations~~. Important findings of this work indicate that, from a qualitative point of view, the 95th percentile maps indicate that widespread inundation by at least 0.5 m of water is likely. More quantitatively, water depths of ≥ 0.5 m have a median probability of > 60 %, regardless of the DEM chosen or the landslide volume range considered, for the main critical infrastructure of Stromboli Island (i.e. the local power plant). In addition, for one of the island's most popular tourist beaches~~one of the most touristic beaches of the island~~ ("Spiaggia Lunga"), in the next 50 years the median probability of the same water depth threshold is similarly > 70 %. Inspection of hazard profiles along specific isolines~~,~~ indicates that for the 15-m elevation isoline there ~~is still~~remains a considerable ~~hazard~~ probability that this zone could be ~~impacted~~ affected by tsunami waves ≥ 0.5 m. These hazard products may support coastal planning at Stromboli for volcano-generated tsunamis, including evacuation mapping for responses to alerts issued by the local tsunami warning system (Ripepe and Lacanna, 2024; Schindelé et al., 2024; UNESCO/IOC, 2024).

To conclude, it is important to recognize that PTHA is an evolving process. These maps and curves represent the current state of knowledge and should be considered a living product, subject to future updates as new data become available, numerical models improve, and our understanding of the underlying physical processes is refined.

Code and data availability

The simulations used to create hazard maps and curves are freely available from the data repositories of ~~freely downloadable from~~ de' Michieli Vitturi (2026a-b) ~~databases~~. The simulations presented in this study were carried out using the Multilayer-HySEA code. The source code is publicly available at the GitHub repository: https://github.com/edanya-uma/Multilayer-HySEA.

Author contributions

MdMV.: conceptualization, resources, data curation, investigation, visualization, software, methodology, supervision, project administration, ~~methodology~~, writing – original draft, writing – review & editing, ~~project administration~~; AT: conceptualization, resources, data curation, investigation, visualization, software, methodology, writing – original draft, writing – review & editing; AB: conceptualization, resources, data curation, formal analysis, investigation, visualization, methodology, writing – review & editing; JFRG: resources, data curation, visualization, methodology, writing – review & editing; MC, TEO, AN, MT: conceptualization, resources, data curation, visualization, methodology, writing -review & editing; SL: methodology, writing – review & editing, project administration; JM, MJC, CE, SO, JMGV: software, writing – review & editing.

Competing interests

The authors declare no competing interests.

Financial support

This research has been supported by "Convenzione Attuativa per il potenziamento delle attività di servizio, Task 2.2" in the framework of "Accordo Quadro DPC-INGV 2022-2025".

Acknowledgements

The contribution and support of ideas of Eugenio Privitera and Mauro Coltelli (INGV coordinators of the DPC-INGV agreement) and of many colleagues participating in the project are acknowledged. In particular, we wish to thank Massimiliano Favalli, Alessandro Fornaciai, Mauro Coltelli, Danilo Cavallaro and Marina Bisson for providing the topo-bathymetric data used to perform the simulations. We also thank Laura Sandri, Finn Løvholt, Stephan Grilli, Anne LeFriant and Bill Fry for useful comments and suggestions provided within the "Convenzione Attuativa per il potenziamento delle attività di servizio, Task 2.2". The manuscript does not necessarily represent official views and policies of the Dipartimento della Protezione Civile.

References

Abadie, S., Aguirre-Ayerbe, I., Aniel-Quiroga, I., Babeyko, A., Baiguera, M., Basili, R., Belliazzi, S., Grezio, A., Johnson, K., Murphy, S., Paris, R., Rafliana, I., De Risi, R., Rossetto, T., Selva, J., Taroni, M., Del Zoppo, M., Armigliato, A., Bures, V., Cech, P., Cecioni, C., Christodoulides, P., Davies, G., Dias, F., Bayraktar, H. B., González, M., Gritsevich, M., Guillas, S., Harbitz, C. B., Kânoğlu, U., Macías, J., Papadopoulos, G. A., Polet, J., Romano, F., Salamon, A., Scala, A., Stepinac, M., Tappin, D. R., Thio, H. K., Tonini, R., Triantafyllou, I., Ulrich, T., Varini, E., Volpe, M., Vyhmeister, E., Behrens, J., Løvholt, F., Jalayer, F., Lorito, S., Salgado-Gálvez, M. A., and Sørensen, M.: Probabilistic tsunami hazard and risk analysis: A review of research gaps. Frontiers in Earth Science, 9, 628772, doi: 10.3389/feart.2021.628772, 2021.

Aspinall, W. P.: A route to more tractable expert advice. Nature 463, 294–295, doi: 10.1038/463294a, 2010.

Aspinall, W. P.: Structured elicitation of expert judgement for probabilistic hazard and risk assessment in volcanic eruptions. In: Mader HM, Coles SG, Connor CB, Connor LJ (eds) Statistics in Volcanology. Geological Society of London, 15-30, doi: 10.1144/IAVCEI001.2, 2006.

Aspinall, W. P., and Cooke, R.: Expert elicitation and judgement. In Risk and uncertainty assessment in natural hazards, Cambridge University Press, 234-274, 2013.

Barberi F., Rosi M., and Sodi A.: Volcanic Hazard Assessment at Stromboli Based on Review of Historical Data. *Acta Vulcanol.*, 3, 173–187, 1993.

Basili, R., Brizuela, B., Herrero, A., Iqbal, S., Lorito, S., Maesano, F.E., Murphy, S., Perfetti, P., Romano, F., Scala, A., Selva, J., Taroni, M., Thio, H.K., Tiberti, M.M., Tonini, R., Volpe, M., Glimsdal, S., Harbitz, C.B., Løvholt, F., Baptista, M.A., Carrilho, F., Matias, L.M., Omira, R., Babeyko, A., Hoechner, A., Gurbuz, M., Pekcan, O., Yalçıner, A., Canals, M., Lastras, G., Agalos, A., Papadopoulos, G., Triantafyllou, I., Benchekroun, S., Agrebi Jaouadi, H., Attafi, K., Ben Abdallah, S., Bouallegue, A., Hamdi, H., and Oueslati, F.: NEAM Tsunami Hazard Model 2018 (NEAMTHM18): online data of the Probabilistic Tsunami Hazard Model for the NEAM Region from the TSUMAPS-NEAM project. Istituto Nazionale di Geofisica e Vulcanologia (INGV), doi: 10.13127/tsunami/neamthm18, 2018.

Basili R., Brizuela B., Herrero A., Iqbal S., Lorito S., Maesano F.E., Murphy S., Perfetti P., Romano F., Scala A., Selva J., Taroni M., Thio H.K., Tiberti M.M., Tonini R., Volpe M., Glimsdal S., Harbitz C.B., Løvholt F., Baptista M.A., Carrilho F., Matias L.M., Omira R., Babeyko A., Hoechner A., Gurbuz M., Pekcan O., Yalçıner A., Canals M., Lastras G., Agalos A., Papadopoulos G., Triantafyllou I., Benchekroun S., Agrebi Jaouadi K., Ben Abdallah S., Bouallegue A., Hamdi H., Oueslati F., Amato A., Armigliato A., Behrens J., Davies G., Di Bucci D., Dolce M., Geist E., Gonzalez Vida J.M., González M., Macías Sánchez J., Meletti C., Ozer Sozdinler C., Pagani M., Parsons T., Polet J., Power W., Sørensen M.B, and Zaytsev A.: The making of the NEAM Tsunami Hazard Model 2018 (NEAMTHM18). *Front. Earth Sci*., doi: 10.3389/feart.2020.616594, 2021.

Behrens, J., Løvholt, F., Jalayer, F., Lorito, S., Salgado-Gálvez, M. A., Sørensen, M., Abadie, S., Aguirre-Ayerbe, I., Aniel-Quiroga, I., Babeyko, A., Baiguera, M., Basili, R., Belliazzi, S., Grezio, A., Johnson, K., Murphy, S., Paris, R., Rafliana, I., De Risi, R., Rossetto, T., Selva, J., Taroni, M., Del Zoppo, M., Armigliato, A., Bureš, V., Cech, P., Cecioni, C., Christodoulides, P., Davies, G., Dias, F., Başak Bayraktar, H., González, M., Gritsevich, M., Guillas, S., Harbitz, C. B., Kânoğlu, U., Macías, J., Papadopoulos, G. A., Polet, J., Romano, F., Salamon, A., Scala, A., Stepinac, M., Tappin, D. R., Kie Thio, H., Tonini, R., Triantafyllou, I., Ulrich, T., Varini, E., Volpe, M., ~~&~~ and Vyhmeister, E.: Probabilistic tsunami hazard and risk analysis: A review of research gaps. *Frontiers in Earth Science*, 9, 628772, doi: 10.3389/feart.2021.628772, 2021.

Bertagnini, A., Papale, P., and Santi, P.: Osservazioni e misure relative all'onda di maremoto del 30 dicembre 2002, effettuate lungo il paese di Stromboli dalla località Piscità al centro GNV eliporto PC. GNV Technical report, 4 pp., https://gnv.ingv.it/pubblicazioni/Stima%20H%20massima%20Tsunami%20dic%202002.pdf, 2003.

Bevilacqua, A.: Doubly stochastic models for volcanic hazard assessment at Campi Flegrei caldera, 227 pp., Birkhäuser/Springer, Pisa, doi: 10.1007/978-88-7642-577-6, 2016.

Bevilacqua, A., Isaia, R., Neri, A., Vitale, S., Aspinall, W. P., Bisson, M., Flandoli, F., Baxter, P. J., Bertagnini, A., Esposti Ongaro, T., Iannuzzi, E., Pistolesi, M., and Rosi, M.: Quantifying volcanic hazard at Campi Flegrei caldera (Italy) with uncertainty assessment: 1. Vent opening maps. Journal of Geophysical Research: Solid Earth 120(4), 2309–2329, doi: 10.1002/2014jb011775, 2015.

Bevilacqua, A., de' Michieli Vitturi, M., Tadini, A., Neri, A., Aspinall, W. P., and Sparks, R. S. J.: The Kolumbo Volcanic Field, Greece: expert elicitation findings supporting volcanic hazard and risk assessment. *Bull. Volcanol.*, 87, 41, doi:10.1007/s00445-025-01822-3, 2025.

Bisson, M., Gianardi, R., Civico, R., Madonia, P., Ricci, T., and Spinetti, C.: Stromboli DSM 2023. INGV Ufficio Dati, doi: 10.13127/stromboli/airborne-lidar-2023, 2025.

Bonilauri, E. M., Harris, A. J., Morin, J., Ripepe, M., Mangione, D., Lacanna, G., Ciolli, S., Cusolito, M., and Deguy, P.: Tsunami evacuation times and routes to safe zones: a GIS-based approach to tsunami evacuation planning on the island of Stromboli, Italy. *J. Appl. Volcanol.*, 10(1), 4, doi:10.1186/s13617-021-00104-9, 2021.

Brunetti, M. T., Guzzetti, F., and Rossi, M.: Probability distributions of landslide volumes. *Nonlinear Process. Geophys.*, 16(2), 179–188, doi:10.5194/npg-16-179-2009, 2009.

Cerminara, M., Esposti Ongaro, T., de' Michieli Vitturi, M., Tadini, A., Trolese, M., Fornaciai, A., Nannipieri, L., and Rodriguez Galvez, J. F.: Simulated scenarios of volcanic mass movements and associated tsunamis at Stromboli (Aeolian archipelago, Tyrrhenian Sea, Italy). version 1 [Data set]. Istituto Nazionale di Geofisica e Vulcanologia (INGV). Doi: 10.13127/stromboli/sciara_del_fuoco_tsunami, 2024.

Chiocci, F. L., and Ridente, D.: Regional-scale seafloor mapping and geohazard assessment. The experience from the Italian project MaGIC (Marine Geohazards along the Italian Coasts). Marine Geophysical Research 32(1–2), 13–23, doi: 10.1007/s11001-011-9120-6, 2011.

Colson, A. R., and Cooke, R. M.: Expert elicitation: using the classical model to validate experts' judgments. Review of Environmental Economics and Policy, doi: 10.1093/reep/rex022, 2018.

Constantinescu, R., González-Zuccolotto, K., Ferrés, D., Sieron, K., Siebe, C., Connor, C., Capra, L., and Tonini, R.: Probabilistic volcanic hazard assessment at an active but under-monitored volcano: Ceboruco, Mexico. Journal of Applied Volcanology, 11(1), 11, doi: 10.1186/s13617-022-00119-w, 2022.

Cooke, R. M.: Experts in uncertainty: opinion and subjective probability in science, 1991.

Cordrie, L., Selva, J., Bernardi, F., Tonini, R., Romano, F., Volpe, M., and Lorito, S.: Dynamic management of uncertainty in rapid tsunami forecasting. Communications Earth & Environment, 6(1), 637, doi: 10.1038/s43247-025-02586-6, 2025.

Dalrymple, R.A., Grilli, S.T., and Kirby, J.T.: Tsunamis and challenges for accurate modeling. Oceanography 19(1):142–151, doi: 10.5670/oceanog.2006.97, 2006

de' Michieli Vitturi, M., Bevilacqua, A., Tadini, A., and Neri, A.: ELICIPY 1.0: a Python online tool for expert elicitation. SoftwareX, 25, 101641, doi: 10.1016/j.softx.2024.101641, 2024.

de' Michieli Vitturi, M., Bevilacqua, A., Tadini, A., and Neri, A.: Version 2-ELICIPY: A Python online tool for expert elicitation. SoftwareX, 35, 102785, doi: 10.1016/j.softx.2026.102785, 2026.

de' Michieli Vitturi M., Tadini A., Bevilacqua A., Rodríguez Gàlvez J. F., Cerminara M., Esposti Ongaro T., Neri A., Trolese M., Macías J., Castro M. J., Escalante C., Ortega S., and González-Vida J. M.: Simulated scenarios of volcanic mass movements and associated tsunamis at Stromboli (Aeolian archipelago, Tyrrhenian sea, Italy) - version 2, simulations with 20-m resolution topo-bathymetry. [Dataset]. INGV Ufficio Dati, https://www.pi.ingv.it/banche-dati/scenarios-of-volcanic-mass-movements-associated-tsunamis-at-stromboli-20-m-topo-bathymetry/, 2026a.

de' Michieli Vitturi M., Tadini A., Bevilacqua A., Rodríguez Gàlvez J. F., Cerminara M., Esposti Ongaro T., Neri A., Trolese M., Macías J., Castro M. J., Escalante C., Ortega S., and González-Vida J. M.: Simulated scenarios of volcanic mass movements and associated tsunamis at Stromboli (Aeolian archipelago, Tyrrhenian sea, Italy) - version 2, simulations with 10-m resolution topo-bathymetry. [Dataset]. INGV Ufficio Dati, https://www.pi.ingv.it/banche-dati/scenarios-of-volcanic-mass-movements-and-associated-tsunamis-at-stromboli-10-m-topo-bathymetry/, 2026b.

Di Traglia, F., Calvari, S., D'Auria, L., Nolesini, T., Bonaccorso, A., Fornaciai, A., Esposito, A., Cristaldi, A., Favalli, M., and Casagli, N.: The 2014 Effusive Eruption at Stromboli: New Insights from In Situ and Remote-Sensing Measurements. Remote Sens. 10, 2035, doi: 10.3390/rs10122035, 2018.

Di Traglia, F., Fornaciai, A., Casalbore, D., Favalli, M., Manzella, I., Romagnoli, C., Chiocci, F. L., Cole, P., Nolesini, T., and Casagli, N.: Subaerial-submarine morphological changes at Stromboli volcano (Italy) induced by the 2019–2020 eruptive activity. Geomorphology, 400, 108093, doi: 10.1016/j.geomorph.2021.108093, 2022.

Escalante, C., de Luna, T. M., and Castro, M. J.: Non-hydrostatic pressure shallow flows: GPU implementation using finite volume and finite difference scheme. Applied Mathematics and Computation, 338, 631–659, doi: 10.1016/j.amc.2018.06.035, 2018.

Escalante, C., Fernández-Nieto, E. D., de Luna, T. M., and Castro, M. J.: An efficient two-layer non-hydrostatic approach for dispersive water waves. Journal of Scientific Computing, 79, 273–320, doi: 10.1007/s10915-018-0849-9, 2019.

Esposti Ongaro, T., de'Michieli Vitturi, M., Cerminara, M., Fornaciai, A., Nannipieri, L., Favalli, M., Calusi, B., Macías, J., Castro, M. J., Ortega, S., González-Vida, J. M., and Escalante, C.: Modeling tsunamis generated by submarine landslides at Stromboli Volcano (Aeolian Islands, Italy): A numerical benchmark study. Frontiers in Earth Science, 9, 628652, doi: 10.3389/feart.2021.628652, 2021.

Esposti Ongaro, T., Cerminara, M., de'Michieli Vitturi, M., Tadini, A., Trolese, M., Fornaciai, A., Nannipieri, L., Calusi, B., Macías, J., Castro, M. J., Escalante, C., Acosta, S. O., González-Vida, J. M., and Rodriguez Galvez, J. F.: Modeling and numerical simulation of volcanic mass movements and associated tsunamis at Stromboli (Aeolian archipelago, Tyrrhenian sea, Italy). Frontiers in Earth Science, 13, 1548961, doi: 10.3389/feart.2025.1548961, 2025.

Fernández-Nieto, E. D., Bouchut, F., Bresch, D., Castro Díaz, M. J., and Mangeney, A.: A new Savage–Hutter type model for submarine avalanches and generated tsunami. Journal of Computational Physics, 227, 7720–7754, doi: 10.1016/j.jcp.2008.04.039, 2008.

Fernández-Nieto, E. D., Garres-Díaz, J., Mangeney, A., and Narbona-Reina, G.: 2D granular flows with the μ(I) rheology and side walls friction: A well-balanced multilayer discretization. Journal of Computational Physics, 356, 192-219, doi: 10.1016/j.jcp.2017.11.038, 2018.

Fornaciai, A., Favalli, M., and Nannipieri, L.: Numerical simulation of the tsunamis generated by the Sciara del Fuoco landslides (Stromboli Island, Italy). Scientific reports, 9(1), 18542, doi: 10.1038/s41598-019-54949-7, 2019.

Fukutani, Y., Moriguchi, S., Terada, K., and Otake, Y.: Time-dependent probabilistic tsunami inundation assessment using mode decomposition to assess uncertainty for an earthquake scenario. Journal of Geophysical Research: Oceans, 126(7), e2021JC017250, doi: 10.1029/2021JC017250, 2021.

Gibbons, S. J., Lorito, S., Macías, J., Løvholt, F., Selva, J., Volpe, M,, Sánchez-Linares, C., Babeyko, A., Brizuela, B., Cirella, A., Castro, M. J., de la Asunción, M., Lanucara, P., Glimsdal, S., Lorenzino, M. C., Nazaria, M., Pizzimenti, L., Romano, F., Scala, A., Tonini, R., Manuel González-Vida, J., and Vöge, M.: Probabilistic Tsunami Hazard Analysis: High Performance Computing for Massive Scale Inundation Simulations. Front. Earth Sci., 8:591549, doi: 10.3389/feart.2020.591549, 2020.

Glimsdal, S., Løvholt, F., Harbitz, C. B., Romano, F., Lorito, S., Orefice, S., Brizuela, B., Selva, J., Hoechner, A., Volpe, M., Babeyko, A., Tonini, R., Wronna, M., and Omira, R.: A new approximate method for quantifying tsunami maximum inundation height probability. Pure and Applied Geophysics, 176(7), 3227-3246, doi: 10.1007/s00024-019-02091-w, 2019.

Grezio, A., Babeyko, A., Baptista, M. A., Behrens, J., Costa, A., Davies, G., Geist, E. L., Glimsdal, S., González, F. I., Griffin, J., Harbitz, C. B., LeVeque, R. J., Lorito, S., Løvholt, F., Omira, R., Mueller, C., Paris, R., Parsons, T., Polet, J., Power, W., Selva, J., Sørensen M. B., and Thio, H. K.: Probabilistic tsunami hazard analysis: multiple sources and global applications. Reviews of Geophysics, 55(4), 1158-1198, doi: 10.1002/2017RG000579, 2017.

Griffin, J., Latief, H., Kongko, W., Harig, S., Horspool, N., Hanung, R., Rojali, A., Maher, N, Fuchs, A., Hossen, J., Supryiati, U., Dewanto, S. E., Rakowsky, N., and Cummins, P.: An evaluation of onshore digital elevation models for modeling tsunami inundation zones. Front. Earth Sci. 3:32. doi: 10.3389/feart.2015.00032, 2015.

Horspool, N., Pranantyo, I., Griffin, J., Latief, H., Natawidjaja, D. H., Kongko, W., Cipta, A., Bustaman, B., Anugrah, S. D., and Thio, H. K.: A probabilistic tsunami hazard assessment for Indonesia. Natural Hazards and Earth System Sciences, 14(11), 3105-3122, doi: 10.5194/nhess-14-3105-2014, 2014.

Kaiser, G., Scheele, L., Kortenhaus, A., Løvholt, F., Römer, H., and Leschka, S.: The influence of land cover roughness on the results of high resolution tsunami inundation modeling. Nat. Hazards Earth Syst. Sci. 11, 2521–2540. doi: 10.5194/nhess-11-2521-2011, 2011.

Kurisu, A., Suga, H., Prochazka, Z., Suzuki, K., Oguri, K., and Inoue, T.: Potential technique for improving the survival of victims of tsunamis. PLoS one, 13(5), e0197498, doi: 10.1371/journal.pone.0197498, 2018.

Jaccard, P.: Étude comparative de la distribution florale dans une portion des Alpes et des Jura. Bull Soc Vaudoise Sci Nat, 37, 547-579, 1901.

Løvholt, F., Glimsdal, S., and Harbitz, C. B.: On the landslide tsunami uncertainty and hazard. Landslides, 17(10), 2301-2315, doi: 10.1007/s10346-020-01429-z, 2020.

Lorito, S., Selva, J., Basili, R., Romano, F., Tiberti, M. M., and Piatanesi, A.: Probabilistic hazard for seismically induced tsunamis: accuracy and feasibility of inundation maps. Geophysical Journal International, 200(1), 574-588, doi: 10.1093/gji/ggu408, 2015.

Lorito, S., Behrens, J., Løvholt, F., Rossetto, T., and Selva, J.: From tsunami science to hazard and risk assessment: Methods and models. Frontiers in Earth Science, 9, 764922, doi: 10.3389/feart.2021.764922, 2021.

Macías, J., Escalante, C., and Castro, M. J.: Multilayer-HySEA model validation for landslide generated tsunamis – Part 1: Rigid slides. Natural Hazards and Earth System Sciences, 21, 775–789, doi: 10.5194/nhess-21-775-2021, 2021a.

Macías J, Escalante C, and Castro MJ: Multilayer-HySEA model validation for landslide generated tsunamis – Part 2: Granular slides. Natural Hazards and Earth System Sciences, 21, 791–805, doi: 10.5194/nhess-21-791-2021, 2021b.

MASE: DTM LiDAR con risoluzione a terra 1 metro - Regione Sicilia, Geoportale Nazionale, Ministero dell'Ambiente e della Sicurezza Energetica, http://www.pcn.minambiente.it/, 2013.

Neri, A., Aspinall, W. P., Cioni, R., Bertagnini, A., Baxter, P. J., Zuccaro, G., Andronico, D., Barsotti, S., Cole, P.D., Esposti Ongaro, T., Hincks, T.K., Macedonio, G., Papale, P., Rosi, M., Santacroce, R., ~~&~~ and Woo, G.: Developing an event tree for probabilistic hazard and risk assessment at Vesuvius. *J. Volcanol. Geotherm. Res.*, 178(3), 397-415, doi: 10.1016/j.jvolgeores.2008.05.014, 2008.

Neri, A., Bevilacqua, A., Esposti Ongaro, T., Isaia, R., Aspinall, W. P., Bisson, M., Flandoli, F., Baxter, P. J., Bertagnini, A., Iannuzzi, E., Orsucci, S., Pistolesi, M., Rosi, M., and Vitale, S.: Quantifying volcanic hazard at Campi Flegrei caldera (Italy) with uncertainty assessment: 2. Pyroclastic density current invasion maps. Journal of Geophysical Research: Solid Earth, 120(4), 2330-2349, doi: 10.1002/2014JB011776, 2015.

Paris, R., Ulvrová, M., Selva, J., Brizuela, B., Costa, A., Grezio, A., Lorito, S., Tonini, R.: Probabilistic hazard analysis for tsunamis generated by subaqueous volcanic explosions in the Campi Flegrei caldera, Italy. Journal of Volcanology and Geothermal Research, 379, 106-116, doi: 10.1016/j.jvolgeores.2019.05.010, 2019.

Protezione Civile: https://rischi.protezionecivile.gov.it/en/volcanic/volcanoes-italy/stromboli/emergency-planning/, last access 15 March 2026, 2015.

Protezione Civile: https://www.protezionecivile.gov.it/en/normativa/decreto-legislativo-n-1-del-2-gennaio-2018--codice-della-protezione-civile/, last access 15 March 2026, 2018a.

Protezione Civile: https://rischi.protezionecivile.gov.it/static/0d78a388122669d46d9a7df0a09cc562/indicazioni-siam-senza-allegati.pdf, last access 15 March 2026, 2018b.

Quigley, J., Colson, A., Aspinall, W., and Cooke, R.M.: Elicitation in the Classical Model. In: Dias, L., Morton, A., Quigley, J. (eds) Elicitation. International Series in Operations Research & Management Science, vol 261. Springer, Cham, doi: 10.1007/978-3-319-65052-4_2, 2018.

Ramos, M., Aránguiz, R., and Bull, M. T.: Tsunami inundation limit based on probabilistic analysis of runup and inundation distance. Natural Hazards, 121(3), 2719-2745, doi: 10.1007/s11069-024-06916-3, 2025.

Ripepe, M., and Lacanna, G.: Volcano generated tsunami recorded in the near source. Nat. Commun., 15(1), 1802, doi:10.1038/s41467-024-45937-1, 2024.

Scala, A., Lorito, S., Escalante Sánchez, C., Romano, F., Festa, G., Abbate, A., Bayraktar, H. B., Castro, M. J., Macías, J., and Gonzalez-Vida, J. M.: Assessing the optimal tsunami inundation modeling strategy for large earthquakes in subduction zones. Journal of Geophysical Research: Oceans, 129(9), e2024JC020941, doi: 10.1029/2024JC020941, 2024.

Schindelé, F., Kong, L., Lane, E. M., Paris, R., Ripepe, M., Titov, V., and Bailey, R.: A review of tsunamis generated by volcanoes (TGV) source mechanism, modelling, monitoring and warning systems. Pure Appl. Geophys., 181(6), 1745–1792, doi:10.1007/s00024-024-03515-y, 2024.

Selva, J., Lorito, S., Volpe, M., Romano, F., Tonini, R., Perfetti, P., Bernardi, F., Taroni, M., Scala, A., Babeyko, A., Løvholt, F., Gibbons, S. J., Macías, J., Castro, M. J., González-Vida, J. M., Sánchez-Linares, C., Bayraktar, H. B., Basili, R., Maesano, F. E., Tiberti, M. M., Mele, F., Piatanesi, A., and Amato, A.: Probabilistic tsunami forecasting for early warning. Nature communications, 12(1), 5677, doi: 10.1038/s41467-021-25815-w, 2021.

Song, J., and Goda, K.: Influence of elevation data resolution on tsunami loss estimation and insurance rate-making. Frontiers in Earth Science, 7, 246, doi: 10.3389/feart.2019.00246, 2019.

Tadini, A., Bevilacqua, A., Neri, A., Cioni, R., Aspinall, W. P., Bisson, M., Isaia, R., Mazzarini, F., Valentine, G. A., Vitale, S., Baxter, P. J., Bertagnini, A., Cerminara, M., de Michieli Vitturi, M., di Roberto, A., Engwell, S., Esposti Ongaro, T., Flandoli, F., and Pistolesi, M.: Assessing future vent opening locations at the Somma-Vesuvio volcanic complex: 2. Probability Maps of the caldera for a future Plinian/sub-Plinian Event with uncertainty quantification. *Journal of Geophysical Research: Solid Earth* 122(6), 4357–4376, doi: 10.1002/2016jb013860, 2017.

Tadini, A., Harris, A., Morin, J., Bevilacqua, A., Peltier, A., Aspinall, W., Ciolli, S., Bachèlery, P., Bernard, B., Biren, J., Brum da Silveira, A., Cayol, V., Chevrel, O., Coppola, D., Dietterich, H., Donovan, A., Dorado, O., Drenne, S., Dupéré, O., Gurioli, L., Kolzenburg, S., Komorowski, J.-C., Labazuy, P., Mangione, D., Mannini, S., Martel-Asselin, F., Médard, E., Pailot-Bonnétat, S., Rafflin, V., Ramsey, M., Richter, N., Vallejo, S., Villeneuve, N., Zafrilla, S.: Structured elicitation of expert judgement in real-time eruption scenarios: an exercise for Piton de la Fournaise volcano, La Réunion island. *Volcanica*, 5(1), 105–131, doi: 10.30909/vol.05.01.105131, 2022.

Tadini, A., Bevilacqua, A., de' Michieli Vitturi, M., Bonilauri, E., Harris, A., Cerminara, M., Esposti Ongaro, T., Neri, A., Paris, R., Pistolesi, M., Trolese, M., Rodriguez Gàlvez, J. F., Andronico, D., Bertagnini, A., Calvari, S., Casalbore, D., Cassidy, M., Civico, R., Del Bello, E., Di Roberto, A., Fornaciai, A., Grezio, A., Gurioli, L., Harbitz, C. B., Lacanna, G., Løvholt, F., Marani, M., Pompilio, M., Rosi, M., Sandri, L., Urgeles, R., Voloschina, M.: Probabilistic tsunami hazard assessment at Stromboli volcano: 1. Review of historical sources and expert elicitation findings~~.~~, EGUsphere [preprint], doi: 10.5194/egusphere-2026-1310, 2026~~Nat. Hazards Earth Syst. Sci., submitted~~.

Tadini, A., Pardini, F., Bevilacqua, A., Bernard, B., Samaniego, P., de' Michieli Vitturi, M., Aravena, A., Hidalgo, S., Roche, O., Azzaoui, N., Neri, A., and Aguilar, J.: Probabilistic tephra fallout hazard maps for Sangay volcano, Ecuador. Bulletin of Volcanology, 87(2), 10, doi: 10.1007/s00445-025-01794-4, 2025.

Tinti, S., Bortolucci, E., ~~&~~ and Romagnoli, C.: Computer simulations of tsunamis due to sector collapse at Stromboli, Italy. *J. Volcanol. Geoth. Res.*, 96(1-2), 103-128, doi: 10.1016/S0377-0273(99)00138-9, 2000.

Tinti, S., Armigliato, A., Manucci, A., Pagnoni, G., ~~&~~ and Zaniboni, F.: Landslides and tsunamis of 30th December 2002 at Stromboli, Italy: numerical simulations. *Bollettino di Geofisica Teorica ed Applicata*, 46(2–3), 153-168, 2005.

Tinti, S., Maramai, A., Armigliato, A., Graziani, L., Manucci, A., Pagnoni, G., and Zaniboni, F.: Observations of physical effects from tsunamis of December 30, 2002 at Stromboli volcano, southern Italy. *Bull. Volcanol.*, 68, 450–461, doi:10.1007/s00445-005-0021-x, 2006a.

Tinti, S., Pagnoni, G., and Zaniboni, F.: The landslides and tsunamis of the 30th of December 2002 in Stromboli analysed through numerical simulations. *Bull. Volcanol.*, 68, 462-479, doi: 10.1007/s00445-005-0022-9, 2006b.

Trolese, M., Cerminara, M., Esposti Ongaro, T., de' Michieli Vitturi, M., and Tadini, A. (2026). Sensitivity analysis and scaling of tsunamis generated by granular flows at Stromboli volcano: A numerical modeling approach. EGUsphere preprint, https://doi.org/10.5194/egusphere-2026-1757, ~~(under review)~~2026.

Tonini, R., Di Manna, P., Lorito, S., Selva, J., Volpe, M., Romano, F., Basili, R., Brizuela, B., Castro, M. J., de la Asunción, M., Di Bucci, D., Dolce, M., Garcia, A., Gibbons, S. J., Glimsdal, S., González-Vida, J. M., Løvholt, F., Macías, J., Piatanesi, A., Pizzimenti, L., Sánchez-Linares, C., and Vittori, E.: Testing Tsunami Inundation Maps for Evacuation Planning in Italy. Front. Earth Sci. 9:628061, doi: 10.3389/feart.2021.628061, 2021.

UNESCO/IOC: Monitoring and Warning for Tsunamis Generated by Volcanoes, Paris, UNESCO, IOC Technical Series No.183, 2024.

Volpe, M., Lorito, S., Selva, J., Tonini, R., Romano, F., and Brizuela, B.: From regional to local SPTHA: efficient computation of probabilistic tsunami inundation maps addressing near-field sources. *Natural Hazards and Earth System Sciences*, 19(3), 455-469, doi: 10.5194/nhess-19-455-2019, 2019.

Woessner, J., and Farahani, R. J.: Tsunami inundation hazard across Japan. International journal of disaster risk reduction, 49, 101654, doi: 10.1016/j.ijdrr.2020.101654, 2020.

Contents of this file

Text S1

Table S1

Figures S1-S12

Introduction

This supporting information contains:

- an extended description of the approaches used, respectively, to integrate simulations with expert elicitation outcomes and to obtain probabilistic hazard maps and curves (Text S1);
- a table listing all the target questions from the elicitation described in Tadini et al. (2026);
- the maps for fixed water depth for thresholds 0.1, 0.2 and 1 m for the Databases A and B and for volumes 1-30 × 10^6 m^3 and ≥ 1 × 10^6 m^3 (Figures S1-S6);
- the maps for fixed probability 2% for the Databases A and B and for volumes 1-30 × 10^6 m^3 and ≥ 1 × 10^6 m^3 (Figures S7-S8);
- the hazard curves for the 6 sites listed in Figure 1 from the main manuscript for the Databases A and B and for volumes 1-30 × 10^6 m^3 and ≥ 1 × 10^6 m^3 (Figures S9-S12).

Text S1

Integration of simulations with expert elicitation outcomes

To derive the hazard maps, we used the outputs of the CM method (see Section 2.1 of the main manuscript) and adopted the following procedure to derive probabilities for each specific volume/position interval. The ELICIPY tool (de' Michieli Vitturi et al., 2024; 2026), used for the elicitation described in Tadini et al. (~~submitted~~2026), generates a set of 10,000 probability values for each target question, representing the aggregated expert judgment. For this study, we thus obtained a set of 10,000 values for each of the target questions TQ16–TQ35. These questions are structured in a logic tree (see Figure TS1). Level 1 questions (TQ16–TQ19) concern the marginal probabilities of a landslide's center of mass falling into one of four elevation ranges. Level 2 questions (TQ20–TQ35) provide the conditional probabilities for four different volume classes (V1-V4), given a specific elevation range. To derive the absolute probabilities for each mutually exclusive volume/position interval, we performed the following calculation for each of the 10,000 sampling steps: the sampled probability value from a level-2 question (e.g., TQ20, the probability of a volume in class V1, given a deep submarine position) was multiplied by the corresponding sampled value from the relevant level-1 question (TQ16, the probability of a deep submarine position).

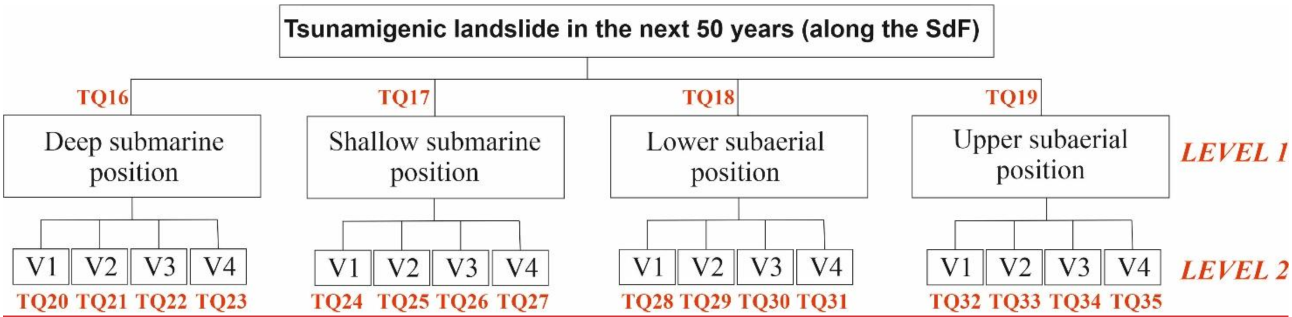

Figure TS1. Logic tree for target questions TQ16-TQ35. The four volume classes in Level 2 (V1-V4) are as follows: V1 – 1-5 x 10^6 m^3; V2 - 5-14 x 10^6 m^3; V3 – 14-30 x 10^6 m^3; V4 - >30 x 10^6 m^3.

This calculation was performed for both of our analysis approaches. For the 1-30 × 10^6 m^3 case, this process considered the 3 bounded volume classes, yielding a matrix of 10,000 rows and 12 columns (4 position ranges × 3 volume classes). For the ≥ 1 × 10^6 m^3 case, which includes the V4 volume class, the same procedure was applied to all 4 volume classes, resulting in a matrix of 10,000 rows and 16 columns (4 position ranges × 4 volume classes). In both cases, each row of the resulting matrix represents a complete, internally consistent set of probabilities for the respective intervals. The values in each row were then normalized to sum to 1 to account for any minor inconsistencies arising from the sampling process. The final output consists of these two matrices of absolute probabilities (10,000x12 and 10,000x16), which are then used to assign probabilities to the simulated scenarios.

As stated above, the main challenge in assigning these probabilities lies in bridging the gap between the elicited interval-based probabilities and the discrete nature of the simulation database. To address this, we developed a sampling procedure to apportion the probabilities from the two matrices (10,000x12 and 10,000x16 matrices) across the relevant discrete simulations. This procedure is based on the key assumption that the probability for an elicitation interval is uniformly distributed within its parameter space. The procedure is executed independently for each of the 10,000 probability sets (i.e., for each row of the matrices) and consists of the following steps:

1. Generate Random Scenarios within each Interval. For each probability interval (12 for the 1-30 × 10^6 m^3 case; 16 for the ≥ 1 × 10^6 m^3 case), we generate 20 random scenarios by sampling uniformly from its defined volume and elevation ranges. The density contrast for each of these randomly generated scenarios is also selected from a uniform distribution between 0.5 and 0.6. This process creates a total of 240 (for the 1-30 × 10^6 m^3 case) or 320 (for the ≥ 1 × 10^6 m^3 case) hypothetical, intermediate scenarios.
2. Map to Closest Simulated Scenarios. Each of these hypothetical scenarios is then mapped to the closest available simulation in the corresponding database subset (Figure 3 from the main document visually illustrates this mapping process for the volume range 1-30 × 10^6 m^3). This step identifies a set of 240 (or 320) - not necessarily distinct— simulations that are considered representative of the continuous probability distributions within the intervals.
3. Partition and Aggregate Probabilities. The probability of each interval is divided equally among its 20 corresponding representative simulations. The final probability for each discrete simulation is then calculated as the sum of all the probability portions it has received from the various intervals. Simulations that are never selected as the "closest" receive a final probability of zero for that sampling step.

This approach, by sampling each interval multiple times, effectively smooths the probability distribution across the discrete simulation set, providing a more robust representation of uncertainty than assigning an entire interval's probability to a single scenario.

The exceedance probabilities derived so far are conditional on the occurrence of a single tsunamigenic landslide within the Sciara del Fuoco. To convert these into absolute probabilities over a 50-year time horizon, we account for the expected frequency of events by incorporating the 10,000 sampled values from elicitation questions TQ3 (number of events in 50 years, N_{50}) and TQ4 (percentage within the Sciara del Fuoco - SdF, P_{SdF}). For each of the 10,000 sampling steps, we calculate a 50-year exceedance probability at every pixel. Since the expected number of events ($n = N_{50} \times P_{SdF}$) is a real number, we discretize its effect by considering the two closest integers, N_{low} and N_{up}. The conditional exceedance probability of a single event (p) is first used to compute the probability of at least one exceedance assuming N_{low} events and N_{up} events [$P(k) = 1 - (1 - p)^k$]. The final 50-year exceedance probability is then calculated as a weighted average of these two outcomes, where the weights are determined by the proximity of the sampled real number n to its integer neighbors. This entire procedure is repeated for all 10,000 sampling realizations, yielding a full distribution of 10,000 values for the 50-year exceedance probability at each pixel. This distribution fully captures the propagated uncertainty from both the source parameters and the event frequency. The final probabilistic maps were produced for water depth exceedance thresholds of 0.1, 0.2, 0.5, and 1 m. For each threshold, we present three maps corresponding to the 5th, Median, and 95th percentiles of the 10,000 fifty-year exceedance probability values calculated for each pixel.

The final output of this procedure consists of two distinct sets of probability vectors. For the 1-30 × 10^6 m^3 analysis, we obtained a set of 10,000 vectors, each containing 286 probability values corresponding to the simulations with volumes up to 30 × 10^6 m^3. For the ≥ 1 × 10^6 m^3 analysis, which includes the 40 × 10^6 m^3 scenarios, we obtain a separate set of 10,000 vectors, each containing 308 probability values. In both cases, each vector represents a complete probability distribution across the relevant set of discrete scenarios and serves as the foundational input for deriving the probabilistic inundation maps and hazard curves.

To generate the probabilistic maps for a fixed water depth threshold, we follow a procedure in line with standard Probabilistic Tsunami Hazard Assessment (PTHA) methodologies (e.g., Grezio et al., 2017; Selva et al., 2021). The process consists of the following steps:

- Set a Threshold and Binarize Maps. A specific water depth threshold is chosen (e.g., 0.5 m). Each of the 286/308 deterministic inundation maps is then converted into a binary map, where a pixel has a value of 1 if its water depth exceeds the threshold, and 0 otherwise.
- Calculate Exceedance Probability for a Single Realization. For each row of the probability matrix (representing one complete "realization" of the source uncertainty), we calculate a corresponding map of exceedance probabilities. For a given pixel, this is done by summing the products of the binary map values (0 or 1) and their corresponding probabilities from that row. The result for each pixel is the total probability of exceeding the threshold for that single realization.
- Generate the Full Distribution of Exceedance Probabilities. This process is repeated for all 10,000 rows of the matrix. Consequently, for every pixel in the domain, we obtain a distribution of 10,000 exceedance probability values. This distribution fully captures the uncertainty in the exceedance probability, as derived from the expert elicitation.

From this distribution of 10,000 values at each pixel, we can then compute summary statistics, such as the 5^{th}, 50^{th} (median), and 95^{th} percentiles. These percentile values are finally used to create the probabilistic inundation maps for the chosen threshold.

Development of Probabilistic hazard maps and curves

The process to obtain probabilistic hazard maps for a given water depth threshold consists of the following steps:

- set a threshold (e.g., 0.5 m) and binarize each of the 286/308 maps (pixel value 1 if its water depth exceeds the threshold, and 0 otherwise);
- calculate exceedance probability for a given pixel by summing the products of the binary map values (0 or 1) and their corresponding probabilities from that row;
- generate the full distribution of exceedance probabilities, obtaining a distribution of 10,000 exceedance probability values. From this distribution of 10,000 values at each pixel, we can then compute summary statistics, such as the 5th, 50th (median), and 95th percentiles. These percentile values are finally used to create the probabilistic inundation maps for the chosen threshold.

The final probabilistic maps were produced for water depth exceedance thresholds of 0.1, 0.2, 0.5, and 1 m. For each threshold, we present three maps corresponding to the 5^{th}, Median, and 95^{th} percentiles of the 10,000 fifty-year exceedance probability values calculated for each pixel.

The second category of hazard maps visualizes the water depth corresponding to a given exceedance probability. These maps represent the uncertainty in the inundation intensity for a specific likelihood level, providing a complementary perspective to the probability exceedance maps. The generation of these maps is performed for every pixel of the domain. For each of the 10,000 sampling realizations (i.e., each row of the probability matrix), we first construct a discrete cumulative probability distribution of water depth by summing the probabilities of the sorted simulation outcomes at a given pixel. From this distribution, we then identify the water depth value that corresponds to the desired exceedance probability (e.g., 10%). Repeating this process for all 10,000 realizations yields a distribution of 10,000 water depth values for each pixel. Each value in this distribution represents a plausible inundation depth for the chosen exceedance probability, reflecting the uncertainty propagated from the expert elicitation. From this distribution of water depths, we then compute summary statistics, such as the 5^{th}, 50^{th} (median), and 95^{th} percentiles. The final maps display these percentile values, thus illustrating the range of likely water depths for a given probability of exceedance. In this paper, we present maps for an exceedance probability of 10% and show the results for the 5th, Median, and 95th percentiles.

To better characterize the hazard for specific sites of interest, we derive hazard curves. These curves describe the probability of exceeding a range of water depth values at a given location and are a standard tool in probabilistic tsunami hazard assessment (e.g., Volpe et al., 2019). The procedure to obtain them is applied independently to both the 1-30 × 10^6 m3 and the ≥1 × 10^6 m^3 analysis cases and is as follows.

First, for each simulation in the relevant database subset (286 or 308 simulations, respectively), we extract the exact water depth at the coordinates of each point of interest. Since these points do not typically coincide with the grid nodes of the simulation, we use bilinear interpolation from the deterministic inundation maps. This step yields, for each site, an array of water depth values, one per simulation.

Next, we define a dense array of water depth thresholds, logarithmically spaced from 0.01 m to 20 m. For each of the 10,000 sampling realizations (i.e., each row of the corresponding 10,000x286 or 10,000x308 probability matrix), we compute a full hazard curve. This is done by calculating the probability of exceeding each threshold. For a given threshold, this probability is the sum of the probabilities (from the specific row of the matrix) of all simulations whose interpolated water depth at that site exceeds the threshold.

By repeating this calculation for every threshold, we obtain 10,000 distinct hazard curves for each site of interest. This ensemble of curves represents the full uncertainty in the hazard, as propagated from the expert elicitation. From this distribution of 10,000 curves, we compute the final hazard curves by taking the Median, 5th, and 95th percentiles of the exceedance probabilities at each water depth threshold.

Finally, these single-event hazard curves are converted to represent the hazard over a 50-year time horizon. This is achieved using the same procedure described for the inundation maps, which accounts for the sampled number of events in 50 years to calculate the final 50-year exceedance probabilities.

Table S1. Target questions from the elicitation of Tadini et al. (2026). Questions used in the present work are highlighted in italic and red.

Part	**Question ID**	**Text**
I	TQ1	Considering the known/documented past TLs with a volume greater than 1 × 10^6 m^3 which occurred at Stromboli from VIII century CE to the present and given possible under-reporting, how many TLs may have actually occurred from VIII century CE to 1878? (ca. 1200 years)
	TQ2	Considering the known/documented past TLs with a volume greater than 1 × 10^6 m^3 which occurred at Stromboli from VIII century CE to the present and given possible under-reporting, how many TLs may have actually occurred from 1879 to the present? (ca. 140 years)
	TQ3	*Considering TLs with a volume greater than 1 × 10^6 m^3 and given the current state of Stromboli volcano, how many TLs do you expect in the next 50 years?*
II	*TQ4*	*By considering the possible tsunamigenic landslides with a volume greater than 1x10^6 m^3 that could occur within the next 50 years, what percentage of them will have its center of mass inside the Sciara del Fuoco?*
	TQ5	By considering the possible tsunamigenic landslides with a volume greater than 1x10^6 m^3 that could occur within the next 50 years, what percentage of them will have its center of mass outside the Sciara del Fuoco?
	TQ6	By considering the possible tsunamigenic landslides with a volume greater than 1x10^6 m^3 that could occur inside the Sciara del Fuoco within the next 50 years what percentage of them will have a volcanic trigger?
	TQ7	By considering the possible tsunamigenic landslides with a volume greater than 1x10^6 m^3 that could occur inside the Sciara del Fuoco within the next 50 years what percentage of them will have a non-volcanic trigger?
	TQ8	By considering the possible tsunamigenic landslides with a volume greater than 1x10^6 m^3 that could occur inside the Sciara del Fuoco within the next 50 years with a volcanic trigger what percentage of them will have an endogenous trigger (i.e. dike intrusion or inflation of the shallow magma chamber)?
	TQ9	By considering the possible tsunamigenic landslides with a volume greater than 1x10^6 m^3 that could occur inside the Sciara del Fuoco within the next 50 years with a volcanic trigger what percentage of them will have an exogenous trigger? (i.e. rapid accumulation of lava and of tephra, primary PDCs)
	TQ10	By considering the possible tsunamigenic landslides with a volume greater than 1x10^6 m^3 that could occur inside the Sciara del Fuoco within the next 50 years with a non-volcanic trigger what percentage of them will be triggered by a regional earthquake?
	TQ11	By considering the possible tsunamigenic landslides with a volume greater than 1x10^6 m^3 that could occur inside the Sciara del Fuoco within the next 50 years with a non-volcanic trigger what percentage of them will be triggered by a meteorological/climatic/marine event?
	TQ12	By considering the possible tsunamigenic landslides with a volume greater than 1x10^6 m^3 that could occur inside the Sciara del Fuoco within the next 50 years with a volcanic exogenous trigger, what percentage of them will be triggered by with lava accumulation?
	TQ13	By considering the possible tsunamigenic landslides with a volume greater than 1x10^6 m^3 that could occur inside the Sciara del Fuoco within the next 50 years with a volcanic exogenous trigger, what percentage of them will be triggered by tephra accumulation during ordinary activity?
	TQ14	By considering the possible tsunamigenic landslides with a volume greater than 1x10^6 m^3 that could occur inside the Sciara del Fuoco within the next 50 years with a volcanic exogenous trigger, what percentage of them will be triggered by tephra accumulation during a paroxysm?

	TQ15	By considering the possible tsunamigenic landslides with a volume greater than 1x10⁶ m³ that could occur inside the Sciara del Fuoco within the next 50 years with a volcanic exogenous trigger, what percentage of them will be triggered by column collapse during a paroxysm?
III	*TQ16*	*By considering the possible tsunamigenic landslides with a volume greater than $1x10^6$ m^3 that could occur inside the Sciara del Fuoco within the next 50 years what percentage of them will be a deep-submarine landslide (center of mass between 700 and 300 m BSL)?*
	TQ17	*By considering the possible tsunamigenic landslides with a volume greater than $1x10^6$ m^3 that could occur inside the Sciara del Fuoco within the next 50 years what percentage of them will be a shallow-submarine landslide (center of mass between 300 m BSL and sea level)?*
	TQ18	*By considering the possible tsunamigenic landslides with a volume greater than $1x10^6$ m^3 that could occur inside the Sciara del Fuoco within the next 50 years what percentage of them will be a lower-subaerial landslide (center of mass between sea level and 300 m ASL)?*
	TQ19	*By considering the possible tsunamigenic landslides with a volume greater than $1x10^6$ m^3 that could occur inside the Sciara del Fuoco within the next 50 years what percentage of them will be a lower-subaerial landslide (center of mass between 300 and 700 m ASL)?*
	TQ20	*By considering the possible deep submarine tsunamigenic landslides with a volume greater than $1x10^6$ m^3 that could occur inside the Sciara del Fuoco in the next 50 years (center of mass between 700 and 300 m BSL) what percentage (%) of them will involve a volume between $1x10^6$ m^3 and $5x10^6$ m^3?*
	TQ21	*By considering the possible deep submarine tsunamigenic landslides with a volume greater than $1x10^6$ m^3 that could occur inside the Sciara del Fuoco in the next 50 years (center of mass between 700 and 300 m BSL) what percentage (%) of them will involve a volume between $5x10^6$ m^3 and $14x10^6$ m^3?*
	TQ22	*By considering the possible deep submarine tsunamigenic landslides with a volume greater than $1x10^6$ m^3 that could occur inside the Sciara del Fuoco in the next 50 years (center of mass between 700 and 300 m BSL) what percentage (%) of them will involve a volume between $14x10^6$ m^3 and $30x10^6$ m^3?*
	TQ23	*By considering the possible deep submarine tsunamigenic landslides with a volume greater than $1x10^6$ m^3 that could occur inside the Sciara del Fuoco in the next 50 years (center of mass between 700 and 300 m BSL) what percentage (%) of them will involve a volume above $30x10^6$ m^3?*
	TQ24	*By considering the possible shallow submarine tsunamigenic landslides with a volume greater than $1x10^6$ m^3 that could occur inside the Sciara del Fuoco in the next 50 years (center of mass between 300 m BSL and sea level) what percentage (%) of them will involve a volume between $1x10^6$ m^3 and $5x10^6$ m^3?*
	TQ25	*By considering the possible shallow submarine tsunamigenic landslides with a volume greater than $1x10^6$ m^3 that could occur inside the Sciara del Fuoco in the next 50 years (center of mass between 300 m BSL and sea level) what percentage (%) of them will involve a volume between $5x10^6$ m^3 and $14x10^6$ m^3?*
	TQ26	*By considering the possible shallow submarine tsunamigenic landslides with a volume greater than $1x10^6$ m^3 that could occur inside the Sciara del Fuoco in the next 50 years (center of mass between 300 m BSL and sea level) what percentage (%) of them will involve a volume between $14x10^6$ m^3 and $30x10^6$ m^3?*
	TQ27	*By considering the possible shallow submarine tsunamigenic landslides with a volume greater than $1x10^6$ m^3 that could occur inside the Sciara del Fuoco in the next 50 years (center of mass between 300 m BSL and sea level) what percentage (%) of them will involve a volume above $30x10^6$ m^3?*
	TQ28	*By considering the possible lower subaerial tsunamigenic landslides with a volume greater than $1x10^6$ m^3 that could occur inside the Sciara del Fuoco in the next 50 years (center of mass between*

		sea level and 300 m ASL) what percentage (%) of them will involve a volume between $1x10^6$ m^3 and $5x10^6$ m^3?
	TQ29	By considering the possible lower subaerial tsunamigenic landslides with a volume greater than $1x10^6$ m^3 that could occur inside the Sciara del Fuoco in the next 50 years (center of mass between sea level and 300 m ASL) what percentage (%) of them will involve a volume between $5x10^6$ m^3 and $14x10^6$ m^3?
	TQ30	By considering the possible lower subaerial tsunamigenic landslides with a volume greater than $1x10^6$ m^3 that could occur inside the Sciara del Fuoco in the next 50 years (center of mass between sea level and 300 m ASL) what percentage (%) of them will involve a volume between $14x10^6$ m^3 and $30x10^6$ m^3?
	TQ31	By considering the possible lower subaerial tsunamigenic landslides with a volume greater than $1x10^6$ m^3 that could occur inside the Sciara del Fuoco in the next 50 years (center of mass between sea level and 300 m ASL) what percentage (%) of them will involve a volume above $30x10^6$ m^3?
	TQ32	By considering the possible upper subaerial tsunamigenic landslides with a volume greater than $1x10^6$ m^3 that could occur inside the Sciara del Fuoco in the next 50 years (center of mass between 300 m ASL and 700 m ASL) what percentage (%) of them will involve a volume between $1x10^6$ m^3 and $5x10^6$ m^3?
	TQ33	By considering the possible upper subaerial tsunamigenic landslides with a volume greater than $1x10^6$ m^3 that could occur inside the Sciara del Fuoco in the next 50 years (center of mass between 300 m ASL and 700 m ASL) what percentage (%) of them will involve a volume between $1x10^6$ m^3 and $5x10^6$ m^3?
	TQ34	By considering the possible upper subaerial tsunamigenic landslides with a volume greater than $1x10^6$ m^3 that could occur inside the Sciara del Fuoco in the next 50 years (center of mass between 300 m ASL and 700 m ASL) what percentage (%) of them will involve a volume between $1x10^6$ m^3 and $5x10^6$ m^3?
	TQ35	By considering the possible upper subaerial tsunamigenic landslides with a volume greater than $1x10^6$ m^3 that could occur inside the Sciara del Fuoco in the next 50 years (center of mass between 300 m ASL and 700 m ASL) what percentage (%) of them will involve a volume above $30x10^6$ m^3?

Figure S1. Probabilistic maps for exceeding a water depth of 0.1 m over a 50-year horizon for the Database B. (a) Volume range 1-30 × 10^6 m^3; (b) volume range ≥ 1 × 10^6 m^3.

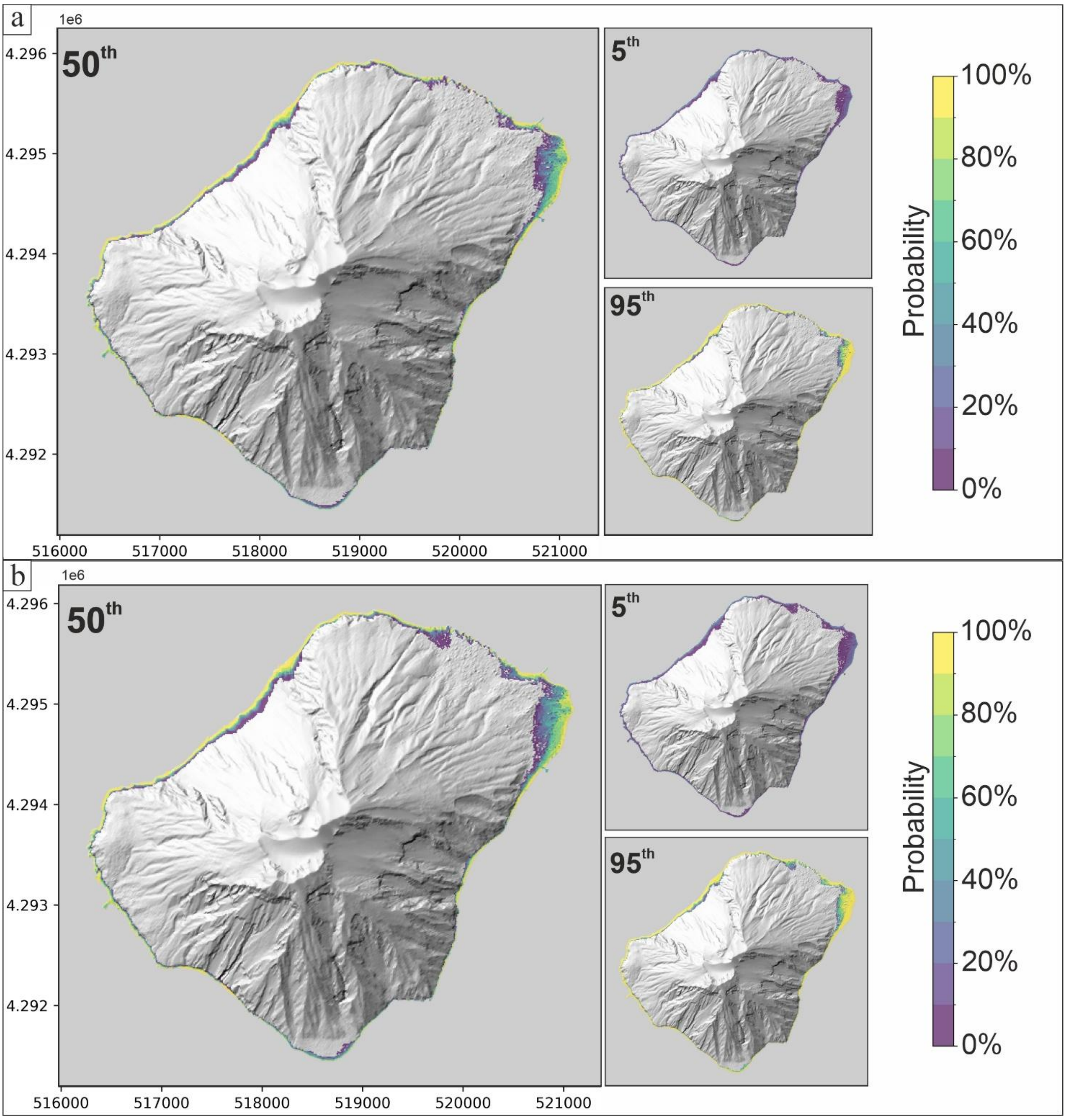

Figure S2. Probabilistic maps for exceeding a water depth of 0.1 m over a 50-year horizon for the Database A. (a) Volume range 1-30 × 10^6 m^3; (b) volume range ≥ 1 × 10^6 m^3.

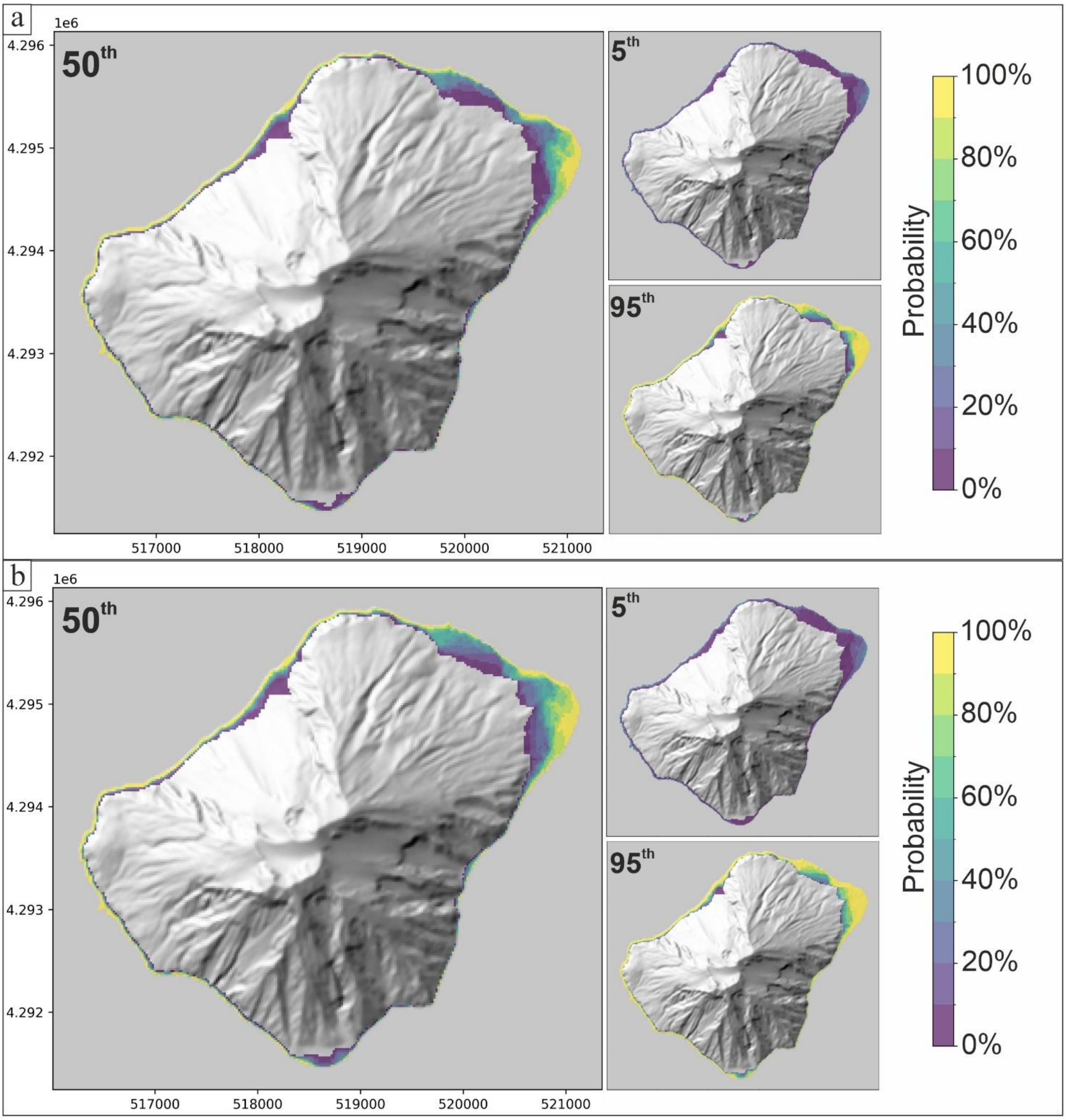

Figure S3. Probabilistic maps for exceeding a water depth of 0.2 m over a 50-year horizon for the Database B. (a) Volume range 1-30 × 10^6 m^3; (b) volume range ≥ 1 × 10^6 m^3.

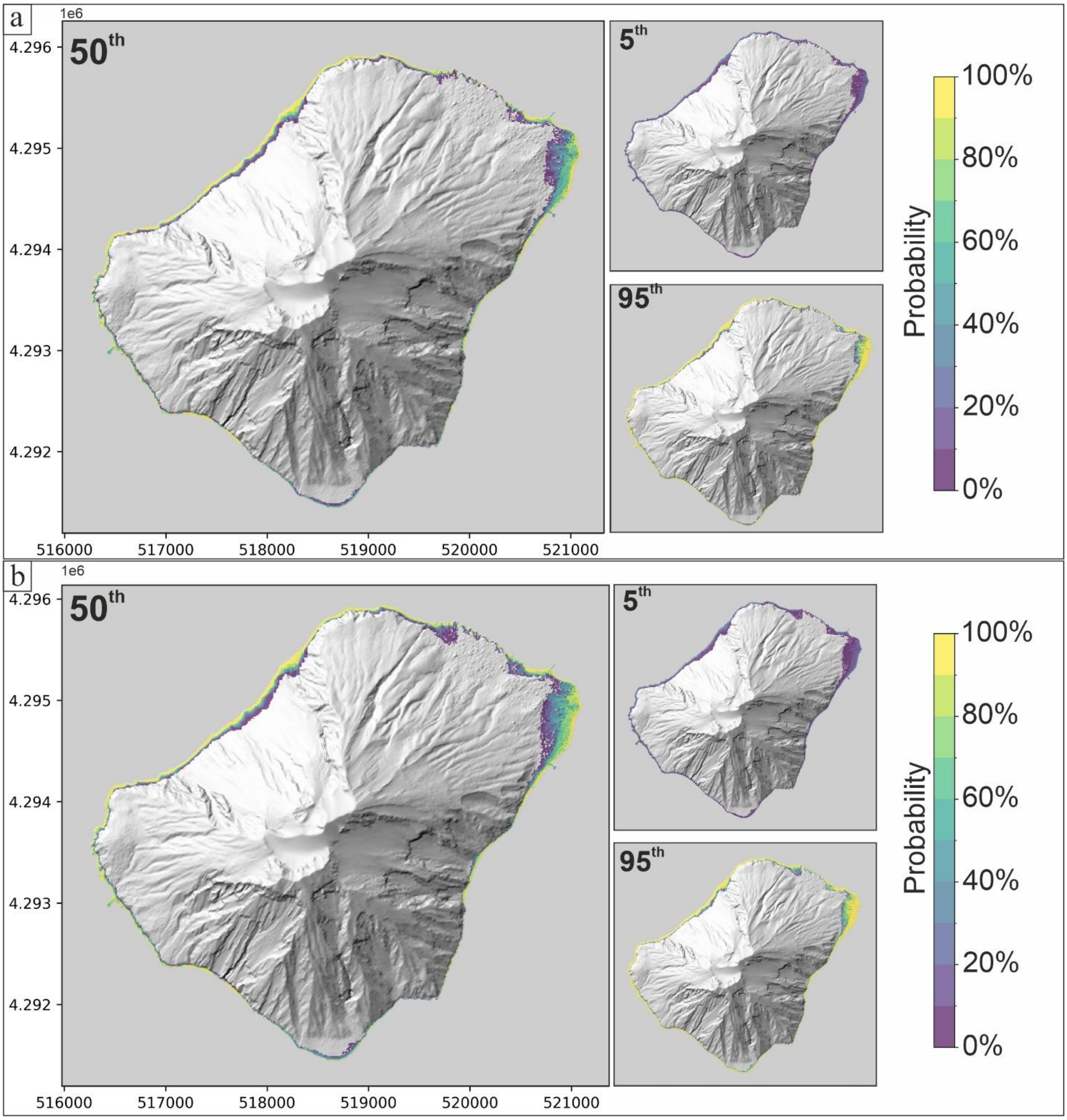

Figure S4. Probabilistic maps for exceeding a water depth of 0.2 m over a 50-year horizon for the Database A. (a) Volume range 1-30 × 10^6 m^3; (b) volume range ≥ 1 × 10^6 m^3.

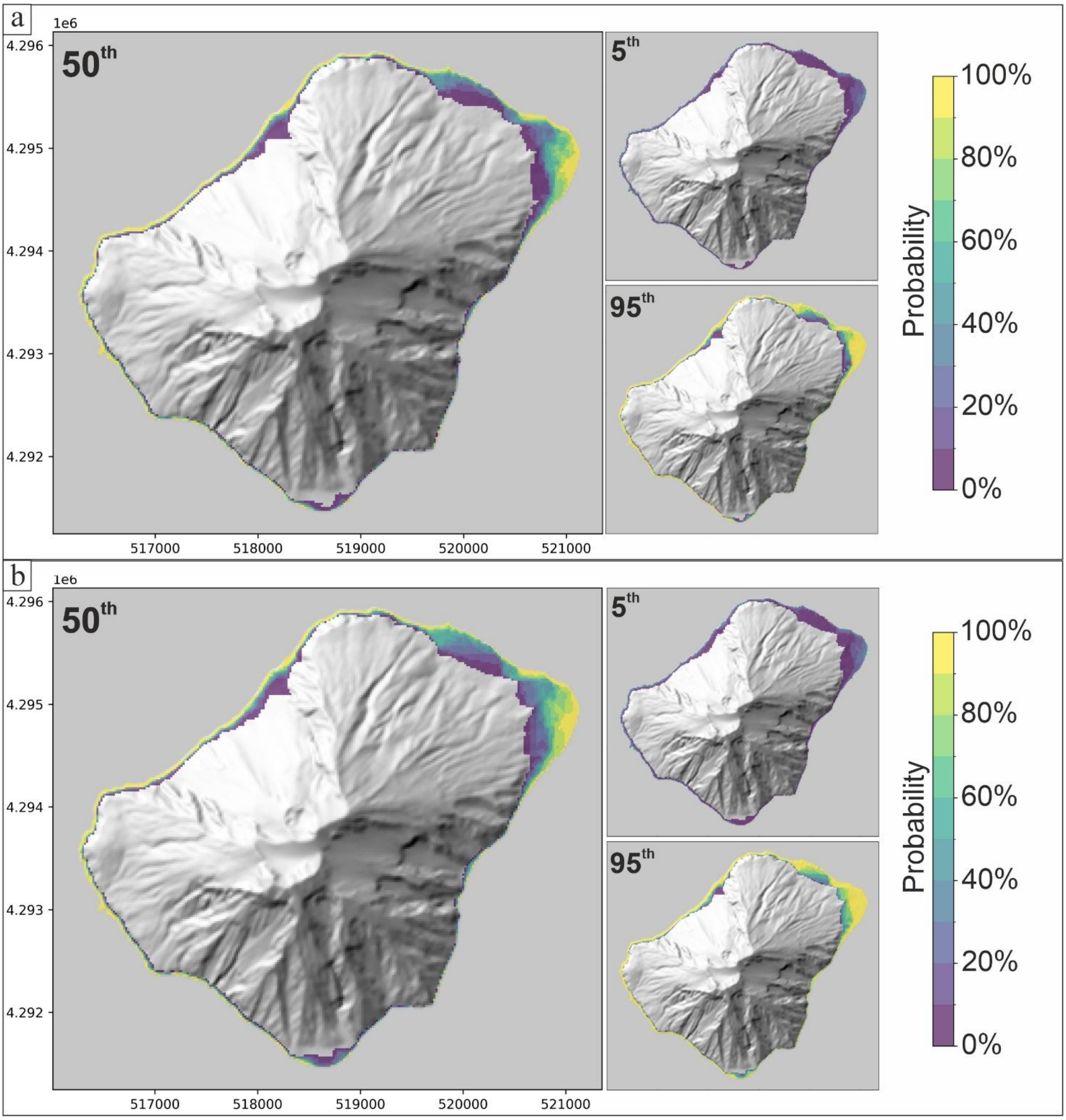

Figure S5. Probabilistic maps for exceeding a water depth of 1 m over a 50-year horizon for the Database B. (a) Volume range 1-30 × 10^6 m^3; (b) volume range ≥ 1 × 10^6 m^3.

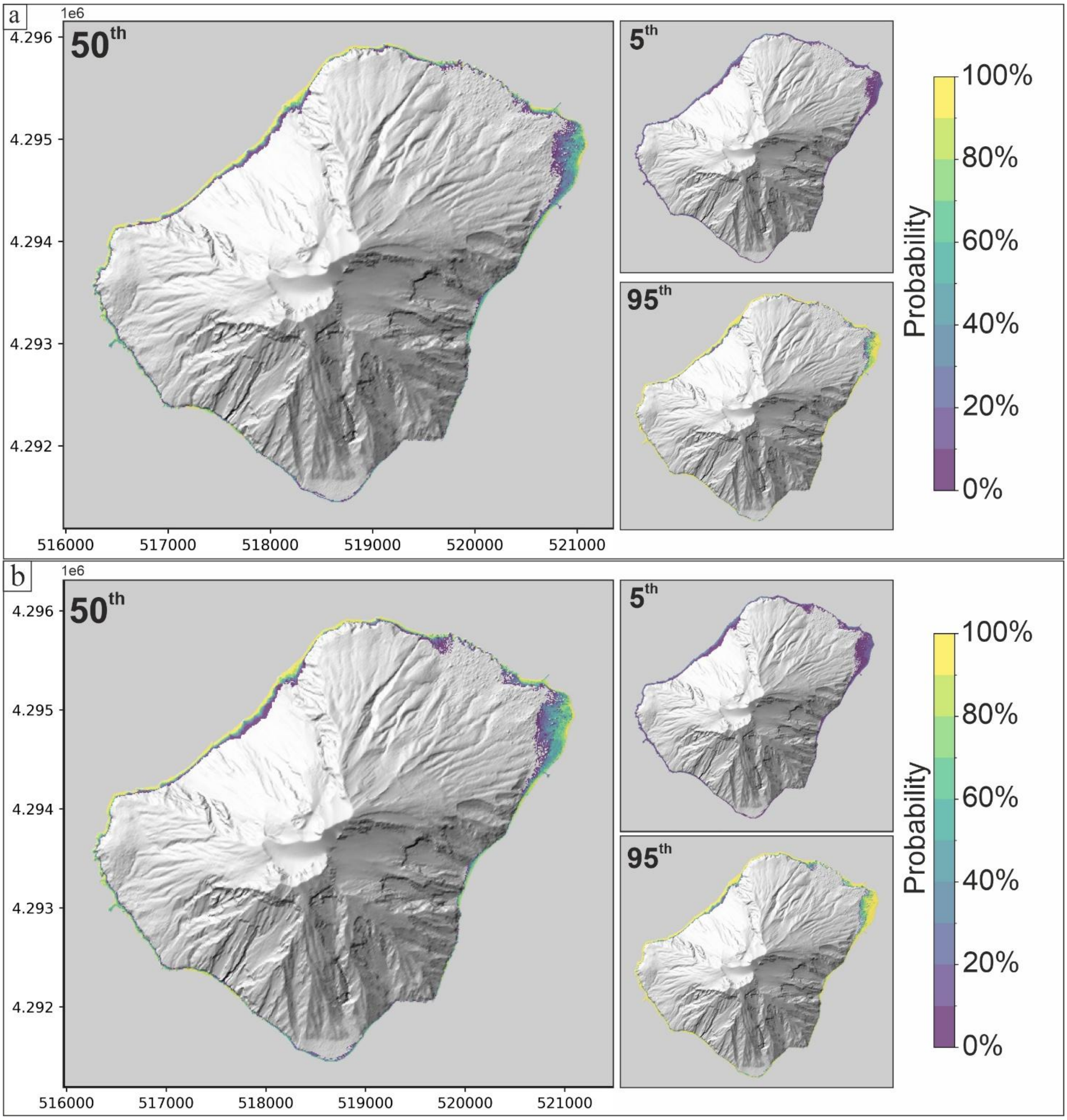

Figure S6. Probabilistic maps for exceeding a water depth of 1 m over a 50-year horizon for the Database A. (a) Volume range 1-30 × 10^6 m^3; (b) volume range ≥ 1 × 10^6 m^3.

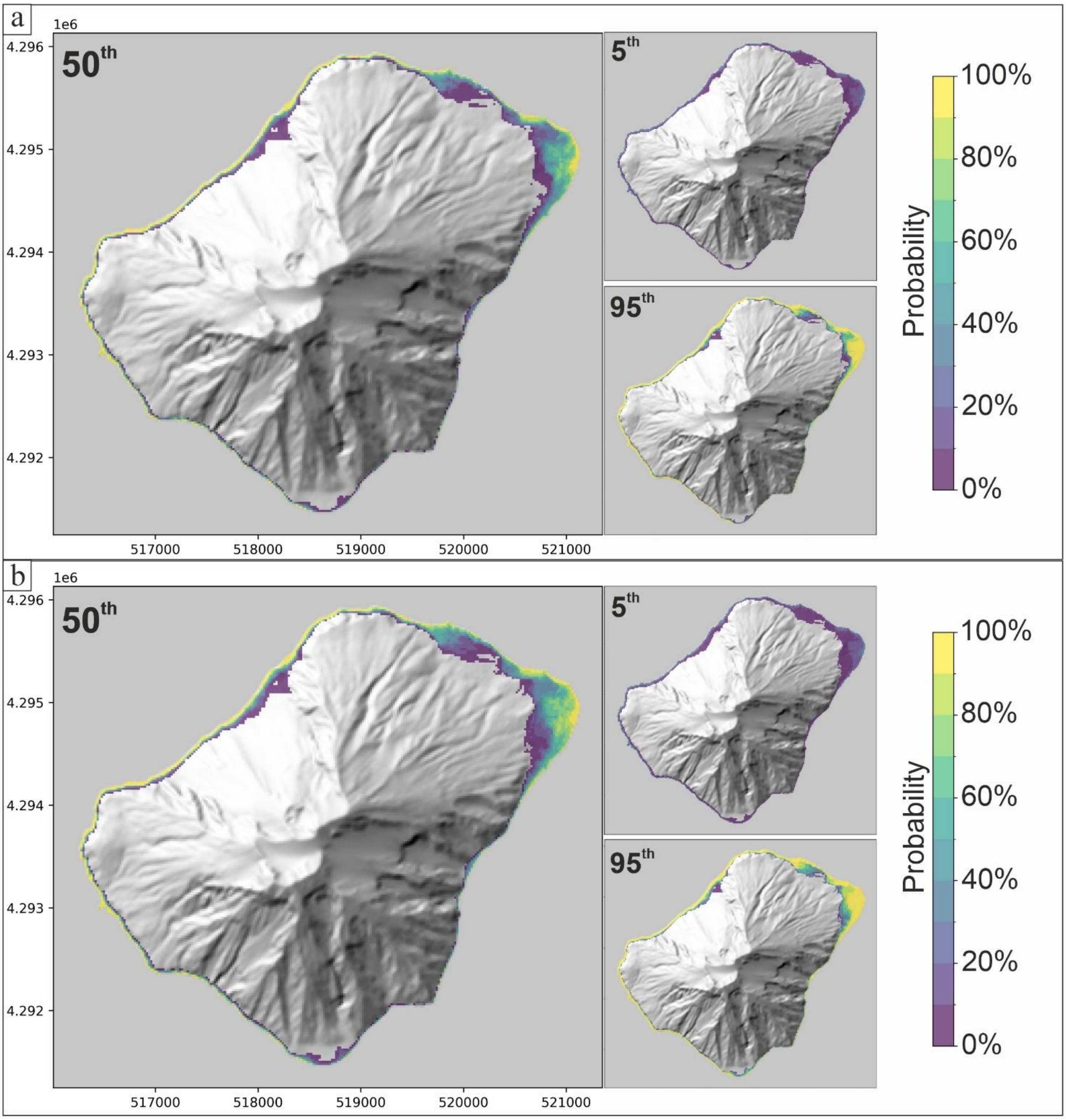

Figure S7. Probabilistic maps showing the inundation water depth corresponding to a 2% exceedance probability over a 50-year horizon for the Database B. (a) Volume range 1-30 × 10^6 m^3; (b) volume range ≥ 1 × 10^6 m^3.

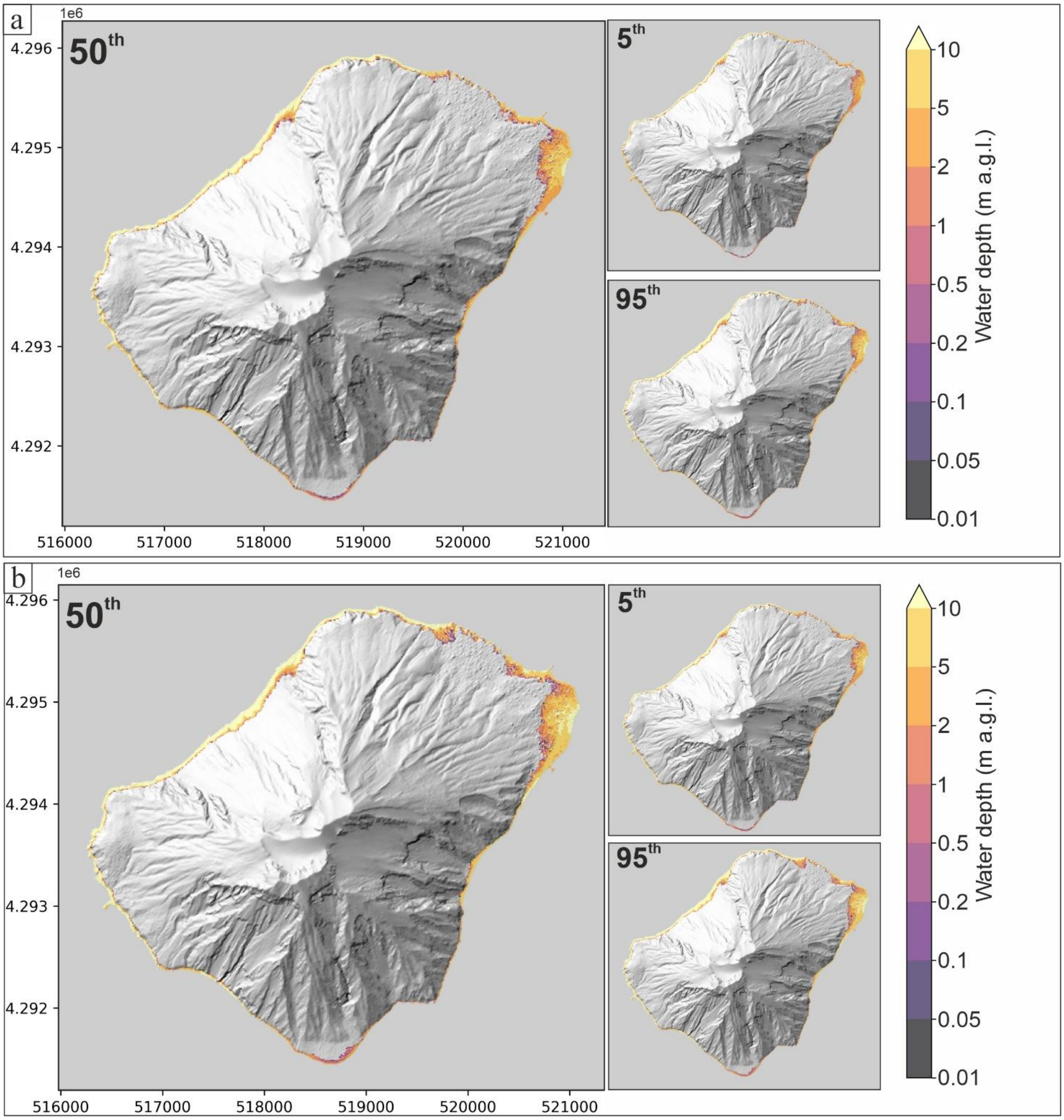

Figure S8. Probabilistic maps showing the inundation water depth corresponding to a 2% exceedance probability over a 50-year horizon for the Database A. (a) Volume range 1-30 × 10^6 m^3; (b) volume range ≥ 1 × 10^6 m^3.

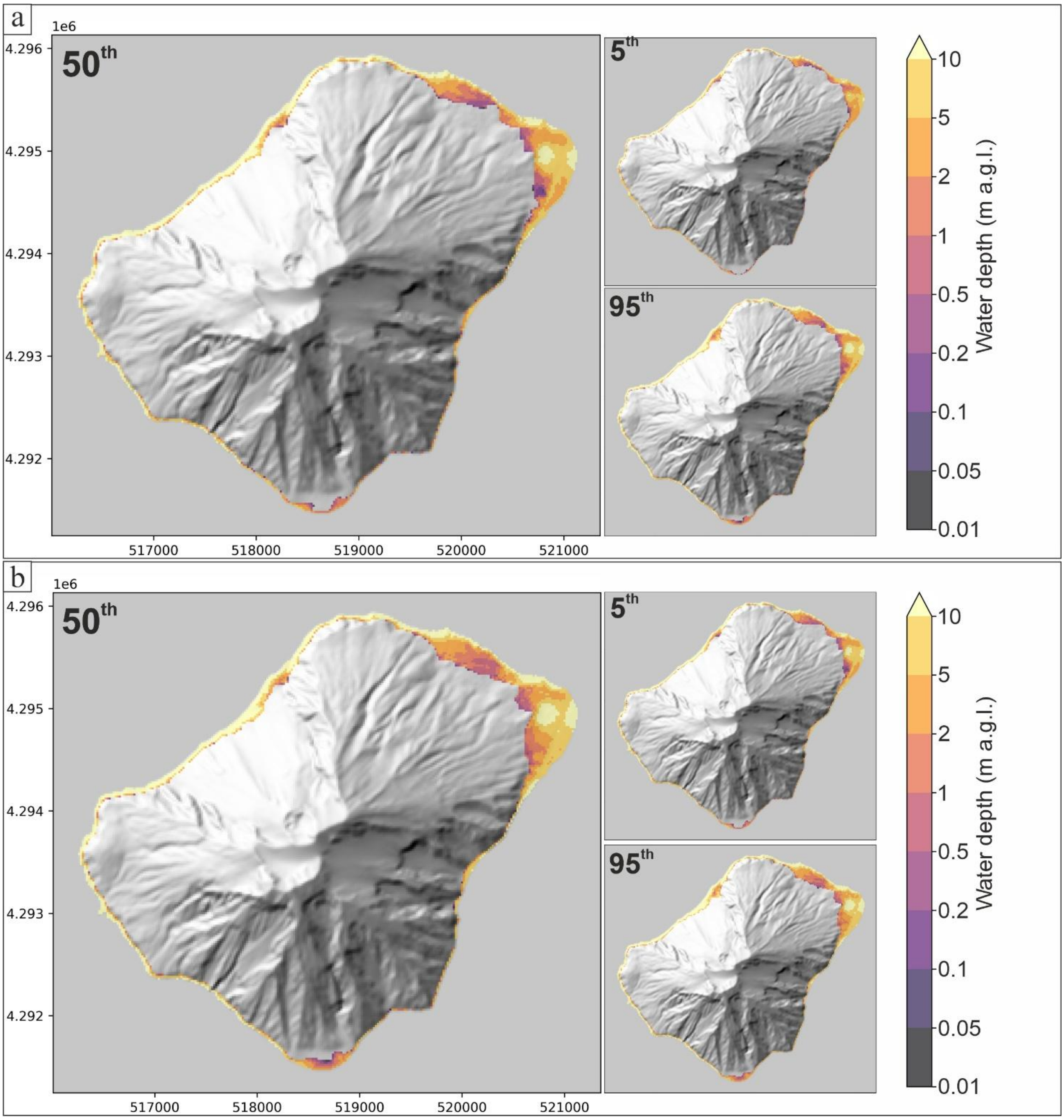

Figure S9. Probabilistic hazard curves for the 6 sites of Fig. 1 (main manuscript) for Database B, volumes 1-30 × 10^6 m^3. Each panel shows the 50-year exceedance probability as a function of water depth for the 5th, 50th, and 95th percentiles of the hazard distribution. Vertical grey dashed lines correspond to the water depth thresholds used for map production (0.1, 0.2, 0.5 and 1 m).

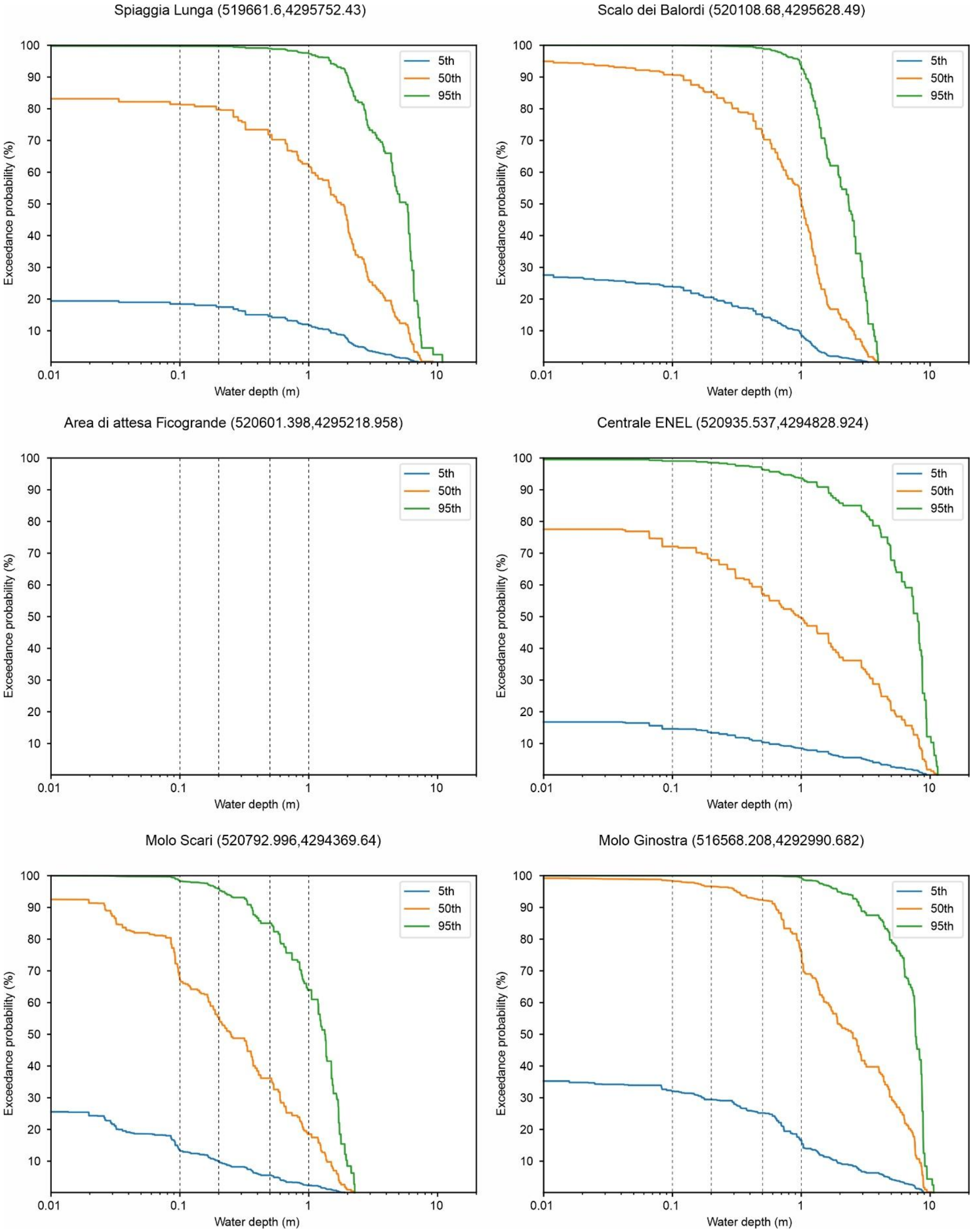

Figure S10. Hazard curves for the 6 sites of Fig. 1 (main manuscript) for Database B, volumes $\geq 1 \times 10^6$ m^3. Each panel shows the 50-year exceedance probability as a function of water depth for the 5^{th}, 50^{th}, and 95^{th} percentiles of the hazard distribution. Vertical grey dashed lines correspond to the water depth thresholds used for map production (0.1, 0.2, 0.5 and 1 m).

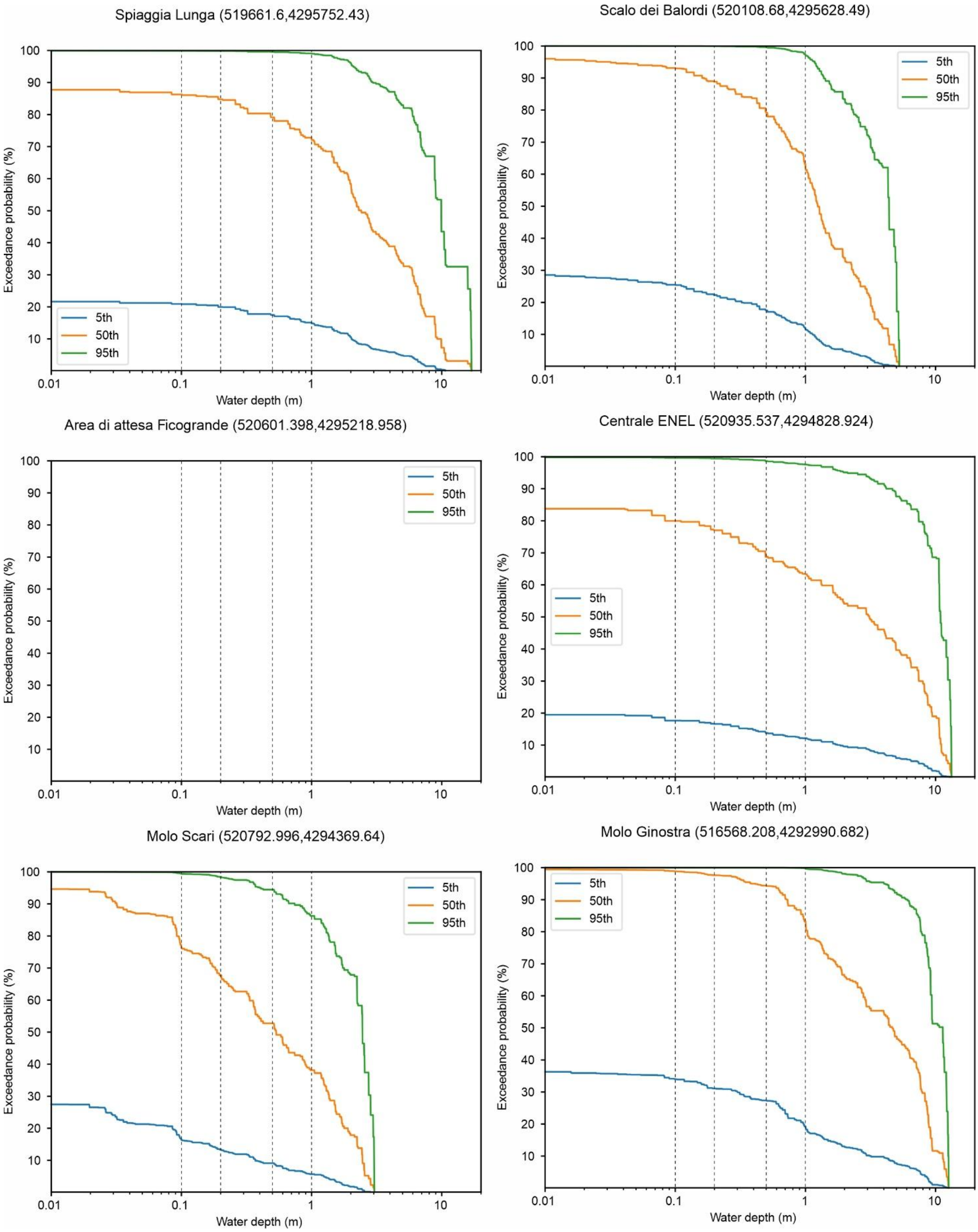

Figure S11. Hazard curves for the 6 sites of Fig. 1 (main manuscript) for Database A, volumes 1-30 × 10^6 m^3. Each panel shows the 50-year exceedance probability as a function of water depth for the 5^{th}, 50^{th}, and 95^{th} percentiles of the hazard distribution. Vertical grey dashed lines correspond to the water depth thresholds used for map production (0.1, 0.2, 0.5 and 1 m).

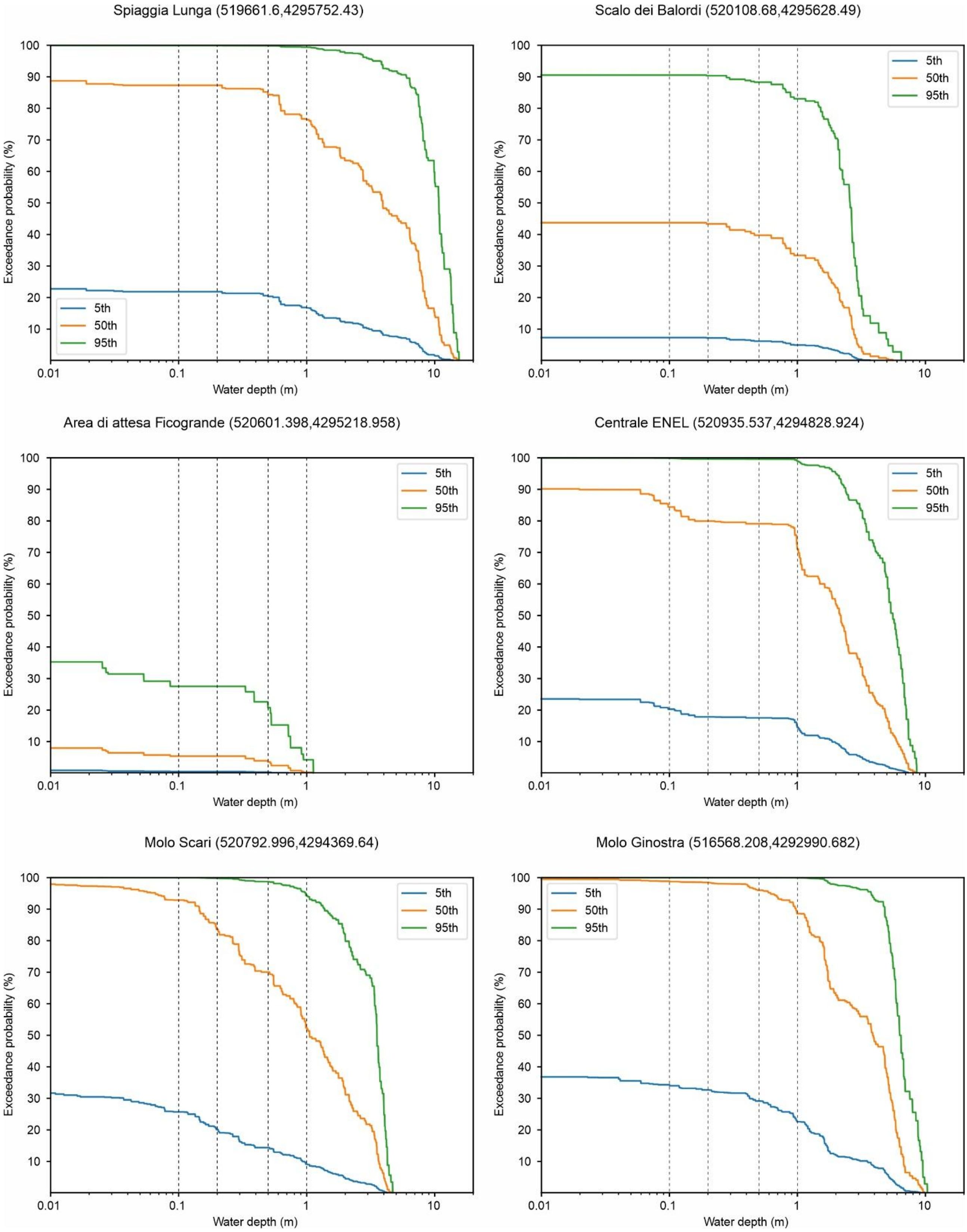

Figure S12. Hazard curves for the 6 sites of Fig. 1 (main manuscript) for Database A, volumes ≥ 1×10^6 m^3. Each panel shows the 50-year exceedance probability as a function of water depth for the 5^{th}, 50^{th}, and 95^{th} percentiles of the hazard distribution. Vertical grey dashed lines correspond to the water depth thresholds used for map production (0.1, 0.2, 0.5 and 1 m).

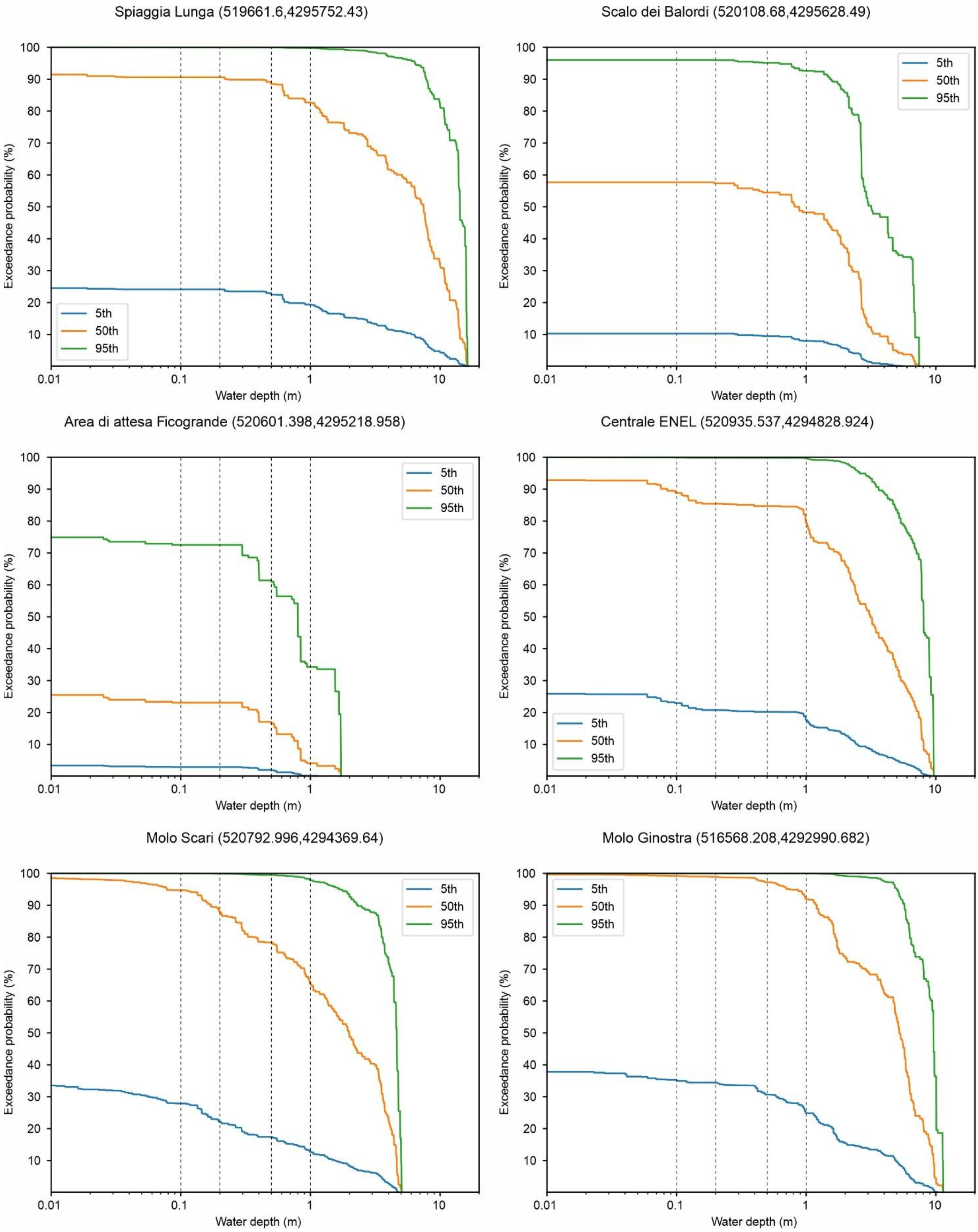

References

de' Michieli Vitturi, M., Bevilacqua, A., Tadini, A., Neri, A.: ELICIPY 1.0: a Python online tool for expert elicitation. SoftwareX, 25, 101641, doi: 10.1016/j.softx.2024.101641, 2024.

de' Michieli Vitturi, M., Bevilacqua, A., Tadini, A., and Neri, A.: Version 2-ELICIPY: A Python online tool for expert elicitation. SoftwareX, 35, 102785, doi: 10.1016/j.softx.2026.102785, 2026.

Grezio, A., Babeyko, A., Baptista, M. A., Behrens, J., Costa, A., Davies, G., Geist, E. L., Glimsdal, S., González, F. I., Griffin, J., Harbitz, C. B., LeVeque, R. J., Lorito, S., Løvholt, F., Omira, R., Mueller, C., Paris, R., Parsons, T., Polet, J., Power, W., Selva, J., Sørensen M. B., Thio, H. K.: Probabilistic tsunami hazard analysis: multiple sources and global applications. Reviews of Geophysics, 55(4), 1158-1198, doi: 10.1002/2017RG000579, 2017.

Selva, J., Lorito, S., Volpe, M., Romano, F., Tonini, R., Perfetti, P., Bernardi, F., Taroni, M., Scala, A., Babeyko, A., Løvholt, F., Gibbons, S. J., Macías, J., Castro, M. J., González-Vida, J. M., Sánchez-Linares, C., Bayraktar, H. B., Basili, R., Maesano, F. E., Tiberti, M. M., Mele, F., Piatanesi, A., Amato, A.: Probabilistic tsunami forecasting for early warning. Nature communications, 12(1), 5677, doi: 10.1038/s41467-021-25815-w, 2021.

Tadini, A., Bevilacqua, A., de' Michieli Vitturi, M., Bonilauri, E., Harris, A., Cerminara, M., Esposti Ongaro, T., Neri, A., Paris, R., Pistolesi, M., Trolese, M., Rodriguez Gàlvez, J. F., Andronico, D., Bertagnini, A., Calvari, S., Casalbore, D., Cassidy, M., Civico, R., Del Bello, E., Di Roberto, A., Fornaciai, A., Grezio, A., Gurioli, L., Harbitz, C. B., Lacanna, G., Løvholt, F., Marani, M., Pompilio, M., Rosi, M., Sandri, L., Urgeles, R., Voloschina, M.: Probabilistic tsunami hazard assessment at Stromboli volcano: 1. Review of historical sources and expert elicitation findings., EGUsphere [preprint], doi: 10.5194/egusphere-2026-1310, 2026Nat. Hazards Earth Syst. Sci., submitted.

Volpe, M., Lorito, S., Selva, J., Tonini, R., Romano, F., Brizuela, B.: From regional to local SPTHA: efficient computation of probabilistic tsunami inundation maps addressing near-field sources. Natural Hazards and Earth System Sciences, 19(3), 455-469, doi: 10.5194/nhess-19-455-2019, 2019.